CCE 2014

Edited by:
Octavian V. Rosca

Computational Civil Engineering

International Symposium

Iasi, Romania - May 24th, 2014

Editura Societatii Academice "Matei-Teiu Botez"

2014

COMPUTATIONAL CIVIL ENGINEERING

2014

Editura Societăţii Academice "MATEI -TEIU BOTEZ"

Proceedings of the 12th International Symposium “Computational Civil Engineering” Iasi, Romania - May 24th, 2014

Scientific publication
ISSN 2285-2735, ISSN-L 2285-2735
Director, Prof. PhD.Eng. Constantin Ionescu
Editor in Chief, Sen.Lect. PhD.Eng. Octavian V. Roşca

CONTENTS

THE 12th INTERNATIONAL SYMPOSIUM "COMPUTATIONAL CIVIL ENGINEERING 2014"

ORGANIZERS

Faculty of Civil Engineering and Installations
Academic Society "Matei - Teiu Botez"
Spanish Association of Seismic Engineering

Co-ordination committee

Prof.PhD.Eng. Mihai Budescu
Prof.Dr.h.c. PhD.Eng. Alex Horia Barbat
Prof.PhD.Eng. Constantin Ionescu

Scientific commission

Prof.PhD.Eng. Doina Ştefan
Prof.PhD.Eng. Elena Axinte
PhD. Eng. Rodian Scînteie
PhD. Eng. Gabriela Covatariu
Sen.Lect.PhD.Eng. Mihai Petru

Organizing commission

Prof.PhD. Eng. Doina Ştefan
Eng. Nicoleta Peşehonov
Sen.Lect.PhD.Eng. Octavian V. Roşca

Some Aspects on Analytical and Numerical Evaluation of Seismic Behaviour on Gravity Retaining Walls

Sergiu Băetu[1], Mihai Vrabie[1]

[1]*Department of Structural Mechanics, "Gheorghe Asachi" Technical University of Iasi, 700050, Romania*

Summary

The retaining walls located in seismic areas are loaded, during earthquakes, by supplementary forces of dynamic nature. In order to evaluate the dynamic active pressure, respectively of the dynamic passive strength, the most frequently is used the pseudo-static method Mononobe-Okabe.

In the present paper are presented some developments, systematisations and specifications to the use of Mohr's theory of limit stress state in order to determine the active and passive earth pressure on gravity retaining walls. It starts from the Rankine hypothesis, according to which the pressures on the surface elements, parallel to the free surface of the soil, have vertical direction. As an effect of the horizontal seismic acceleration, in the soil appear inertial forces which are combining with the vertical pressures, generating in this way normal and shearing stresses on the parallel planes with the soil surface behind the retaining wall. Using the intrinsic curve appropriate to the slip plane and the stresses from this plane, can be obtained the limit Mohr's circles and, than the active and passive pressures generated by the earthquake on the retaining wall. It permits the determination of the slip plane position and also of magnitude for principal normal and shearing stresses in the points of this plane, in which the stress state is limit. All these parameters, determined graphically, are found through finite element method by means of ANSYS software. The soil was modelled with Drucker-Prager model. Also, a comparison between the failure of nature soil slope and a retained backfill with a gravity retaining wall was done.

KEYWORDS: *seismic active pressure, slip plane, limit stress state, Mohr's circle, FEM, Drucker-Prager model.*

Computational Civil Engineering - CCE 2014
International Symposium, Iaşi, Romania, May 24, 2014
ISSN 2285 - 2735, Pages 5 - 18

1. INTRODUCTION

The soil exert pressure or pushing on many engineering structures such as earthworks for communications pathways, waterways regularization, harbour constructions, mining and underground constructions, soil systematisation works on vertically, deep foundations etc. [1], [2], [3], [4].

Retaining structures are used in all cases where an earth mass must be kept in equilibrium. These structures, generic called retaining walls, are generally classified as gravity, semi-gravity, non-gravity cantilevered, non-gravity anchored and soil nail [2], [5]. Among the most widespread and studied types of retaining structures are listed the gravity wall type, which includes rigid gravity, mechanically stabilized earth and prefabricated modular gravity walls. These types of retaining walls derive their capacity to resist lateral loads through the dead weight of the wall [5], [6].

The safety prescriptions require that the retaining wall to resist lateral earth pressures and infiltrated water, to self weight, to the effects of possible overload and, in seismic areas, to the earthquake action. As is known, the lateral pressure of the earth can be classified in three categories, depending on the deformation of the wall: the pressure at-rest, the active pressure and the passive pressure. The magnitude of earth pressure is related to the allowed movement of the retaining structure. Minimum (active) and maximum (passive) earth pressure occur when the retaining structure is allowed to move away from and into the soil, respectively. At-rest pressure falls in between these two extremes and occur when the retaining system is not allowed to move [1], [5]. The value of the active and/or passive pressure can be determined using the Rankine theory, the Coulomb theory, the Log-Spiral-Rankine method, or the Trial Wedge method (depending on the earth retaining system).

For gravity walls, the dynamic earth pressure acting on the wall can be evaluated by using the well-know pseudo-static Mononobe-Okabe (M-O) method. Considering some simple assumptions and using a closed form method, M-O solves the equations of equilibrium and suggests seismic active and passive lateral earth pressure. Thanks to its simplicity, the use of the M-O method to compute seismic active/passive earth pressure is a dominant factor in wall design, both in research literature [1], [2], [4], [5], [9], [10], [12], and in a lot of design prescriptions from many countries [2], [4], [5], [6], [13]. Also, numerical modelling has been applied to verify the practical seismic design methods and the main software used are: ANSYS, ABAQUS, DIANA, PLAXIS [7], [8], [10], [11], [14].

2. ANALYTICAL EVALUATION OF THE SEISMIC EARTH PRESSURE AND SLIP PLANE

The Rankine theory to determine the active/passive pressure of the soil on retaining wall extents in the dynamic case, for both cohesive and cohesionless soil, highlighting the Mohr's circle properties, considered in the limit state. The representation of stress limit state from backfill using Mohr's circle determines the position of slip plane, the principal stresses and of the extreme shearing stresses and other useful values.

With the purpose of Rankine theory expansion to the seismic case the retaining wall from Fig. 1a is considered, having the height H and the upstream face inclined to the vertical with the angle ψ. The soil mass from the back of the wall is characterized by the following parameters: γ – the specific weight; φ – the internal friction angle; c – cohesion; β – the backfill slope; δ – the friction angle at the wall-backfill interface; q – the vertical overload intensity from the backfill.

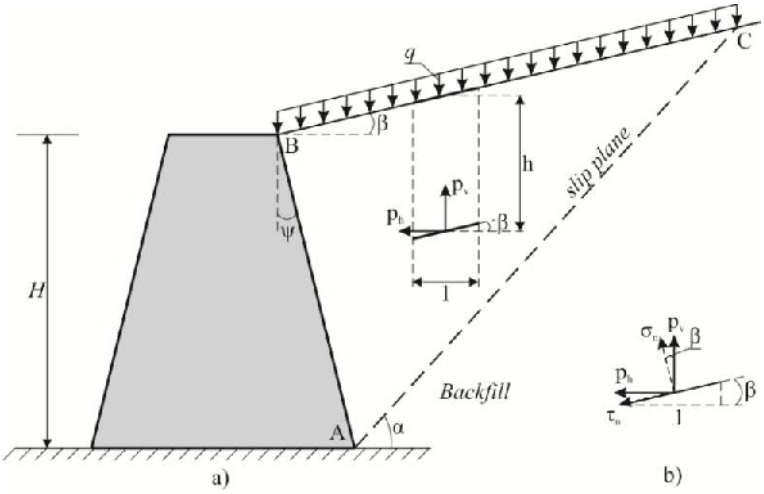

Figure 1. The assemble retaining wall – backfill: a) general characteristics b) pressures on the inclined element – decompositions details

Similar to the static case, is kept the Rankine hypothesis, according to which the pressure from a point located at the height h, on a plane parallel to the backfill surface, is vertical. A column with the height h, with the horizontal section equal to the one, produces on the inclined element a vertical pressure.

During the earthquake action, the horizontal seismic acceleration,

$$a_h = k_h g \tag{1}$$

(where k_h is the seismic horizontal coefficient and g is gravitational acceleration), on the considered prism of soil generates inertial forces.

The horizontal seismic pressure, p_h, is obtained amplifying the vertical force with the horizontal seismic coefficient k_h:

$$p_h = k_h p_v = k_h(\gamma h + q)\cos\beta \tag{2}$$

The pressures p_v and p_h decompose in normal respectively tangent directions, to the inclined surface element (Fig. 1b), and the following stresses are obtained:

$$\sigma_n = p_v \cos\beta + p_h \sin\beta = (\gamma h + q)\cos^2\beta + k_h(\gamma h + q)\cos\beta\sin\beta \tag{3}$$

$$\tau_n = -p_v \sin\beta + p_h \cos\beta = -(\gamma h + q)\cos\beta\sin\beta + k_h(\gamma h + q)\cos^2\beta$$

The equations (3), can be written, more compact, in the form:

where were inserted the notations [15]:

$$\bar{\sigma}_n = \cos^2\beta + k_h \cos\beta\sin\beta; \quad \bar{\tau}_n = -\cos\beta\sin\beta + k_h\cos^2\beta \tag{5}$$

The values $\bar{\sigma}_n$ and $\bar{\tau}_n$ are dimensionless and depend on the backfill slope (through β angle) and on the wall location (through the k_h coefficient).

The physical interpretation of those two values can be done considering in equation (4):

$$\gamma\bar{h} + q = 1 \quad \Rightarrow \quad \bar{h} = \frac{1-q}{\gamma} \tag{6}$$

meaning that $\bar{\sigma}_n$ and $\bar{\tau}_n$ are normal and respectively shearing stress on the surface element parallel to the backfill surface, located at the $\bar{h}$ depth relative to this. All the precedent equations can be particularized easily for the cases where the backfill surface is horizontal ($\beta = 0$) and/or when the overload is missing ($q = 0$).

When in soil was reached to the limit state, meaning that a slip plane was formed, in a point from this plane (for example, the point A from the base of the wall – Fig. 1a), the stresses σ_n and τ_n represents a limit state; the point M(σ_n, τ_n) will be find on the limit Mohr's circle. The envelope of the limit circles, which delimits in the plane $\sigma O\tau$ the admissible stress state domain, is called intrinsic curve or failure envelope (Fig. 2). In the case of cohesive soils, having the internal friction angle φ and the cohesion c, the equation of the lines which forms the failure envelope is:

$$\tau = c + \sigma\tan\varphi \tag{7}$$

The two lines are concurrent in the point O', located at the distance *s* from O:

$$s = \frac{c}{\tan\varphi} \tag{8}$$

Supposing that the soil is cohesive and knowing the internal friction angle, φ, and the cohesion, *c*, of the soil (from experimental tests), the intrinsic curve can be plotted. Any circle tangent to the intrinsic curve represents a limit stress state. It is assumed, also, that in the backfill a limit stress state was reached, and therefore the slip plane has formed. In a point located on this plane (that can be even the point A from the base of the wall), on a parallel section with the surface of soil, the stresses σ_n and τ_n represent a limit stress state. In the plane σOτ, the point M, of coordinates (σ_n, τ_n), will be find on Mohr's circle corresponding to yielding. From the geometric point of view, the demand is to draw a circle that passes through M and is tangent at the two lines which represents the failure envelope. Through the point M will pass two circles, which fulfil the mentioned demand: the small circle corresponds to active pressures and it is represented in Fig. 2 and the large circle (unrepresented in Fig. 2) corresponds to passive pressures.

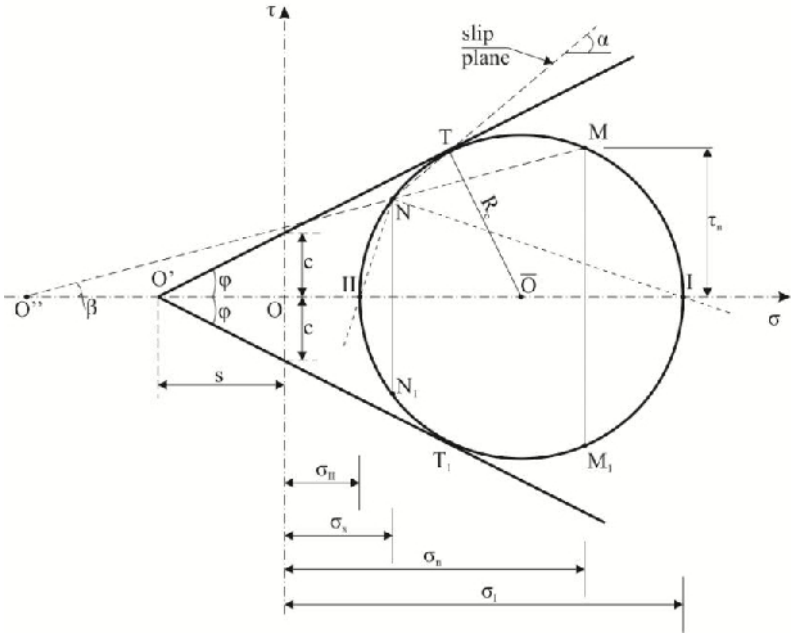

Figure 2. The graphical representation of limit stress state of active pressures (limit Mohr's circle)

The line which passes through the point M and is inclined with the angle β from horizontal (is parallel to the surface of the soil) intersect the circle in the point N, which is the pole of the circle. The pole has the property that the line which unifies it with a point from the circle is parallel with the section on which acts the stresses which represents the coordinates of that point. Therefore, the line NM is parallel to the plane on which acts the stresses (σ_n, τ_n), and is inclined with the angle β from direction Oσ.

For a retaining wall with vertical upstream face AB ($\psi = 0$), at a linear distribution of the pressures, knowing $\sigma_{xA} = p_A$ and $\sigma_{xB} = p_B$ the resultant of seismic active pressure can be computed (on a length equal to 1):

$$P_{as} = \frac{p_A + p_B}{2} H \tag{9}$$

Regarding the pressures p_A, p_B, should be considered the particular cases of cohesive and cohesionless soils, the overloads existence or absence etc. Particularly, on the upstream face of the wall with height H, the backfill having the slope β and in absence of the overload (Fig. 3), it can be written the pressure at the base of the wall using (4):

$$p_A = \sigma_{xA} = \gamma H \bar{\sigma}_{xA} \tag{10}$$

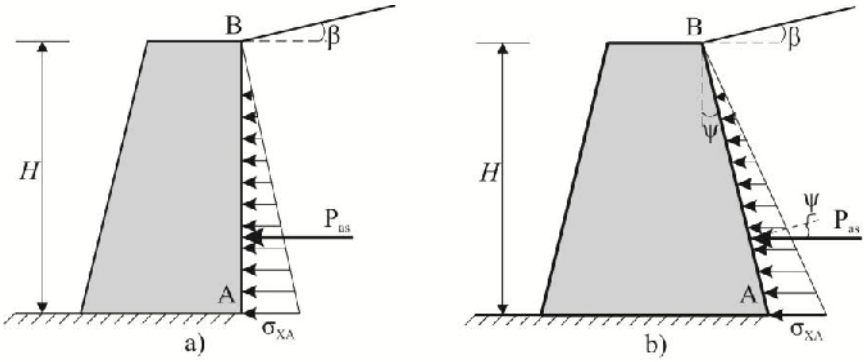

Figure 3. The triangular diagram of the seismic active pressure: a) on the vertical upstream face; b) on the inclined upstream face

The resultant of the seismic active pressure will be equal with the surface of diagram

$$P_{as} = \frac{1}{2}\sigma_{xA} H = \frac{\gamma H^2}{2}\bar{\sigma}_{xA} = \frac{\gamma H^2}{2} K_{as} \tag{11}$$

where $K_{as} = \bar{\sigma}_{xA}$ is the seismic coefficient of the active pressure.

The effect of the overload, of constant intensity q, leads to uniform pressures on height with the resultant qK_{as}; this resultant is added to (11) and the total resultant will be

$$P_{as} = \frac{\gamma H^2}{2} K_{as} + qK_{as} = \frac{K_{as} H}{2}(\gamma H + 2q) \tag{12}$$

On Mohr's circle from Fig. 3, the pressure σ_{xA} corresponds to the point N_1, therefore

$$\sigma_{xA} = \sigma_x^{N_1} = \sigma_x^N = (\gamma H + q)\bar{\sigma}_x^N \tag{13}$$

and $\bar{\sigma}_x^N = K_{as}$ with which can be found the active pressures resultant P_{as}.

The slip plane direction can be obtained connecting the pole N with the tangent point, T, of the circle with the failure envelope. The parallel at NT, through the point A from the base of the wall and which is inclined with the angle α with the horizontal, represents the direction of slip plane (AC in Fig. 1a).

The points I and II determines the values of the principal stresses: σ_I is the maximum stress, and σ_{II} is the minimum one. The principal stress directions, normal to the principal planes on which the tangential stresses are null, are found by connecting the pole with the points I and II.

The centre of the circle, $\bar{O}$, has the coordinates $((\sigma_{I+} \sigma_{II})/2;0)$, and the radius is equal to the maximum shearing stress, namely

$$R_c = \tau_{\max} = \frac{\sigma_I - \sigma_{II}}{2} \tag{14}$$

Similar judgments can be expanded also in the case of seismic passive pressure, using properly the Mohr's circle (the large circle that passes through M and is tangent to the intrinsic curve).

3. COMPUTATIONAL EVALUATION OF THE EARTH PRESSURE AND SLIP PLANE – CASE STUDY

3.1. Model description

The case of study considers a gravity retaining wall and the soil that surrounds it (Fig.4). The computational analysis was performed with the ANSYS 12 computer program and the plane strain finite element PLANE83 was used for soil and for retaining wall. Drucker-Prager material model was used for the modelling of the backfill soil non-linear behaviour (Fig.5) [16][17][19][20]. In ANSYS the critical failure surface is found automatically and the progressive failure can be easily monitored. The interaction between soil and the gravity retaining wall was simulated with contact finite element CONTA172/TARGET169 [19][20]. The soil zone behind and under the gravity retaining wall was taken such that the stresses and strains to be negligible in the restrained zones, in this way the stress and strain state is not influenced by the restrains [16].

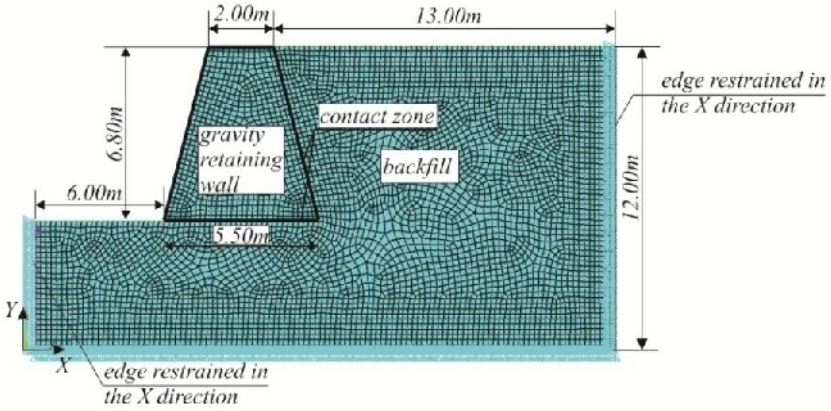

Figure 4**.** The mesh and the dimensions of the studied gravity retaining wall

Table 1. Geotechnical parameters used in the FEM model for foundation soil and backfill

Parameters	Value
Density	1800 kg/m^3
Poisson's ration	0.32
Young's modulus	10 MPa
Cohesion	0.03 MPa
Friction Angle	30°
Flow Angle	10°

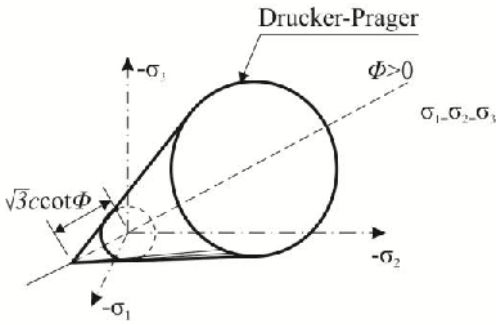

Figure 5. Drucker-Prager model used for soils

Table 2. Gravity retaining wall parameters used in the FEM

Parameters	Value
Density	2500 kg/m^3
Poisson's ration	0.2
Young's modulus	30000 MPa

3.2. FEM Analysis

Firstly, an analysis of a nature soil slope is done, in order to show the failure surface. The loads considered in this analysis were the self weight of the soil and retaining wall and a surcharge on the top of the soil. The surcharge was increased incrementally until the soil fails. Also, in order to simulate the seismic action, an acceleration was introduced in the direction of the gravity retaining wall. The design value for the seismic force, used in pseudo-static analyses, on a nature soil slope is [13]:

$$F_H = 0.5\alpha SW$$

Where: S – is the characteristic parameter of the soil type (according to SR EN 1998-1-2004 for soil from class A, S = 1);

W – is the weight of the soil analyzed;

$$\alpha = \frac{a_g}{g};$$

g – is the gravitational acceleration;

a_g – is the seismic soil acceleration (according to P100-2013 the value for a_g = 0.25g for IASI zone).

The design value for the horizontal seismic force, used in pseudo-static analyses, for the backfill and the retaining structure is [13]:

$$F_H = k_h W$$

$$k_h = \frac{\alpha S}{r} = \frac{0.25 \cdot 1}{2} = 0.125$$

For a free gravity retaining wall which can accept a displacement till dr=300αS (mm), r=2.

The horizontal seismic acceleration inputted in ANSYS software is: $a_h = k_h g = 0.125 * g$ (where k_h is the seismic horizontal coefficient and g is gravitational acceleration).

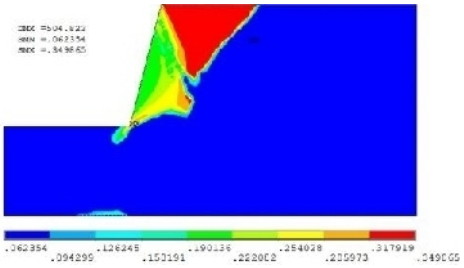

Figure 6. Plastic equivalent stress

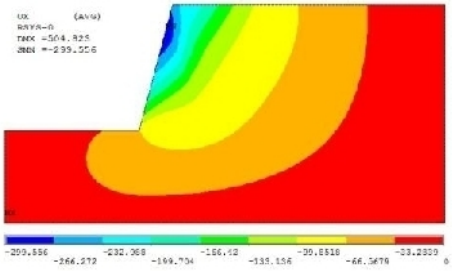

Figure 7. X-Component of displacement

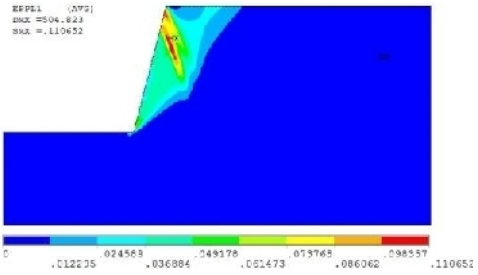

Figure 8. 1st principal plastic strain

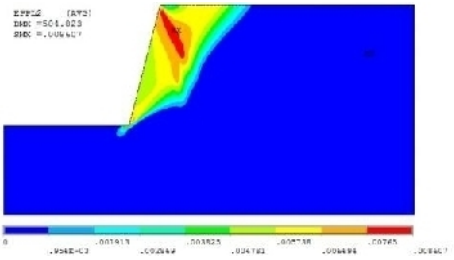

Figure 9. 2nd principal plastic strain

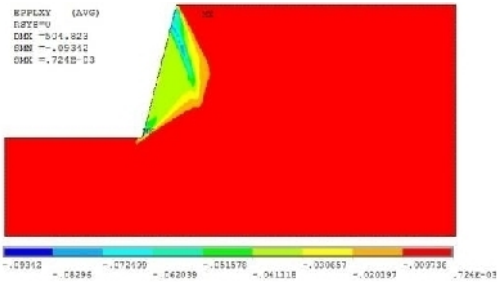

Figure 10. XY-Shear plastic strain

From the numerical analysis on the nature soil slope, it can be seen very clear in Fig. 6 that plastic equivalent stresses were developed in the zone where the slope is high, resulting the soil failure. The maximum plastic equivalent stress is 0.35 MPa at the base of the slope. Also, the X displacements are maxim near the steep, namely 300 mm, and decrease radial (Fig. 7). Fig. 8 and 9 depict the principal plastic strain developed in the soil, and in Fig. 10 can be seen the XY shear plastic strain.

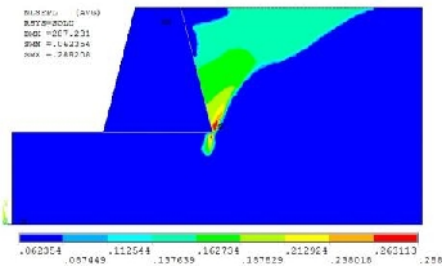

Figure 11. Plastic equivalent stress

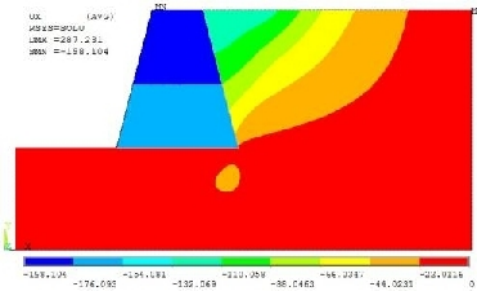

Figure 12. X-Component of displacement

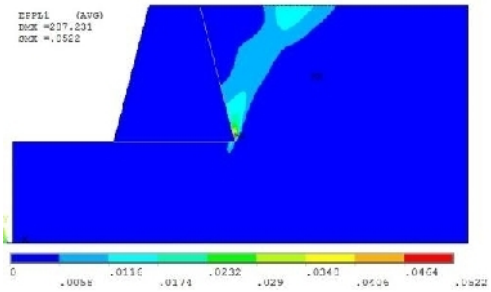

Figure 13. 1st principal plastic strain

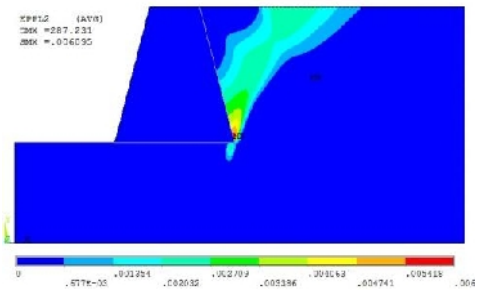

Figure 14. 2nd principal plastic strain

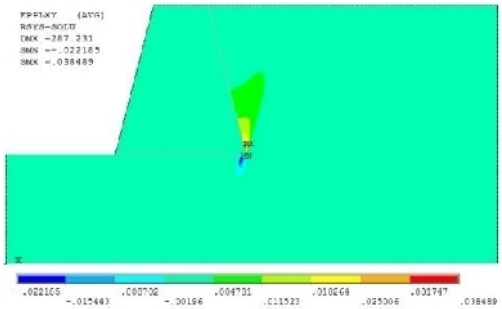

Figure 15. XY-Shear plastic strain

From the numerical analysis on the soil slope retained by a gravity retaining wall, it can be seen very clear on the plastic equivalent stress map, from Fig. 11, the failure plane development in the backfill. The maximum plastic equivalent stress is 0.28 MPa at the base of the slope. Also, the X displacements are maxim at the top of the gravity retaining wall, namely 198.1 mm (Fig. 7); this is due to the tilting effect.

Fig. 8 and 9 depict the principal plastic strain developed in soil, and in Fig. 10 can be seen the XY shear plastic strain which are smaller that the plastic strains from the nature soil slope.

4. CONCLUSIONS

The oldest and the most widely used method for the evaluation of dynamic pressure of soil on the gravity retaining walls is the pseudo-static Mononobe-Okabe method. The results obtained are valid only in the adopted hypotheses field, but there are many practical cases in which the M-O theory cannot be applied.

Many researchers have developed a variety of analytical, numerical and experimental methods in order to describe accurately the dynamic behaviour of retaining walls, methods which tried to exceed the limits of the M-O theory.

The analytical method described in this paper, starts from Rankine hypothesis, according to which, the pressure from a point located on a section parallel to the surface of the backfill is vertical (similar to the static case). If the mentioned point is on the slip plane (for instance, the point A from the wall base), then the stress state from the point is a limit state. This stress state it is represented graphically with Mohr's circle, which must be tangent to the intrinsic curve and must pass through the point M(σ_n , τ_n).

Having as input data characteristics on the backfill and the retaining wall (φ, c, β, γ, q, δ, H, k_h) and manipulating the limit Mohr's circle, can be determined:

- the resultant of active/passive seismic pressure that acts on the wall;
- the direction of slip plane (the α angle with the horizontal);
- the principal stresses and their directions;
- the extreme shear stresses in the slip plane points;
- the volume of the failure prism ABC (knowing the angle α).

The seismic pressure coefficient of the soil can be determined for cohesionless and cohesive soils, both in the case of active pressure and also in the case of passive one.

Also, a numerical evaluation of slip plane was done with finite element software, ANSYS. Firstly, plastic equivalent stresses were computed for the nature soil slope, in order to show the soil failure without retaining structures. Other parameters such as the X displacements the principal plastic strains and the XY shear plastic strain were plotted. In the end, the same parameters were plotted for the retaining wall and backfill. It can be clear seen that the failure mechanism is

very different for these two solutions with and without gravity retaining wall. The plastic strains in the backfill behind the retaining wall are smaller that the plastic strains from the nature soil slope.

References

1. Al Atik L. & Sitar N. *Experimental and Analytical Study of the Seismic Performance of Retaining Structures*, Pacific Earthquake Engineering Research Center (PEER), University of California, Berkley, 295 pp., 2008;
2. Anderson G.D., Martin R.G., Lam (Po) I., Wang J.N., *Seismic Analysis and Design of Retaining Walls, Buried Structures, Slopes and Embankments*, NCHRP Report 611, Washington D.C., 148 pp., 2008.
3. Moga A.S. About compliance and calculation of planar and spatial elements used in the retaining constructions, *Ph.D. Thesis*, "Gheorghe Asachi" Technical University of Iasi, pp. 65-144, 2005 (in Romanian).
4. Visone C. & Santucci de Magistris F. A review of design method for retaining structures under seismic loadings, Structural and Geotechnical Dynamic Lab StreGa, University of Molise, Termoli (CB), Italy (www.reluis.it/doc.pdf/Publicazioni/Visone-Santucci.pdf), pp. 1-14.
5. Samsabadi A., Xu S-Y, Taciroglu E. Development of Improved Guidelines for Analysis and Design of Earth Retaining Structures, University of California, Los Angeles (UCLA), Structural and Geotechnical Engineering Laboratory, UCLA-SGEL Report 2013/2, pp. 243, 2013.
6. Au-Yeung Y.S. & Ho K.K.S., Gravity Retaining Walls Subject to Seismic Loading, *Geo Report No. 45*, Hong Kong Government, pp. 7-13, 1995.
7. Al Atik L. & Sitar N. Seismic Earth Pressure on Cantilever Retaining Structures, *J. Geotech. Geoenviron. Eng., 136 (10)*, pp. 1324-1333, 2010.
8. Rajeev P. Numerical modeling seismic response of cantilever earth retaining structures, *SAITM Research Symposium on Engineering Advancements* (SAITM-RSEA), pp. 7-10, 2012.
9. Hazarika H. Prediction of Seismic Active Earth Pressure Using Curved Failure Surface with Localized Strain, *American J. of Engineering and Applied Sciences 2(3)*, Science Publications, pp. 544-558, 2009.
10. Kalasin T. & Wood Muir D. Seismic Analysis of Retaining Walls within Plasticity Framework, *The 14th WCEE*, Beijing, China, 11 pp., October 12-17, 2008.
11. Yang S., Chegnizadeh A., Nikraz A. Review of Studies on Retaining Wall's Behavior on Dynamic/Seismic Condition, *Int. J. of Engineering Research and Applications*, vol.3, Issue 6, pp. 1012-1021, 2013.
12. Yazdani M., Azad A., Farshi A.H., Talatahari S. Extended "Mononobe-Okabe" Method for Seismic Design of Retaining Walls, Hindawi Publishing Corporation, *Journal of Applied Mathematics, Volume 2013*, Article ID 136132, 10 pp., 2013.
13. SR EN 1998-5 Eurocode 8: *Design of structures for earthquake resistance*, Part 5: Foundations, retaining structures and geotechnical aspects, pp. 27-30, 36-39, 2006.
14. Song F. & Zhang J-M Evaluation of Seismic Earth Pressure at the Passive Side, *The 14th WCEE*, Beijing, China, 11 pp., 8 pp., October 12-17, 2008.

15. Ungureanu N., Moga A., Vrabie M. Extending Mohr's Theory of Limit States in Determining Soil Seismic Loads on Retaining Walls, *Bull. of the Polytechnic Institute of Jassy, Construction. Architecture Section*, Tomme LI (LV), Fasc. 1-2, pp. 7-13, 2005.

16. Cakir T., Livaoglu R., Dogangun A., Effects of different backfill soil types on dynamic behaviour of rectangular tank wall considering backfill-wall-fluid interaction, *The 14th World Conference on Earthquake Engineering*, Beijing, China, 2008.

17. Lund G., Dawson B., Foster M., Hume dam – seismic analysis of soil/structure interaction, *Innovative Dam and Levee Design and Construction*, pp. 1531-1547, 2012.

18. Jalali M., Golmaei H., Jalali R., Borthwich A., Ahmadi Z., Moradi R., Using Finite Element method for Pile-Soil Interface, *Journal of Civil Engineering and Construction Technology, Vol. 3(10)*, pp. 256-272, 2012.

19. Barrett P.R., *CivilFEM Geotechnical Webseminar*, 2009.

20. ANSYS 12 Structural Analysis Guide, 2009.

Factors of Influence for the Wind Flow Over Flat Roofs Equipped with Solar Panels Studied on Physical Models

Georgeta Băetu[1], Elena Axinte[1], Carmen Elena Teleman[1], Victoria Elena Roșca[1], Silviu Cristian Melenciuc[1]

[1]*Department of Civil and Industrial Engineering, "Gheorghe Asachi" Technical University, Iaşi, 700050, Romania*

Summary

The solar panels placed on the roof surface stand for a frequent solution of obtaining „green energy" by optimizing the built environment. In the evaluation of the wind loading on the solar panels an important role is played by the combination between the wind and building interference, the direction of the wind action and the particular features of the solar panels field (that may be isolated or grouped in consecutive rows). These particular features of the interaction between the in wind flow and the complex field of obstacles become ultimate factors that act together in the process of modelling the local and general distribution of the wind speed and pressure.

KEYWORDS: wind action, wind tunnel, numerical simulation, solar panels, flat roofs.

1. INTRODUCTION

Placing solar panels on the building roofs is a handy solution from the point of view of the built environment, the lowest consumption of materials, manoeuvre and even energy losses due to the proximity to the consumer. The structural systems used for supporting the solar panels should be designed as to be prevented from malfunctions due to occasional wind strong and turbulent manifestations. The major problem in their design is a realistic evaluation of the lifting forces as a result of the loads transferred by the wind pressure action followed by the search of suitable solutions to reduce them. In the analysis of wind loads on the solar panels, the parameters that influence the air flow depend on the built environment, the panels array together with the wind profile itself [1, 2]. Thus, in assessing wind loads on solar panels placed on roofs, the following characteristics occur:

- wind velocity and direction,
- height of the building and the presence or the lack of the parapet
- position of the building in built environment,
- arrangement of panels - parallel to the sides of the building or skew,
- inclination angle of panels (tilt),
- position of the panels with respect to the roof edges,
- individual position of the current panel in the entire group.

Generally, the solar panels located on the roofs of the buildings change the distribution of velocity and pressure fields, respectively. Pressure coefficients showed off in wind design codes for flat roofs are useless for the determination of particular values of wind pressure on the solar panels because they usually present standard simplified regular situations of wind local pressure coefficients on the surface of the buildings. It becomes then necessary to model the interaction between the incoming air flow and the obstacles that represent the built environment in the wind tunnel. According to SR EN 1991-1-4 [9], loads generated by wind are calculated as the product of the reference wind pressure, the aerodynamic coefficient and the exposure factor, the last depending on the roughness of the terrain. As the aim of this particular study was to determine the design resultant forces transferred to the sustaining structure of the solar panels from the subsequent surfaces exposed to wind action, the assessed wind loading on the panel's supports is based on the averaged pressure coefficients; these coefficients are obtained as the algebraic sum of all the pressure coefficients (fig. 1) gathered from the two exposed surfaces of the panel:

$$c_{p,net} = c_{p,us} - c_{p,ls} \tag{1}$$

where $c_{p,us}$ is the pressure coefficient from the upper surface and $c_{p,ls}$ is the pressure coefficient from the lower surface. Negative values of this coefficient represent the areas with negative pressure.

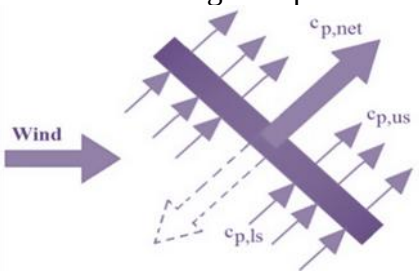

Figure 1. Calculation of the $c_{p,net}$ coefficient

2. INFLUENCE OF FACTORS FROM WIND DIRECT ACTION ON THE SOLAR PANELS

2.1 The influence of the building upon the velocity and pressure field

The shape and size of the building has a major influence on the alterations of the velocity field. The analysis of the roof terrace of a rectangular building (fig. 2), shows that the streamlines deflect when meeting a rigid obstacle. A detachment point emerges when the wind flow streamlines reaches in the area of the exposed in-wind edge, an aerodynamic leap resulting together with the development of negative wind pressures [3].Whenever a sufficient length of the roof is insured, the wind streamlines might reattach, developing areas with positive pressure (fig. 2a).

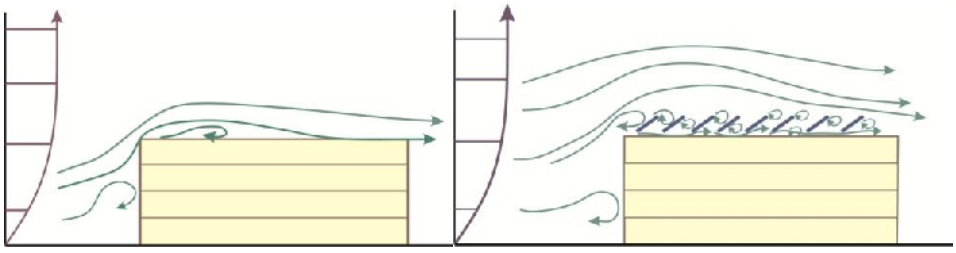

a. b.

Figure 2. Air flow over the flat roof: a.) - roof without solar panels(adapted from Cook N. J., 1985); b.) - roof with solar panels

The presence of the solar panels on the roof increases the complexity of the air flow conditions thus, cumulating the influence of the building and the rows of the solar panels. The reattaching distance of the streamlines is much larger and small eddies are formed between consecutive rows of panels. The aerodynamic leap of streamlines is affected by the dimensions of the building and particularly, by the height and geometry of the rows of solar panels.

The first row of panels is subjected to wind pressure, depending on the ratio between the height of the building and the height of the solar panels. The wind pressure distribution must be evaluated when it is necessary, as depending on the presence of parapets on the edge perimeter. According to the conclusions via numerous researches developed in the Laboratory of Buildings Aerodynamics of the Faculty of Civil Engineering and Building Services from Iaşi [4, 5, 6], the influence of the parapet must not be

neglected, at any rate (fig. 3). If in the case of a parapet with reduced depth the decrease of the pressure coefficients is not relevant, whenever the depth becomes significant (about 1.0 m) wind pressure reduces drastically in the first row of the solar panels.

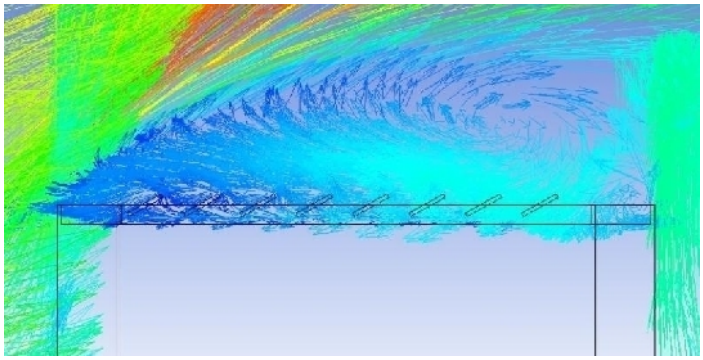

a.

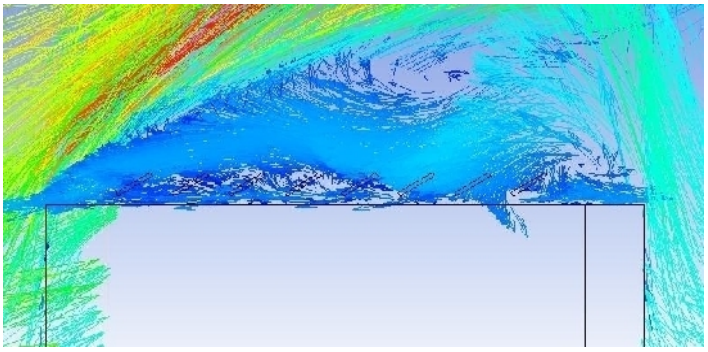

b.

Figure 3. Influence of the parapet upon the wind flow over the solar panels: a.-roof with parapet of 1.0 m depth, b.-roof without parapet [7]

The solar panels rows increase the deflection of the wind flow lines (aerodynamic leap) engendered by the in-wind flow on encountering the volume of the building. In the case of higher parapets, the screening effect is more evident; as an example, in fig. 3 a the first row of solar collectors is mostly subjected to wind local pressure.

A stepped roof (fig. 4) will further alter the streamlines and the field pressure distribution accordingly; alterations will consequently affect the panel array as well. The difference between high and low parapet gather significance in this situation.

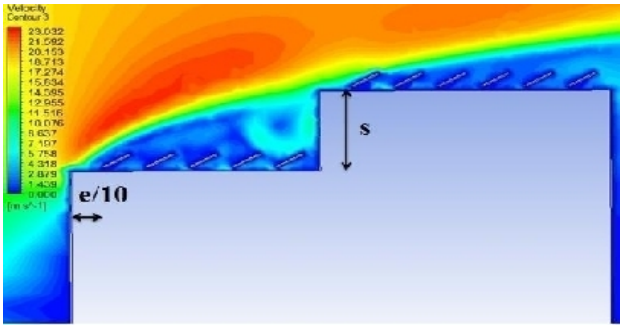

Figure 4. Wind action upon the rows of solar collectors placed on a stepped roof

2.2. Influence of the array of solar panels on the surface of the flat roof

If the roof is sloped, the solar panels may be placed in two different possible ways: inserted in the roofing system or fixed on the top of roofing layers, parallel with the slope. In case of the flat roofs there are many more possibilities of placing the solar collectors (panels), every solution having its particularities. As an example, the panels may be aligned in consecutive rows (fig. 2b) or grouped (fig. 5), parallel with one edge of the roof or even in a skew position with respect to the edges. A certain distance *e* may be left between the panels and the edge (fig. 4a), or sometimes this distance is missing at all. However, the literature recommends a minimum distance to be maintained from edges of the roof, mentioned in the standard regulations SR EN 1991:1-4 as *e/10* defining *e* with:

$$e = min\,(b, 2h) \tag{2}$$

In the relationship (2) *b* is the dimension of the edge normal to the wind direction and *h* is the height of the building.

Other possibilities refer to placing the panels directly on the roof level (fig. 5a) or to mount them at a certain height above this level (fig. 5b). In this last case it must be known that wind flow acts underneath the panels with increased turbulence, resulting in small eddies with negative pressures.

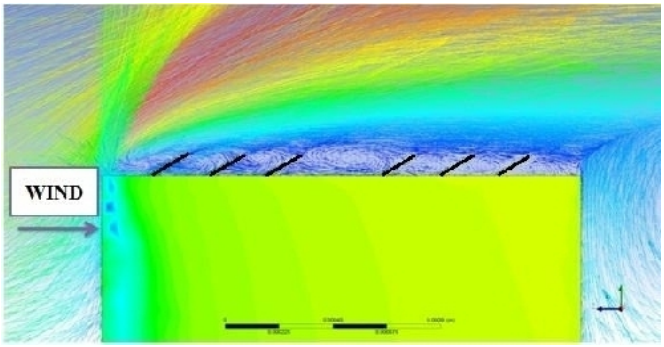

a.

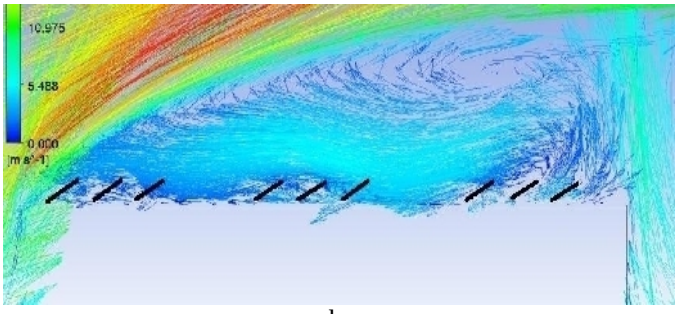

b.

Figure 5. Groups of solar panels placed on terrace: a.- directly on the roof level[8], b. – mounted at a certain distance above the roof level

The supporting system of the panels may be opened or closed, the last solution modifying totally the aerodynamics of the roof (fig. 6). In this case the wind flow will act similar as in the case of a roof with multiple sheds, to which the design loads will increase induced by snow deposits.

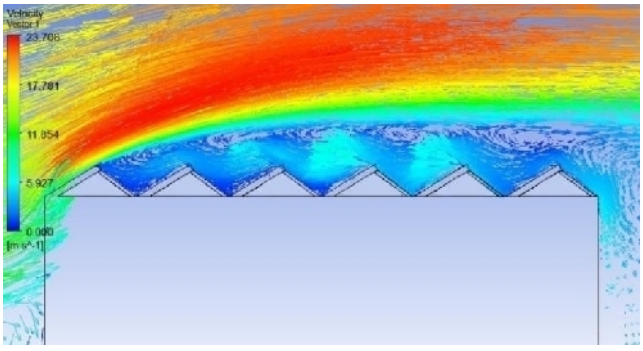

Figure 6. Vectors field of the wind speeds over a closed support system of the panels with deflectors

The evaluation of the normal and tangential components of the wind action upon the solar panels is very difficult owing to the lack of specific data in the codes for the design to wind actions. This is one of the situations calling for tests in atmospheric boundary layer tunnels, which are the only able to reproduce the natural phenomenon; the results obtained are realistic values of wind pressure coefficients and the benefit consists in the optimization of the design of these supporting systems.

2.3. Influence of wind direction of action

Other parameter in the evaluation of the wind loading on solar panels is the incidence angle with respect to the building and also to the panels array. From the point of view of increasing the energy obtained the panels must be oriented on the S, S-SE, S-SV directions but not always the dominant direction of wind action is considered in the arrangements of the solar panels rows.

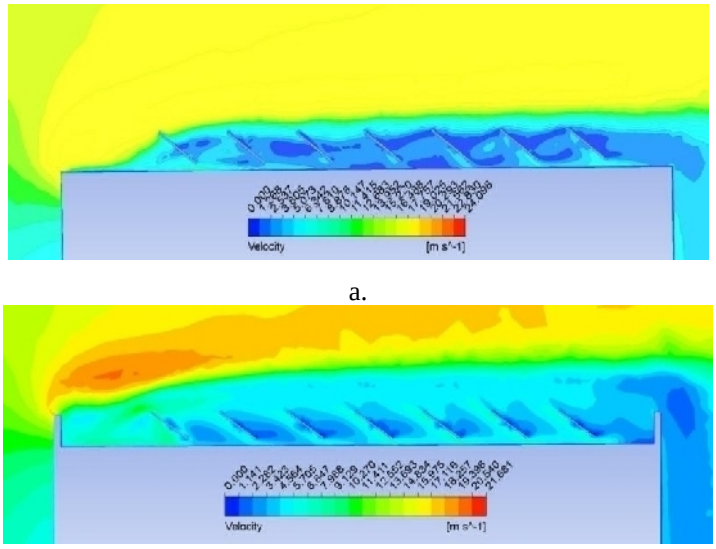

a.

Figure 7. Influence of wind direction of action (180°) upon the distribution of speeds and pressures over the terrace: a. - without parapet, b. – with parapet

Unfavourable situations may rise, such as the case when wind acts from behind the array of panels (fig. 7)or with a tilted direction, when the suction field produces lifting of the panels. Incidence angle between 30º and 60ºwill generate delta-wing vortices in the plane of the roof (fig. 8, 9). The vortices are placed at the roof corners, between the edges parallel to the flow and the

in-wind edge and inside them high negative velocities with increased turbulence manifest [3].

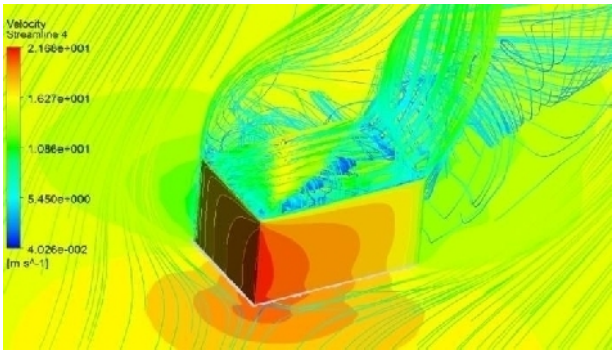

Figure 8. Wind pressures on the building and the roof for incidence at 45°

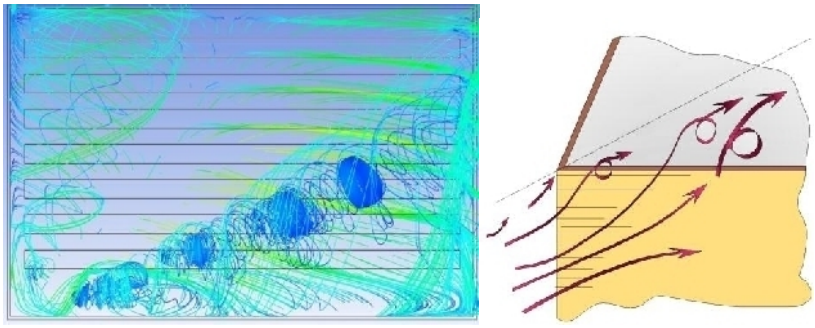

a. b.

Figure 9. Delta wing vortex generation on the roof (a) and at the corners of the buildings (b) for wind incidence between 30º and 60º [6, 7]

A more complex situation is determined by the presence of snow drifts due to wind action combined with snowfalls; large deposits may be scattered over the terrace and between the solar panels and their lengths and heights are not similar with those formed in the absence of the solar panels on a flat roof. As panels are in fact obstacles that shape differently the snow deposits, all the factors involved in the wind evaluation will also affect these agglomerations: wind speed and direction, the solar panels array, the tilting of the panels and the mounting height the distances between panels and between rows and edges of the roof, the presence or the absence of the parapet, the saturation flux of the snow drift and finally the dimensions of the drift itself.

4. CONCLUSIONS

The standard regulations refer only to the necessary data for the design of monopitched canopies to wind action, but do not give explicit data that could be used for the solar panels arrays. There is no data also, about the alteration of the wind pressure coefficients upon the solar collectors with the wind direction of action. By putting into light the numerous factors that influence the distribution of wind pressures in the field of the solar collectors, like direction, intensity and local exposure a real evaluation of the wind loading will be obtained, playing a key role in a safer design of the supporting system.

Experimental studies in the wind tunnels assisted by numerical simulations are beneficial solutions to the uncertainty or even the lack of data and rules for design and exploitation of the solar panels system of producing green energy.

References

1. Ruscheweyh H., Windhovel R., Wind loads at solar and photovoltaic modules for large plants, *Proceedings of the 13th International Conferences on Wind Engineering*, july 10-15, Amsterdam, 2011.
2. Văsieş G., Radu A.,Evaluarea acţiunii vântului asupra construcţiilor în vederea utilizării energiei solare, *Simpozionului National Creatii Universitare 2010* "Evaluarea in constructii", Iasi, Romania, EdituraSocietatiiAcademice „Matei-TeiuBotez", p. 119-130, ISBN 978-973-8955-83-7.
3. Cook N. J., *The designer's guide to wind loading of building structure*. Part 2: Static structures, ISBN 0-408-00871-7, 1990.
4. Axinte E., Modelarea fizică a interacţiunii vânt-structură pentru proiectarae captatoarelor solare, Institutul Politehnic Iaşi, Facultatea de Construcţii, *Teză de doctorat*, Iaşi 1988.
5. Radu A., Axinte E., Theohari C., Steady wind pressures on industrial solar collectors on flat-roofed buildings, *Journal of Wind Engineering and Industrial Aerodynamics*, vol. 23, pp 249-258, 1986.
6. Radu A., Axinte E., Wind forces on structures supporting solar collectors, *Journal of Wind Engineering and Industrial Aerodynamics*, vol. 32, pp 93-100, 1989.
7. Vasies, G., Axinte, E., Teleman, E.C., Numerical simulation of wind action on solar panel placed on flat roofs with and without parapet, *Buletinul Institutului Politehnic din Iasi, Sectia Constructii. Arhitectura,*Tomul LVIII (LXII), Fasc. 1, Editura Politehnium, ISSN 1224-3884 (p), ISSN 2068-4762 (e), p 139-155, Iasi, 2012.
8. Văsieş G., Axinte E., Teleman E. C., The influence of wind direction on the solar panel placed on flat roofs, using CFD simulation, *Proceedings of The 9-th International Symposium „CCE 2011" New Computational Concepts in Civil Engineering*, EdituraSocietatiiAcademice "Matei - TeiuBotez", ISBN 978-606-582-006-7, pp. 158-172.
9. SR EN 1991-1-4/2006, *Eurocod 1: Acţiuni asupra structurilor*. Partea 1-4: Acţiuni generale-Acţiuni ale vântului.

Studies Regarding the Relation Between Wind Velocity Field and Snow Drift on a Flat Roof Equipped with a Solar Panels Array

Georgeta Băetu[1], Elena Axinte[1], Carmen Elena Teleman[1], Victoria Elena Roșca[1], Sergiu Andrei Băetu[2]

[1]*Department of Civil and Industrial Engineering, "Gheorghe Asachi" Technical University, Iaşi, 700050, Romania*

[2]*Department of Structural Mechanics, "Gheorghe Asachi" Technical University, Iaşi, 700050, Romania*

Summary

Violent manifestations of strong wind storms and heavy winters with frequent blizzards and abundant snowfalls are the characteristics of nowadays climatic conditions. The widespread use of the solar panels as a common solution of obtaining unconventional energy implies their presence on the roofs of buildings. In the case of terraces, the pattern of the air flow is generally altered due to the solar panels because it originates important snow agglomerations on the flat roof. Both the shape and the amount of the snow deposits increase significantly in this case. As the design codes do not cover these particular situations, studies on scaled models in atmospheric boundary layer wind tunnels in parallel with numerical simulations are important in order to identify the critical areas of drifting and to evaluate their importance in the structural design.

KEYWORDS: wind action, snow drift, wind tunnel, numerical simulation, solar panels, flat roofs.

1. INTRODUCTION

The codes for design of buildings to climatic loading do no offer comprehensive data necessary for estimating the wind and snow loads on solar panels. According to SR EN 1991-1-3:2005 [14, 15], the snow agglomerations on the roof surface depend on several factors like the roof geometry, the angle of the roof surface, the amount of heat radiated through the roof, the presence of neighbouring buildings, the local meteorological climate, the nature of wind and the rainfall. The uneven distribution of the snow deposits under the effect of wind drifting is important to be evaluated for the design of the roofs of buildings and the particular case of the flat roofs equipped with solar panels, the air flow pattern is diverted and altered in their presence, the aerodynamic pressure field being thus influenced with direct

consequences on the snow deposits [1, 2]. The areas affected by snow agglomerations are those affected by the flow streamlines because they entrain the snow particles, moving them on the surface of the roof.

Numerous studies developed by researchers, like Tsuchiya and his collaborators [3] showed that the formation of snow deposits on roofs surface is influenced by the wind direction and velocity, the snow quality, temperature, the shape of the building and the neighbouring environment. There is a strong connection between the wind speeds and snowdrift phenomenon: the analysis of the influence of gravity, inertia and lift forces that characterize the mechanics of the movement of a snow particle (fig. 1), Tsuchiya makes the following observations:

- the gravitational and the lifting forces are in equilibrium when the snow particles moves horizontally in the air,
- the decrease of the wind speed results into the decrease of the lift force, hence the speed of snow particle increase; due to the difference between the snow and the air density, the snow particle falls and lodge,
- increasing the wind speed implies an increase of the lift force too, which in turn, will defeat gravity generating a further entraining of the snow particle in movement.

The study on models in the wind tunnel are directed towards the analysis of snow deposits on the flat roof equipped with solar panels, highlighting the areas where the snow forms drifts having patterns corresponding to the specific conditions imposed for snow and wind actions, like wind direction, positions of the solar panel rows, shape of the roof, etc.

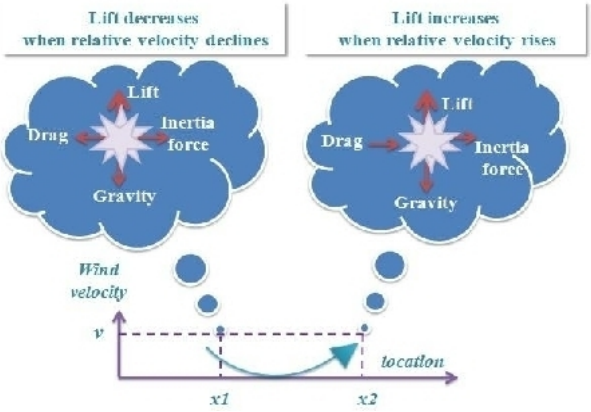

Figure 1. Behaviour of snow particles in area where wind speed in changing (adapted from Tsuchiya et al., [3])

Leitl [4] identifies three possibilities of behaviour of snow particles entrained in wind flow, presented in figure 2, which is the horizontal movement in creeping, saltation and suspension. The horizontal movement is produced by snow particles by rolling on the surface of the existing snow layer [5].

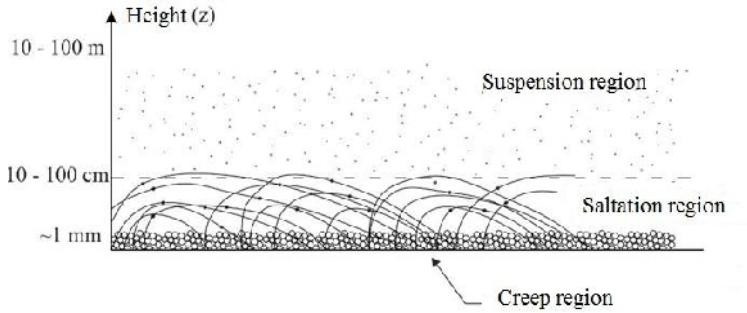

Figure 2. Areas of snow movement (adapted from Sundsbø, [13])

The saltation of the small and medium-sized deposited particles is induced by a sufficiently high wind speed. In this case, the snow particles are lifted and carried in short and medium distances, prior to falling again in the snow layer. By contrast, the particles that are very small are blown away and remain suspended in the air stream. According to Inversen [6, 7], the physical modelling of the phenomenon in the atmospheric boundary layer must be able to replicate the saltation phenomenon which happens predominantly in the first few centimetres above the existing snow layer. But this physical modelling of snowfall in the presence of wind action at the wind tunnel scale is quite difficult due to the complexity of the behaviour of snow particles and hence of the difficulty of respecting the scaling laws.

2. THE INFLUENCE OF SOLAR PANELS ON SNOW DEPOSITS FORMED AT THE ROOF LEVEL

Snow deposits vary according to the manner and the location of solar panels. In the case of the solar panels placed at ground level in consecutive rows, the shape of drifts is similar to that shown in Figure 3. If the solar panels are mounted on a structure leaving a free space from the ground, the shape of snow drifts are like in figure 4 [1].

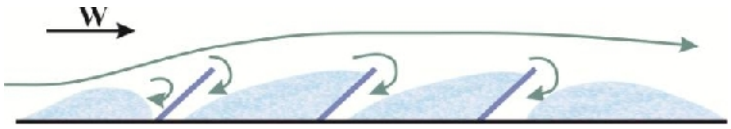

Figure 3. The shape of snow deposits in front and rear the solar panels placed at the ground level [1]

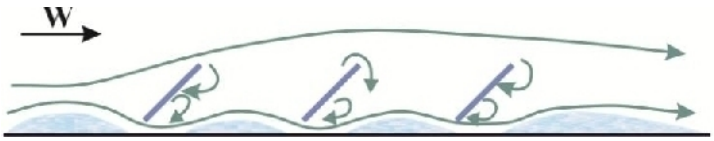

Figure 4. The shape of snow deposits if the solar panels are mounted from the ground level [1]

The snow deposits resulted from drifting on flat roof free from any obstacles will be very different from those generated by the blizzard in encountering a roof equipped with several solar panels disposed in consecutive rows. In the first case, if the roof is large enough, the diverged streamlines due to the building presence will reattach to the roof surface [8, 9, 10, 11]. Solar panels layout in consecutive rows increases and maintains the deflection of the aerodynamic pressure so he reattaching streamlines will move further in leeward of the roof. This manifestation is reflected by the snow deposits forming on the roof terrace. We may say that the presence of the solar panels on the roof surface increases the wind turbulence and reduces air velocity, favouring the agglomeration of a larger snow quantity on the roof [1]. In figure 6 the agglomeration of snow on the roof terrace with parapet is presented schematically.

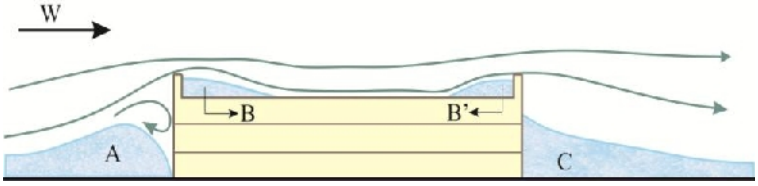

Figure 5. Formation of deposits of snow on the roof terrace [1]

Both the position and the magnitude of the areas where drifted snow reaches saturation and the extension of the ablation dependent directly on the wind speed at the specific location.

3. PHYSICAL MODELLING OF SNOW AGGLOMERATIONS AND NUMERICAL SIMULATION OF WIND FLOW OVER A FLAT ROOF WITH SOLAR PANELS

This paper presents the results obtained by physical modelling in atmospheric boundary layer of the snowfall in the presence of wind action, in order to put I evidence the interaction between air velocity, angle of wind action on the snow deposits formed in the field of a group of solar panels located on the roof terrace of a storied building. In parallel, a numerical simulation of the velocity field was developed in order to identify the strong connection between the particularities of the wind speeds and pressures field to the snow drifting.

The building considered for the numerical simulation and physical modelling has five levels and the dimensions of 21x15x15 meters at full scale. On the roof terrace eight rows of solar panels are placed parallel to the 21 meters building edge, at 0.30 m above the roof plane. Numerical simulation and physical modelling are scaled at 1:50 (fig. 6). The two methods were chosen in order to highlight the correlation between physical modelling and numerical simulation.

a. b.

Figure 6. Experiments in SECO2 wind tunnel: a.- the model of the building with solar panels, b.- simulation of blizzards

The physical modelling of the snowstorm is achieved by using a granular material (glass micro-beads) that simulates the snow. During the physical modelling, the recorder averaged wind speed at the reference height (building height) was 4m/s. The snowdrift was studied in the following cases:

- building with parapet of 1.00 m and incident wind angle of 0°;
- building with parapet attic of 1.00 m and incident wind angle of 180°;
- building without parapet and incident wind angle of 0°;
- building without parapet and incident wind angle of 180°.

The numerical simulation of air flow over the field of solar panels was run for a wind speed of 12 m/s and a turbulence intensity of 20%. The local pressures produced by the wind on the surfaces of the solar panels was measured by considering a network of measuring points on each side of panels. The wind local pressure was measured in 24 points on each side of the panel and the resultant of these local pressures was determined by processing the data. Monitoring the pressures distribution on each individual panel and on the entire row was achieved by analyzing the local and global values, comparing the pressures corresponding to the average on the 8 rows of panels.

So the monitoring of the pressures distribution was the result of a local analysis on each panel of the row and an overall analysis in which the average pressures corresponding to the all eight rows of panels were compared (fig. 7b).

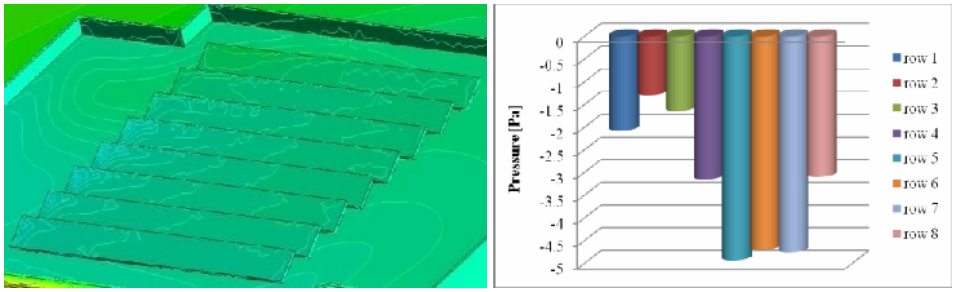

a. b.

Figure 7. Numerical simulation of air flow on solar panels field: a.- pressure contour; b.- mean pressure values on each row, for wind angle of 0°

4. RESULTS

Arrangements in parallel rows of solar panels on the roof reduce the wind speed above the field of mutually shielding panels and panel lines result in local agglomerations of important quantities of snow.

The formation of snow deposits is favoured by the presence of the array of solar panels in consecutive parallel rows, the decreasing wind speed above the panels group and the shielding effect of panels individually. In the case of a roof with parapet free from obstacles (fig. 5), important deposits of snow occur in the close proximity of the parapet, in areas where wind speed decreases. By contrast, in the central area of the roof equipped with solar panels, due to air circulation under the panels combined with diminishing shelter effect produced by the parapet, snow accumulates in quasi-uniform layers without causing congestion. Through physical modelling of blizzards in the wind tunnel, it is observed the influence of the size of the deposits of snow on the roof by the presence or absence of the parapet and the direction of wind action. Figure 8 summarizes snow deposits obtained through the snow drifts on the roof terrace, for each of the four cases considered.

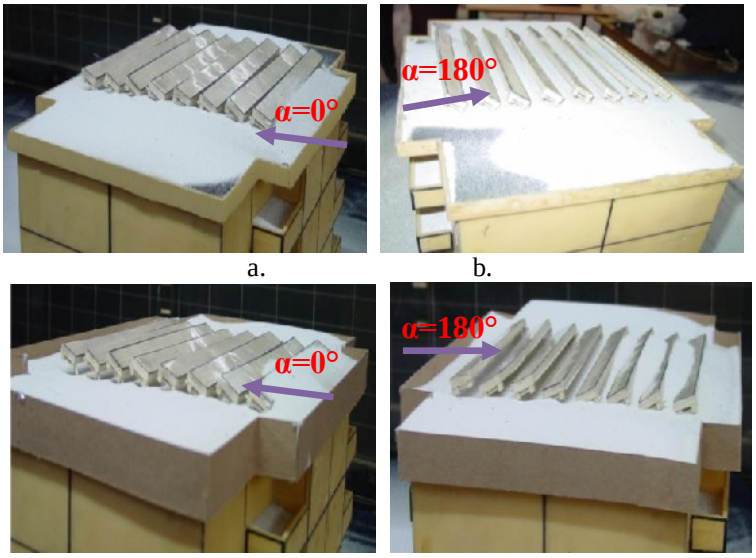

a. b.

c. d.

Figure 8. Snow agglomeration on the roofs surface: a.- building without parapet, wind at 0°; b.- building without parapet, wind at 180°; c.- building with parapet, wind at 0°; d.- building with parapet, wind at 180°

A detailed analysis of wind combined with snow action on the group of solar panels located on the model of the roof terrace, revealed a good correlation between the data obtained by numerical simulation and the physical modelling, for the building with parapet and wind action at 0 ° and 180 °, respectively. For the both directions of wind, the group of solar panels was immersed in a negative pressure bulk and high intensity of turbulence, developed under aerodynamic pressure field produced by the impact of the streamlines with the edge of the roof (attic). In the case of the building with parapet and wind action at 0^0, large amounts of snow are deposited on the side areas of the panels group. Agglomerations of snow occur also in the area between the edge of the parapet and the first row of solar panels, as well as on its surface (fig. 9).

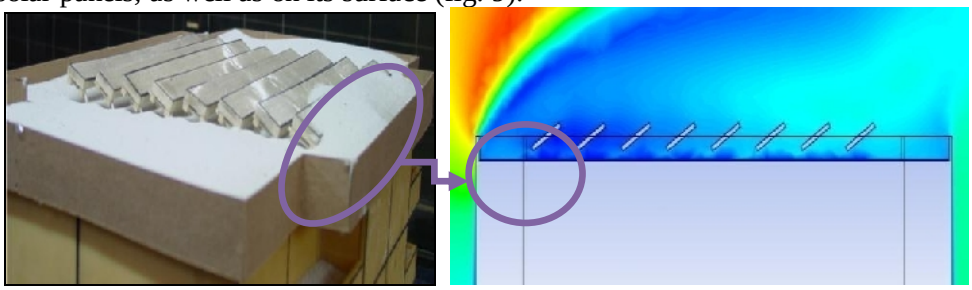

a. b.

Figure 9. Deposits of snow formed in the area with low wind speed: a.-physical modelling, b.-numerical simulation

The presence of these deposits (fig. 8) is connected to the results obtained by the numerical simulation because their locations correspond to the area in which the speed of the airflow is reduced (fig 10, 11).

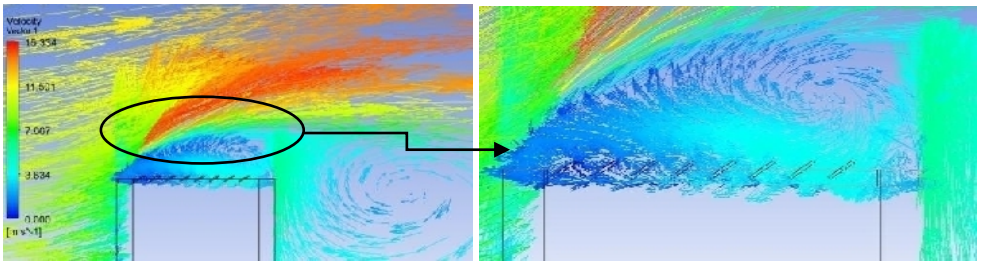

a.

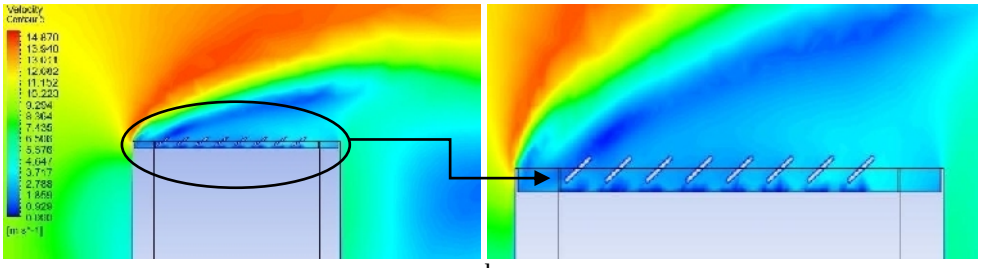

b.

Figure 10. Velocity vector (a) and contour (b) for wind angle of 0°

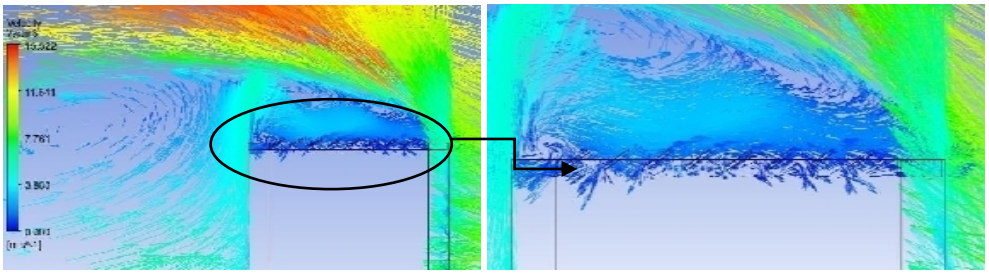

a.

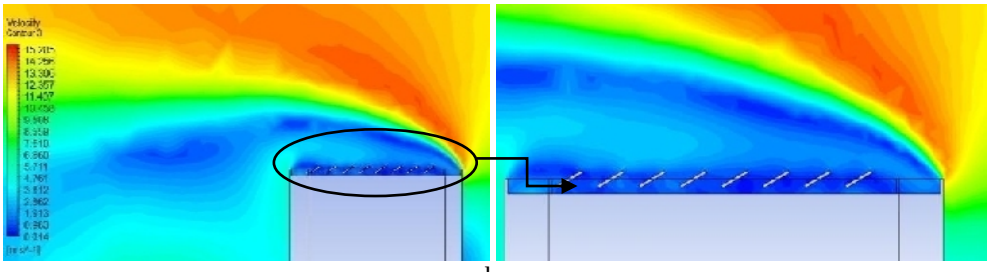

b.

Figure 11. Velocity vector (a) and contour (b) for wind angle of 180°

Inside the field of solar panels, the persistence of the deviation of the aerodynamic pressure field and the sheltering produced by the rows of panels, prevent from gathering the snow in large quantities. Small deposits of snow occur in the areas between consecutive lines, areas where wind speed is reduced due to shielding effect of panels. Action of the wind direction at an angle of 180 ° was found to be unfavourable in terms of the amount of snow deposited on the roof surface and inside the field of panels.

It should be noted that even if in the case of the building without parapet the amount of snow between rows of panels is significant (fig. 8b), the lack of parapet allows the drifting of the snow deposit; this doesn't happen in the case of the building with parapet, where snow deposits may reach the height of the parapet.

5. CONCLUSIONS

The geometry and the dimensions of the building substantially influence the pressure distribution on the field of solar panels located on the roof terrace.

Inside the field, the mutual shielding of the individual panels happens more currently when the building has a parapet. The amount of snow agglomeration on the roof terrace with solar panels depends on the parapet height and angle of the wind action. The largest deposits develop when wind acts behind the group of panels, under an incident angle between 120° and 240 °, reaching to the situation in which the height of deposits is comparable to the height of the parapet. The presence of the parapet favours the increase of snow deposits in the area between the roof edge and the first row of panels, but decreases the deposits inside of the group. On the other hand, the lack of parapet determines the agglomeration of snow to move in the central area the roof, inside the solar panel's group and on both sides of it (fig. 8a, b). With regard to buildings provided with parapets, a solution of reducing the heavy local agglomerations consists in placing a permeable parapet, which allows air infiltration inside of the group of panel entraining the creeping snow particles.

References

1. Axinte, E., Teleman, E., Vasies, G., Rosca V., Extreme actions of snow drift caused by wind on built environment in the context of global climatic changes, *International Multidisciplinary Scientific GeoConference & EXPO – SGEM*, SGEM Conference Proceedings, ISSN: 1314-2704, pp. 311-318.
2. Vasies, G., Axinte, E., Teleman, E., Wind action on solar panels placed on flat roofs with parapets, *Proceedings of the 10th Intenational Symposium Computational Civil Engineering 2012*, Iasi, Romania, ISSN 2285-2735, pp.393-401, 2012.
3. Tsuchiya M., Tomabechi T., Hongo T., Ueda H., Wind effects on snowdrift on stepped flat roofs, *Journal of Wind Engineering and Industrial Aerodynamics*, Vol. 90, pp. 1881 – 1892, 2002.

4. Leitl B., Schatzmann M., Baur T., Koenig-Laglo G., Physical modeling of snow drift and wind pressure distribution at the proposed german antarctic station NEUMAYER III, *25th International Conference on Offshore Mechanics and Arctic Engineering*, Hamburg, Germany, 2006.
5. Thiis T. K., Gjessing, Y., Large-scale measurements of snowdrifts around flat-roofed and single-pitch-roofed buildings, *Cold Regions Science and Technology*, vol 30, pp. 175-181, 1999.
6. Inversen J.D., Smal-scale modeling of snow-drift phenomena, *Congress "Wind Tunnel Modeling for Civil Engineering"*, Gaithersburg, Maryland, U.S.A, pp. 522-540., 1982.
7. Inversen J.D., Drifting-snow similitude – transport – rate and roughness modeling, *Journal of Glaciology*, Vol 26(94), pp. 393 – 402, 1979.
8. Radu Radu, A., Axinte, E., Wind forces on structures supporting solar collectors, *Journal of Wind Engineering and Industrial Aerodynamics*, Vol. 32, pp. 93-100, 1989.
9. Radu, A., Axinte, E., Teohari, C., Steady wind pressures on solar collectors on roofed buildings, *Journal of Wind Engineering and Industrial Aerodynamics*, Vol. 23, pp. 249-258, 1986.
10. Vasieş, G. Axinte, E., Teleman, E. C., Numerical simulation of wind action on solar panel placed on flat roofs with and without parapet, *Buletinul Institutului Politehnic din Iaşi*, Tomul LVIII (LXII), Fasc. 1, Secţia Construcţii. Arhitectură, pp. 139 – 155, 2012.
11. Ruscheweyh H., Windhovel R., Wind loads at solar and photovoltaic modules for large plants, *Proceedings of the 13th International Conference on Wind Engeneering*, Amsterdam, 2011.
12. N. G. Cook Cook N. J., The designer's guide to wind loading of building structures. Part 1: Background, damage survey, wind data and structural classification, *Building Research Establishment Report*, ISBN: 0-408-00870-9, 1985.
13. Sundsbø, P. A., Bang, B., Calculation of snow drift around roadside safety barriers, *Proceedings of the international snow science workshop 1998*, Sunriver, Oregon, pp. 279–283, 1998.
14. SR EN 1991-1-3/2005, Eurocod 1: *Acţiuni asupra structurilor*, Partea 1-3: Acţiuni generale – Încărcări date de zăpadă (in Romanian).
15. SR EN 1991-1-4/2006 Eurocod 1: *Acţiuni asupra structurilor*, Partea 1-4: Acţiuni generale - Acţiuni ale vântului (in Romanian).

Use of Constitutive Equations for Fatigue Simulations

Lucia G. Barbu[1,2], Xavier Martinez[1,3], Sergio Oller[1,2] and Alex H. Barbat[1,2]
[1]*Centro Internacional de Métodos Numéricos en Ingeniería, CIMNE, Barcelona, 08034, Spain*
[2]*Departamento RMEE, Universitat Politècnica de Catalunya, Barcelona, 08034, Spain*
[3]*Department of Nautical Science and Engineering – UPC, Pla de Palau 18, 08003 Barcelona, Spain*

Summary

The mechanical phenomenon known as fatigue consists in the loss of material strength, and consequent failure, due to the effect of periodic loads. Fatigue is characterized, among other parameters, by the number of cycles, load amplitude and reversion index. Material failure is produced by an inelastic behavior, micro-cracking and crack coalescence, which lead to the final collapse of structural parts. This paper disseminates on the use of constitutive equations of plasticity and damage to numerically simulate the entire range of fatigue: high-cycle, low-cycle and ultra-low-cycle. The theoretical model will be presented as well as some numerical examples.

KEYWORDS: constitutive law, cyclic behavior, stiffness reduction, strength reduction.

1. INTRODUCTION

The fatigue phenomenon is defined in the ASTM E1823 standard as: "the process of permanent, progressive and localized structural change which occurs to a material point subjected to strains and stresses of variable amplitudes which produce cracks which lead to total failure after a certain number of cycles" [1].

While there is a general agreement that for failures in the range of 10^6 to 10^8 cycles the structure has failed in the “High Cycle Fatigue” (HCF) range, there is not such agreement in defining the limits for “Low Cycle Fatigue” (LCF) and “Ultra Low Cycle Fatigue” (ULCF). Authors such as Kanvinde and Deierlein [2] consider that LCF is found between 100s and 1000s cycles and that ULCF is in the range of 10-20 cycles; and other authors, such as Xue [3], put these limits in 10^4 for LCF and 100 for ULCF. However, despite these discrepancies, there is a general agreement that plastic behavior of the material plays an important role in the failure due to LCF or ULCF, while damage plays an important role in the failure of HCF and LCF [4].

The current paper presents a new constitutive model specially developed for the prediction of material failure produced by HCF, LCF and ULCF. The agreement obtained between experimental and numerical results allow considering the

proposed law an excellent tool for the simulation of fatigue under regular cycles and non-regular cyclic loading / seismic conditions, as it allows predicting the strength capacity of a material under any given seismic load or assessing its residual strength once the seismic load has already been applied.

According to the literature review made by Yao and Munse in [5], first attempts to characterize LCF and ULCF can be attributed to Kommers who, in 1912, conducted several tests on a cantilever specimen subjected to cyclic bending. After these tests he reached the conclusion that the magnitude of deflection plays an important role in low cycle fatigue. However, main efforts to characterize the parameters driving LCF and ULCF are not found until 1950s, when numerous experimental programs where carried out to calibrate the material constants for various metals. A large amount of work is documented from this period. The experimental data is usually plotted on a log–log scale with the abscissa representing the number of life cycles and the ordinate the plastic strain amplitude. This graph is known as the $\Delta\varepsilon^p - N$ curve. Following this approach, probably the most known, and most widely used, procedure to predict material failure under LCF and ULCF is the Manson-Coffin law ([4], [6] and [7]).

An interesting approach to characterize low cycle fatigue accounting for non-regular cycles is the one proposed by Jiang et al. [8], that defines an independent continuous cumulative damage function (EVICD) based on the accumulation of plastic strain energy. Another interesting approach based on damage accumulation is the one proposed by Kanvinde and Deierlein ([2], [9] and [10]). These authors, in order to account for the effects of void growth and coalescence that drive the fracture of metallic materials, propose a model that calculates the void growth and compares it with a critical value to detect material failure. This parameter is obtained experimentally. The initial formulation developed for monotonic cases (Void Growth Model - VGM [9]) is extended to cyclic loads by differentiating the void growth obtained in the tensile and compressive regions of the load cycle.

This formulation, as well as the formulation proposed by Jiang et al. [8], is capable to account for regular and non-regular cycles, as both formulations are based on the addition of certain quantities while the material increases its plastic strain. However, they both have the drawback of being based on a failure criterion that is completely independent of the constitutive model: It is calculated as the simulation advances and, when it reaches certain level, the criterion tells the code that the material has failed.

Regarding the HCF phenomenon, it is known that the type of fracture involved at macroscale level occurs with little or no plastic deformation ([4], [11]). Therefore, HCF does not introduce macroscopic plastic strain, but it introduces porosity [12]. These are the reasons that have led to describe this failure mode by means of damage models. These can be categorized into five groups: damage curve approach, crack growth- based approach, life curve modification approach, energy

based damage theories and continuum damage mechanics (CDM) approaches [13]. However, in spite of the great number of models proposed in the HCF field, there is not yet a universally accepted one.

In particular, the CDM approach is based on the original concepts of Kachanov [14, 15] for treating creep damage problems. The posterior work of Chaboche [16, 17], Chaboche and Lemaitre [18 ,19], Wang [20], Wang and Lou[21], Li et al. [22] and Oller et al. [23] established the CDM framework as a valid alternative to the fracture mechanics formulations in order to asses in a unified way both crack initiation and propagation. Furthermore, they enhanced the study of fatigue problems by recognizing that the theoretical structure of continuum mechanics, such as damage, is suitable for the study of nonlinear fatigue problems and that the mechanical effect known as fatigue produces a loss of material strength as a function of the number of cycles, load amplitude, reversion index, etc.

Regarding fatigue life prediction, many different approaches have been proposed such as the early methods of stress-life approach and strain-life approach [24]. One of the most used models is based on the Palmgren-Miner linear damage law [25, 26]. However, such models do not recognize the effects of prior history of loading, or the load sequence on the subsequent life. Strain-life models, on the other hand, account for the local plasticity effects at stress concentrations regions [27]. Information is abundant in literature as there are many different crack initiation models [28], with a large number of empirical models proposed for the long crack growth prediction [29]. Despite the abundant information existent on fatigue constitutive models, there are none able to simulate all three types of fatigue with the same non-linear constitutive equation.

Current work proposes simulating the material failure due to HCF, LCF and ULCF using a material non-linear model. This approach will allow the simulation of regular and non-regular cycles, as well as obtaining the post-critical response of the structure when the material has failed.

A material non-linear model is defined by the thermodynamic law that drives the material performance and a yield criterion defining the stress level that triggers the non-linear behavior ([30], [31]). The constitutive law proposed herein is characterized by the combination of plasticity and damage. These two material laws have been already coupled by several authors proposing different models. These models vary in their complexity, versatility and accuracy. Some of them are those of Simo and Ju [32], Lubliner et al. [33], Luccioni et al. [34] and, more recently, Armero and Oller [35].

The necessity of combining these two laws is based on the following assumption: the plastic phenomenon leads to the distortion of metal voids and their coalescence. This effect is responsible of the permanent deformations obtained after steel yielding, characteristic of plasticity. However, this process does not account for the formation or nucleation of new voids, which may reduce the material stiffness [36].

In order to include this effect in the material behavior, it is necessary a new law complementing plasticity. An increment of the voids in the metal leads to a reduction of the effective area, resulting also in a reduction on the material stiffness. This effect will be simulated with a damage law.

2 PLASTIC DAMAGE MODEL FORMULATION

The theories of plasticity and/or damage can simulate the material behavior beyond the elastic range, taking into account the change in the strength of the material through the movement of the yield and/or damage surface (isotropic and kinematic) due to the inelastic behavior (plasticity and damage) of each point of the solid. However they are not sensitive to cyclic load effects. In this work the standard inelastic theories are modified to introduce the fatigue effect coupled with non-fatigue material behavior.

It is assumed that each point of the solid follows a damage-elasto-plastic constitutive law (stiffness hardening/softening) ([33], [34] and [37]) with the stress evolution depending on the free strain variable and plastic and damage internal variables. The formulation proposed herein studies the phenomenon of stiffness degradation and irreversible strain accumulation through the combined effect of damage and plasticity.

Since this work is oriented towards mechanical problems with small elastic strains and large inelastic strains, the free energy additively hypothesis is accepted $\Psi = \Psi^e + \Psi^p$ ([30], [38]). The elastic Ψ^e and plastic Ψ^p parts of the free energy are written in the reference configuration for elastic Green strains $E_{ij}^e = E_{ij} - E_{ij}^p$; the last variable operates as a free field variable [23], [30], [39] and [33]. The free energy is thus written as

$$\Psi = \Psi^e(E_{ij}^e, d) + \Psi^p(\alpha^p) = (1-d)\frac{1}{2m^o}\left[E_{ij}^e C_{ijkl}^o E_{kl}^e\right] + \Psi^p(\alpha^p) \tag{1}$$

Considering the second thermodynamic law (Clausius-Duhem inequality – [38], [40] and [41]), the mechanical dissipation can be obtained as [30]:

$$\Xi = \frac{S_{ij}\,\dot{E}_{ij}^p}{m^o} - \frac{\partial \Psi}{\partial \alpha^p}\dot{\alpha} - \frac{\partial \Psi}{\partial d}\dot{d} \geq 0 \tag{2}$$

The fulfilment of this dissipation condition (Equation 2) demands that the expression of the stress should be defined as (Coleman method; see [41])

$$S_{ij} = m^o \frac{\partial \Psi}{\partial E_{ij}} = (1-d)\, \mathrm{C}^o_{ijkl}\left(E_{kl}\right) \tag{3a}$$

Also, from the last expressions, the secant constitutive tensor can be obtained as:

$$\mathrm{C}^s_{ijkl}(d) = \frac{\partial S_{ij}}{\partial E^e_{kl}} = m^o \frac{\partial^2 \Psi^e}{\partial E^e_{ij} \partial E^e_{kl}} = (1-d)\, \mathrm{C}^o_{ijkl} \tag{3b}$$

where m^o is the material density, $E^e_{ij}, E_{ij}, E^p_{ij}$ are the elastic, total and plastic strain tensors, $d^{ini} \le d \le 1$ is the internal damage variable enclosed between its initial value d^{ini} and its maximum value 1, α^p is a plastic internal variable, C^0_{ijkl} and C^S_{ijkl} are the original and secant constitutive tensors and S_{ij} is the stress tensor for a single material point.

2.1 Yield and potential plastic functions

The yield function F^P accounts for the residual strength of the material, which depends on the current stress state and the plastic internal variables and, in the formulation proposed herein, it is sensitive to the fatigue phenomenon. This F^P function has the following form, taking into account isotropic and kinematic plastic hardening (Bauschinger effect [42], [43]):

$$F^P(S_{ij}, \alpha^p) = f^P(S_{ij} - \eta_{ij}) - K^P(S_{ij}, \kappa^p, N) \le 0 \tag{4}$$

where $f^P(S_{ij} - \eta_{ij})$ is the uniaxial equivalent stress function depending of the current value of the stresses S_{ij}, η_{ij} is the kinematic plastic hardening internal variable, $K^P\left(S_{ij}, \kappa^p, N\right)$ is the plastic strength threshold and κ^p is the plastic

isotropic hardening internal variable ([34], [33], and [37]). N is the number of cycles of the stress in the point of the solid and α^p is a symbolic notation for all the plastic variables involved in the process.
Equation (4) incorporates the number of cycles as an internal variable that affects the strength threshold by lowering it as the number of cycles accumulates. This enables the model to also account for strength reduction due to high cycle fatigue effects ([11], [23]) and this in turn shows the potential of the formulation to adjust by itself to the type of fatigue involved.

The evolution law for the plastic strain is $\dot{E}_{ij}^P = \dot{\lambda}\dfrac{\partial G^P}{\partial S_{ij}}$, being λ the consistency plastic factor and G^P the plastic potential.

Kinematic hardening accounts for a translation of the yield function and allows the representation of the Bauschinger effect in the case of cyclic loading. This translation is driven by the kinematic hardening internal variable η_{ij} which, in a general case, varies proportionally to the plastic strain of the material point. One of the laws that define the evolution of this parameter is

$$\dot{\eta}_{ij} = c_k \dot{E}_{ij}^P \text{ ,with } c_k = \frac{2}{3} b_k \text{ for Von Mises} \tag{5}$$

where b_k is a material property to be determined by particular tests for the Prager and Melan kinematic hardening [30]. The evolution of isotropic hardening is controlled by the evolution of the plastic hardening function K^P, which is often defined by an internal variable κ^p. The rate equation for these two functions may be defined, respectively, by

$$\begin{aligned} \dot{K}^p &= \dot{\lambda} \cdot H_k^p = h_k^p \cdot \dot{\kappa}^p \\ \dot{\kappa}^p &= \dot{\lambda} \cdot H_{\mathrm{k}}^p = \dot{\lambda} \cdot \left[h_{\mathrm{k}}^{\mathrm{p}} : \frac{\partial G}{\partial S} \right] = h_{\mathrm{k}}^{\mathrm{p}} \cdot \dot{E}^p \end{aligned} \tag{6}$$

where k denotes scalar and $\mathbf{k}$ stands for a tensor function. Depending on the functions defined to characterize these two parameters, different solid performances are obtained.

2.2 Threshold damage function oriented to fatigue analysis. Phenomenological approach

The effects caused by applying an increasing number of loading cycles are taken into account by means of a proposed $f_{red}(N, S_{\max}, R)$ function. This function is introduced in the above formulation in the expression of the damage threshold surface, $F^D(S_{ij}, d)$, proposed by [32], [41] and [44]. The number of cycles N can then be incorporated as a new variable. This enables the classical constitutive damage formulation to account for fatigue phenomena by translating the accumulation of number of cycles into a readjustment and/or movement of the damage threshold function.

The non-linear behavior caused by fatigue is introduced in this procedure implicitly, by incorporating a fatigue state variable $f_{red}(N, S_{\max}, R)$, that is irreversible and depends on the number of cycles, the maximum value of the equivalent stress in the material $S_{\max}$, and on the factor of reversion of the equivalent stress, $R = \dfrac{S_{\min}}{S_{\max}}$. This new variable affects the residual strength of the material by modifying the damage threshold, $F^D(S_{ij}, d, N)$, either on the equivalent stress function $f^D(S_{ij})$ (equation 7a), or on the damage strength threshold

$$F^{D'}(S_{ij}, d, N) = \underbrace{\frac{f^D(S_{ij})}{f_{red}(N, S_{\max}, R)}}_{f^{D'}(S_{ij}, N, R)} - \overline{K}^D(S_{ij}, d) \le 0 \tag{7a}$$

$$F^{D''}(S_{ij}, d, N) = f^D(S_{ij}) - \underbrace{\overline{K}^D(S_{ij}, d) \cdot f_{red}(N, S_{\max}, R)}_{K^{D'}(S_{ij}, d, N)} \le 0 \tag{7b}$$

$\overline{K}^D(S_{ij}, d)$ (equation 7b) [23].

In the above, $f^{D'} = f^D / f_{red}(N, S_{\max}, R)$, is the reduced equivalent stress function in the undamaged space, $K^{D'}(S_{ij}, d, N)$ is the fatigue damage strength threshold, and $d = \int_0^t \dot{d}\,dt$ the damage internal variable.

The evolution of the damage strength threshold is analogous to that of the plastic strength threshold, depending on the internal degradation variable κ^d

$$\dot{K}^D = h_k^d \cdot \dot{\kappa}^d$$
$$\dot{\kappa}^d = h_k^d \cdot \dot{d} \tag{8}$$

In equation 8, h_k^d is a scalar function with scalar arguments and h_k^d is a scalar function with tensorial arguments as shown by (34, 33, and 37).

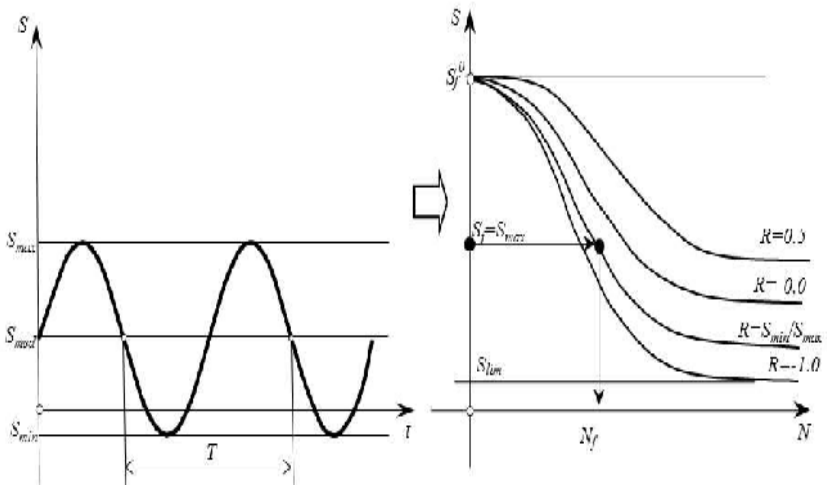

Figure 1.a. Stress evolution at a single point; b. S-N (Wöhler’s) Curves

The evolution of the damage variable is defined as

$$\dot{d} = \dot{\mu} \frac{\partial F^D}{\partial f^D} \tag{9}$$

being μ the consistency damage factor, which is equivalent to the consistency plastic factor defined in [30]. Consequently, for the isotropic damage case,

$$\dot{d} = \frac{\dot{\mu}}{f_{red}} \tag{10}$$

2.3 Function of residual strength reduction for fatigue – Wöhler curve definition

Wöhler or "Stress-Num. of cycles" (S-N) curves are experimentally obtained by subjecting identical smooth specimens to cyclic harmonic stresses and establishing their life span measured in number of cycles. The curves depend on the level of the maximum applied stress and the ratio between the lowest and the highest stresses (R=Smin/Smax). Usually, S-N curves are obtained for fully reversed stress (R=Smin/Smax=-1) by rotating bending fatigue tests.

S-N curves are, therefore, fatigue life estimators for a material point with a fixed maximum stress and a given ratio R. If, after a number of cycles lower than the cycles to failure, the cyclic load stops, a change in the material's elastic threshold is expected due to accumulation of fatigue cycles. Furthermore, if the number of cycles exceeds Nf, being Nf the fatigue life as resulting from Figure 2, the material will fail with the consequent reduction of strength and stiffness. The change in strength is quantified by the strength reduction function $f_{red}(N, S_{\max}, R)$, while the change in stiffness is taken into account by means of the damage parameter.

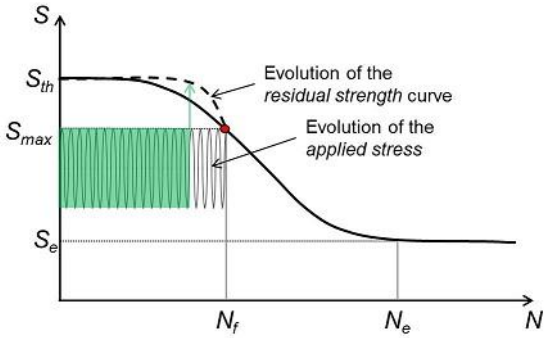

Figure 2. Schematic representation of the evolution of the residual strength with the applied load and number of cycles

In the case of a cyclic load with constant S_{max} and R throughout the entire life of a material, the S-N curve is sufficient for determining fatigue life. However, when dealing with different load interactions the main focus resides on the residual strength curve. The curve quantifies the loss of strength in the material as the number of cycles accumulates and as load characteristics change.

All fatigue numerical simulations are based on the Wöhler curves obtained experimentally. These curves are described in an analytical form with the help of

material parameters. Their expression, as well as the analytical definition of the strength reduction function, is connected to the experimental curve and, therefore, subjected to change if the material changes. Different analytical definitions can be found in [45], [46] and [47], as well as in [23].

2.4 Coupled plastic-damaged response and tangent constitutive law

From the simultaneous consistency conditions for the plastic ($\dot{F}^P = 0$) and damage ($\dot{F}^D = 0$) problems, the evolution of the plastic strain and damage variables can be obtained. The secant constitutive law and the stress rate are

$$\begin{aligned} S_{ij} &= (1-d)\,\mathrm{C}^o_{ijkl}\,(E_{kl} - E^p_{kl}) \\ \dot{S}_{ij} &= \frac{\partial}{\partial t}\left[(1-d)\mathrm{C}^o_{ijkl}\,(E_{kl} - E^p_{kl})\right] = \mathrm{C}^e_{ijkl}\,\dot{E}_{kl} - \mathrm{C}^p_{ijkl}\,\dot{E}^p_{kl} \\ \mathrm{C}^e_{ijkl} &= \mathrm{C}^s_{ijkl} - \frac{1}{(1-d)}\frac{\partial G^D}{\partial g^D}\left[\left(\frac{\partial g^D}{\partial S^0_{rs}}\right)\mathrm{C}^o_{rsij}\right] S_{kl} \end{aligned} \tag{11}$$

Considering the stress rate as $\dot{S}_{ij} = \mathrm{C}^{ep}_{ijkl}\,\dot{E}_{kl}$, the analytical expression of the tangent constitutive tensor is

$$\mathrm{C}^{ep}_{ijkl} = \mathrm{C}^e_{ijkl} - \frac{\mathrm{C}^s_{ijrs}\frac{\partial G^P}{\partial S_{rs}}\frac{\partial F^P}{\partial S_{mn}}\mathrm{C}^e_{mnkl}}{-c_k\frac{\partial F^P}{\partial \eta_{tu}} : \frac{\partial G^P}{\partial S_{tu}} - \frac{\partial F^P}{\partial \alpha^p_r}(h_r)_{tu}\frac{\partial G^P}{\partial S_{tu}} + \frac{\partial F^P}{\partial S_{mn}}\mathrm{C}^s_{mnrs}\frac{\partial G^P}{\partial S_{rs}}} \tag{12}$$

2.5 Algorithm for the numerical implementation of the plastic-damaged model

For this model, plasticity and damage equation must be integrated simultaneous. This is done with the following Euler-backward algorithm. Between two-equilibrium configurations t and $t-\Delta t$ the formulation is updated as follows:

$$\begin{aligned} \left(E^p_{ij}\right)_t &= \left(E^p_{ij}\right)_{t-\Delta t} + \Delta\lambda \cdot \left(\frac{\partial G^P}{\partial S_{ij}}\right)_t \\ \left(\alpha^p\right)_t &= \left(\alpha^p\right)_{t-\Delta t} + \Delta\lambda \cdot \left(H(S_{ij}, \alpha^p)\right)_t \\ \left(\eta_{ij}\right)_t &= \left(\eta_{ij}\right)_{t-\Delta t} + \Delta\lambda \cdot c_k \cdot \left(\frac{\partial G^P}{\partial S_{ij}}\right)_t \\ \left(d\right)_t &= \left(d\right)_{t-\Delta t} + \Delta d_t \end{aligned} \tag{13}$$

The stress state is updated according to the secant constitutive law shown in equation (11) and its reduction to the damage and plastic yield surfaces is done simultaneously leading to the following non-linear system of equations:

$$\begin{aligned} H^P(\Delta\lambda_t, \Delta d_t) &= F^P(S_{ij}, \alpha^p) = f^P(S_{ij} - \eta_{ij}) - K^P(S_{ij}, \kappa^p, N) = 0 \\ H^D(\Delta\lambda_t, \Delta d_t) &= F^D(S_{ij}, d) = f^D(S_{ij}) - K^D(S_{ij}, d, N) = 0 \end{aligned} \tag{14}$$

This system of equations can be solved by Newton-Raphson procedure [48]

$$\begin{Bmatrix} \Delta\lambda_t \\ \Delta d_t \end{Bmatrix}_k = \begin{Bmatrix} \Delta\lambda_t \\ \Delta d_t \end{Bmatrix}_{k-1} - \begin{bmatrix} \left(\frac{\partial H^P}{\partial \Delta\lambda}\right)_t & \left(\frac{\partial H^P}{\partial \Delta d}\right)_t \\ \left(\frac{\partial H^D}{\partial \Delta\lambda}\right)_t & \left(\frac{\partial H^D}{\partial \Delta d}\right)_t \end{bmatrix}_{k-1}^{-1} \begin{Bmatrix} H^P(\Delta\lambda_t, \Delta d_t) \\ H^D(\Delta\lambda_t, \Delta d_t) \end{Bmatrix}_{k-1} \tag{15}$$

Despite having the analytical expression of the tangent constitutive tensor, equation (12), the calculation of this tensor is extremely costly and, depending on the yield and damage functions used, its approximation does not provide correct results. To overcome this drawback this tensor will be calculated numerically by a perturbation method. This is obtained as:

$$C^{ep}_{ijab} = \frac{\delta \dot{S}_{ij}}{\delta \dot{E}_{ab}} \tag{16}$$

with $\delta \dot{E}_{ab}$ an infinitesimal perturbation applied to the mechanical strain tensor, and $\delta \dot{S}_{ij}$ the stress variation produced by the strain perturbation. With this procedure, it is necessary to apply $2 \times a \times b$ perturbations to obtain the complete tangent tensor. However, despite the computational cost, it provides an accurate approximation that improves the global convergence of the problem [49].

3. PLASTIC DAMAGE MODEL ORIENTED TO FATIGUE ANALYSIS

The effects of a cyclic load on the constitutive behavior of a material range from the accumulation of plastic strain in the case of ULCF to the reduction of material stiffness when dealing with high cycle fatigue. LCF induces changes in the material that are a combination of the aforementioned phenomena. In the following the methodology and motivation for taking into account the effects generated by the cyclical load will be presented.

3.1 Ultra-low cycle fatigue

The model is able to account ULCF effects by incorporating a new law, especially developed for steel materials, that has been designed to reproduce their hardening and softening performance under monotonic and cyclic loading conditions (Figure 3). This law depends on the fracture energy of the material.

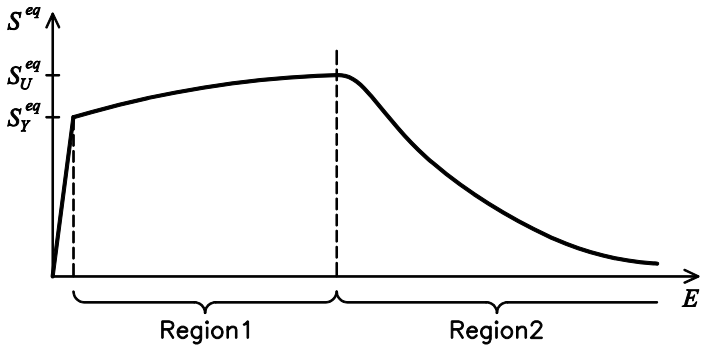

Figure 3. Evolution of the equivalent stress

The equivalent stress state shown in Figure 3 has been defined to match the uniaxial stress evolution shown by most metallic materials. This curve is divided in two different regions. The first region is defined by fitting a curve to a given set of equivalent stress-equivalent strain points. This curve is a polynomial of any given order and is fitted by using the least squares method. The data given to define this region is expected to provide an increasing function, in order to obtain a good performance of the formulation for cyclic analysis.

The second region is defined with an exponential function to simulate softening. The function starts with a null slope that becomes negative as the equivalent plastic strains increases. The exact geometry of this last region depends on the fracture energy of the material. The exact formulation of the constitutive law can be found in Martinez et al. [50].

Characteristic of this type of fatigue is the Bauschinger effect that is taken into account in the constitutive model by combining isotropic hardening with kinematic hardening. The energy dissipated in each hysteresis loop is monitored and failure under cyclical loads is reached when the total available fracture energy of the material is spent.

The plastic damage formulation presented in this paper can be used to improve result accuracy when simulating the softening behavior under ULCF loads.

3.2 Low cycle fatigue

The behavior of a material subjected to cyclical loads that induce low cycle fatigue (LCF) exhibits both accumulation of plastic strain and a reduction of stiffness (Figure 4). While ULCF can be described exclusively by plastic models and HCF by damage models, LCF should be modelled with coupled plastic damage models. It is often difficult to predict at which moment in the material life stiffness reduction begins, since the boundaries between these types of fatigue are rather arbitrary. The model this paper proposes aims at making a contribution in correctly assessing the fatigue life for materials subjected to ULCF and LCF and is particularly effective for the transition zone between these two phenomena.

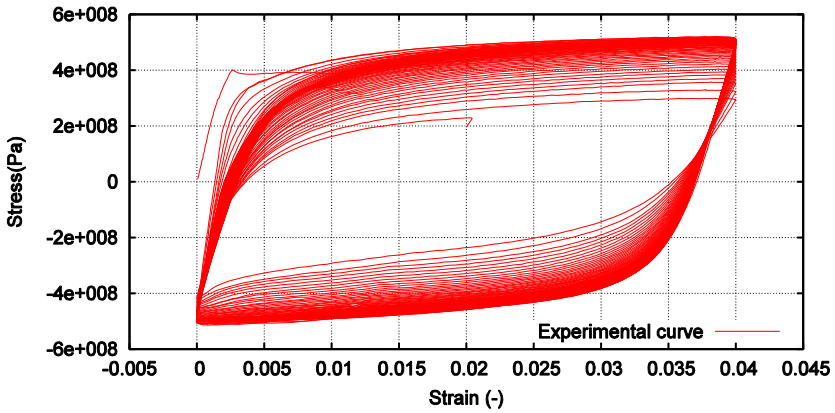

Figure 4. Experimental stress-strain curve for X52 steel [51]

In the context of the hardening law proposed for ULCF, the plastic damage model presented in this work activates itself in the softening region. This is justified by the physical implications behind the damage phenomenon, as damage induces porosity that leads to stress relaxation. This implies that region 1 in Figure 3 is governed by plasticity ensuring that only the cyclical loads that last a long enough number of cycles get to experience damage effects. This is important as the formulation is meant to guarantee that, for a material life clearly in the ULCF range (dozens of cycles or less), the constitutive equations governing should be those of

plasticity. By regulating the extension of region 1 with respect to region 2 discrimination is made between materials that exhibit more sensitivity to ULCF with respect to LCF or the opposite.

The hardening law proposed in Figure 3 marks as the onset of softening the level of equivalent plastic strain inputted by user [50]. This is the triggering point for the plastic damage model to activate itself. At this point the total energy dissipated by the plasticity model has been quantified and, by subtracting it from the total fracture energy of the material, the energy available for the plastic damage model is obtained.

The next issue to be addressed is then: how much energy goes to the plasticity model and how much to the damage model? The following law is proposed in order to assess this issue, where N is the number of cycles the material has been subjected to, up until the first increment when softening begins, $\lim_{ULCF}$ is the limit between the ULCF domain and the LCF one and $\lim_{HCF}$ is the limit between the LCF domain and the HCF one (Figure 5):

$$p\%_{dam} = \frac{(N - \lim_{ULCF})}{(\lim_{HCF} - \lim_{ULCF})} \times 100 \tag{17}$$

The percentage of energy allocated to plasticity is the complementary part, $p\%_{plast} = 100 - p\%_{dam}$. By multiplying these percentages to the energy available for the softening process, $G_f^{soft} = G_f - G_f^{hard}$, the nominal energy for each process is obtained: $G_f^{soft,plast} = G_f^{soft} \times p\%_{plast}$ and $G_f^{soft,dam} = G_f^{soft} \times p\%_{dam}$.

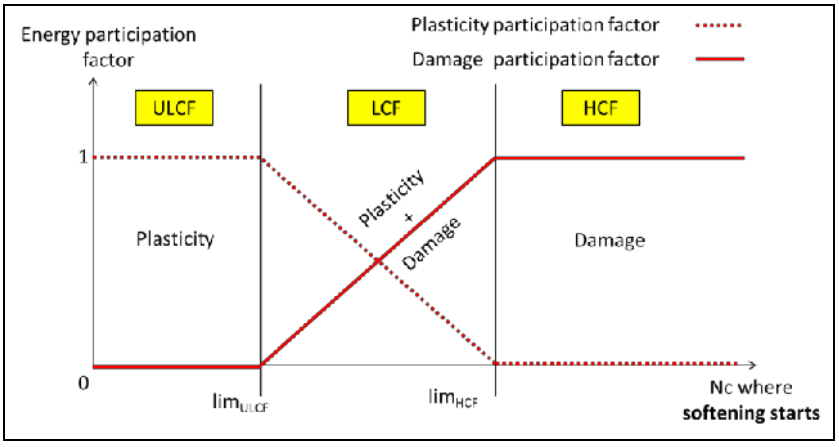

Figure 5. Schematic representation of the energy distribution law in softening over the entire fatigue domain (X axis not scaled).

If at the onset of softening the number of cycles recorded is lower than the $\lim_{ULCF}$, then the $p\%_{dam} = 0$ and $p\%_{plast} = 1$, thus marking the behavior as completely governed by plasticity. When the number of cycles is greater than the limit between LCF and HCF then the entire energy available for the softening part goes to damage.

Although the energy distribution law is formulated in a straightforward and simple manner, the main difficulty lies in correctly assessing the number of cycles considered as a limit in between ULCF and LCF, and LCF and HCF. These limits can be derived statistically if an experimental program is available for small scale specimens. However, the statistical analysis has to be made taking into account the loading cycle when softening begins, not when the sample has failed (e.g. total life of the sample).

These limits are material dependent, as each material exhibits a different behavior in terms of the vulnerability to ULCF or HCF conditions. Consider for instance two materials that exhibit the same fatigue life for certain straining amplitude, but have different onsets for the softening process. The stress –strain hysteresis loop is different and a more accurate monitoring of the exact onset of softening leads to a finer tuning in terms of strain based design.

4 ADVANTAGES OF THE APPROACH PROPOSED

To prove the ability of the model to simulate monotonic and cyclic tests made on steel, in the following are compared the results obtained from the numerical model with the results obtained from experimental tests performed at the Universidade do Porto in the framework of the ULCF project. The tests were performed on an X52 steel.

The data used to define the numerical model has been obtained adjusting the solution of the model to the results of the experimental tests. To do so, it has been necessary to take into account that the effects of the kinematic and the isotropic hardening laws are coupled. This implies that the definition of the first region of isotropic hardening cannot be obtained from the experimental curve straightforward, as this curve does not take into account the displacement of the yield surface due to the kinematic hardening law. The most relevant parameters of the model are described in the following table.

Table 1. Mechanical properties of steel X52

Young Modulus	$2.05 \cdot 10^5$	MPa
Poisson Modulus	0.30	
Elastic Stress (σ_Y^{eq})	270	MPa
Plastic Strain Softening (E_2^p)	27	%
C1 kinematic hardening	$5.0 \cdot 10^4$	MPa
C2 kinematic hardening	450	
Fracture Energy	8.0	$MN \cdot m/m^2$

Previous results [50],[52] have shown that the proposed constitutive equation is capable of predicting material failure after applying several cycles to the material; it has shown also that the number of cycles depends on the plastic strain amplitude and, finally, that this is a logarithmic variation (as it was expected). However, these capabilities do not present major advantages compared to other approaches such as the Coffin-Manson rule, or any other analytical expression capable of defining the maximum number of cycles that can be applied for a given plastic strain.

The main advantage of the proposed approach is that the prediction of ULCF failure does not depend on the plastic strain applied, but on the energy dissipated during the cyclic process. Therefore, it is possible to vary the plastic strain in the cycles applied to the structure and the constitutive model will be still capable of predicting the material failure.

This is proved in the following example, where an irregular load, in frequency and amplitude, is applied to the material (Figure 6a). This load will provide the stress-strain response plotted in Figure 6b. As it can be seen, the load applied produces several loops, each one with a different plastic strain.

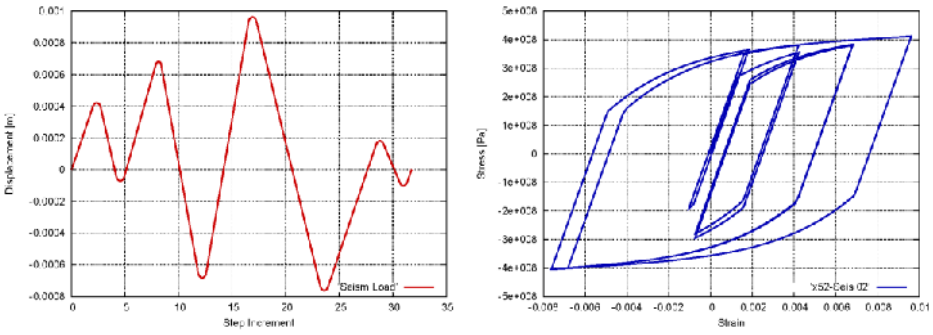

Figure 6. Seismic-type load applied (a) and material stress-strain response (b)

The model is capable of capturing the energy dissipated in each one of these loops and, therefore, to evaluate the fracture energy available in the material after having applied the load. In the following figure it is shown the response if a monotonic load is applied after two repetitions of the load depicted in Figure 6a. This response is superimposed with the response of a monotonic load. The result obtained shows that these two cycles have dissipated some energy and, therefore, the maximum strain reached by the model before failure is lower than the strain reached with the monotonic test.

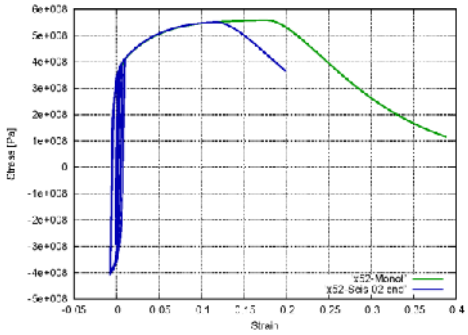

Figure 7. Response of the material after applying two seismic-type cycles

It is also possible to repeat several times the irregular load, shown in Figure 6a, to study the number of repetitions that are required to reach material failure. Figure 8 shows the stress-strain response of the material after twelve seismic-type cycles. This graph shows that in the last six cycles the stress developed by the material has been reduced, which allows to conclude that the material can hold only six cycles of the load described.

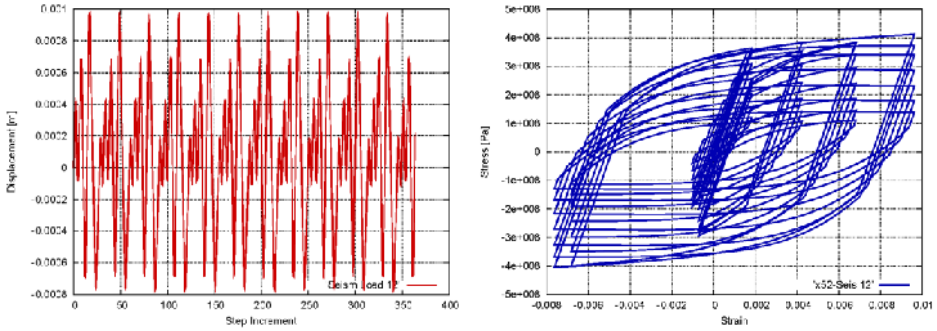

Figure 8. Response of the material after twelve seismic-type cycles

5 CONCLUSIONS

This document has presented a constitutive model to characterize the mechanical performance of steel, capable of taking into account the isotropic and kinematic hardening effects. The size of the yield surface is determined by the isotropic hardening law that depends on the amount of energy dissipated by the material.

Preliminary results, made on the material, show that the simulation of steel with the proposed approach is capable of capturing the effect of fatigue in the material. Moreover, the model not only is capable of predicting the failure for a specific cyclic load, but it is also capable of predicting the material failure for cyclic irregular loads.

Acknowledgements

This work has been supported by the Research Fund for Coal and Steel through the ULCF project (RFSR-CT-2011-00029), by the European Research Council under the Advanced Grant: ERC-2012-AdG 320815 COMP-DES-MAT "Advanced tools for computational design of engineering materials", by the research collaboration agreement established between Abengoa Research and CIMNE and by the Spanish Government program FPU: AP2010-5593.

References

1. ASTM Standard E1823-13. *Standard Terminology Relating to Fatigue and Fracture Testing*. ASTM International, West Conshohocken, PA (2013).
2. A.M Kanvinde, G.G. Deierlein. *Micromechanical simulation of earthquake-induced fracture in steel structures*. Technical Rep. 145, John A. Blume Earthquake Engineering Center, Stanford University, California (2004).
3. L Xue, A unified expression for low cycle fatigue and extremely low cycle fatigue and its implication for monotonic loading, *Int. J. Fatigue*, 30, 1691-1698 (2008).
4. F.C. Campbell, *Elements of Metallurgy and Engineering Alloys*, ASM International, Ohio, USA (2008).
5. J.T.P. Yao and W.H. Munse. *Low-cycle fatigue on metals - Literature review*. Technical Report SSC-137. Ship Structure Committee (1963).
6. H.D. Solomon, G.R. Halford, L.R. Kaisand, B.N. Leis. *Low Cycle Fatigue: Directions for the Future*. ASTM STP942 technical papers (1988).
7. M. Kuroda. Extremely low cycle fatigue life prediction based on a new cumulative fatigue damage model. *International Journal of Fatigue*, 24(6): 699-703 (2002).
8. Y. Jiang, W. Ott, C. Baum, M. Vormwald, H. Nowack, Fatigue life predictions by integrating EVICD fatigue damage model and an advanced cyclic plasticity theory. *International Journal of Plasticity*, 25(5): 780-801 (2009).
9. A.M. Kanvinde, G.G. Deierlein, Void growth model and stress modified critical strain model to predict ductile fracture in structural steels. *Journal of Structural Engineering*, 132(2): 1907–1918 (2006).
10. A.M. Kanvinde, G.G. Deierlein, Cyclic void growth model to assess ductile fracture initiation in structural steels due to ultra low cycle fatigue. *Journal of Engineering Mechanics*, 136(6): 701–712 (2007).
11. Barbu, L.G., Oller, S., Martínez, X. and Barbat, A.H. Stepwise advancing strategy for the simulation of fatigue problems. *Proceedings of the 12th International Conference on Computational Plasticity - Fundamentals and Applications, COMPLAS* (2013): 1153-1164.
12. Schijve, J. *Fatigue of Structures and Materials*, 2nd edition, Springer-Verlag, Berlin,Germany (2009).
13. Fatemi, A. and Yang, L. Cumulative fatigue damage and life prediction theories: a survey of the state of the art for homogeneous materials, *International Journal of Fatigue* (1998) **20**:9-34.
14. Kachanov, L. M. Time to the rupture process under creep conditions, *Izv. Akad. Nauk*. SSR Otd. Tech. Nauk. (1958) 8:26-31.
15. Kachanov, L. M. *Introduction to Continuum Damage Mechanics*, Martinus Nijhoff, The Netherlands (1986).
16. Chaboche, J.L. Fracture mechanics and damage mechanics: complementarity of approaches, In *Numerical Methods in Fracture Mechanics, Proceedings of the Fourth International Conference* (1987) 309-324.
17. Chaboche, J.L. A differential law for nonlinear cumulative fatigue damage, In *Materials and Building Research, Annales de l'ITBTP* (1974) **39**:117-124.
18. J. Lemaitre and J.-L. Chaboche. *Mechanics of Solid Materials*. (1990) Cambridge University Press. New York, USA.
19. Lemaitre, J. and Chaboche J. L. Aspect phenomenologique de la rupture par endommagement, *Journal Mechanique Appliquee* (1978) **2**(3):317-365.
20. Wang, J. A continuum damage mechanics model for low-cycle fatigue failure of metals, *Engineering Fracture Mechanics* (1992) **41**(3):437-441.
21. Wang, T. and Lou, Z. A continuum damage model for weld heat affected zone under low-cycle fatigue loading, *Engineering Fracture Mechanics* (1990) **37**(4): 825-829.
22. Li, C., Qian, Z. and Li, G. The fatigue damage criterion and evolution equation containing material microparameters, *Engineering Fracture Mechanics* (1989) **34**(2):435-443.

23. Oller, S., Salomón, O. and Oñate, E. A continuum mechanics model for mechanical fatigue analysis, *Computational Materials Science* (2005) **32**:175-195.
24. Holman, R. K. , Liaw, P. K., Methodologies for predicting fatigue life, *JOM: the journal of the Minerals, Metals & Materials Society* (1997) **49**(7):46-52.
25. Palmgren, A.,Die Lebensdauer von Kugellagern (The service life of ball bearings), *Zeitschrift des Vereines Deutscher lngenieure* (1924) **68**(14):339-341.
26. Miner, M. Cumulative fatigue damage, *Journal of Applied Mechanics* (1945) **12**:159-164.
27. Vasudevan,A.K, Sadananda, K, Glinka, G. Critical parameters for fatigue damage *International Journal of Fatigue* (2001) **23**(1): 39–53.
28. Halford, G.R. Cumulative fatigue damage modeling—crack nucleation and early growth, *International Journal of Fatigue* (1997) **19**(1):S253-S260.
29. Hoeppner, D. W., Krupp, W. Prediction of component life by application of fatigue crack growth knowledge, *Engineering Fracture Mechanics* (1974), **6**:47-70.
30. J. Lubliner, *Plasticity Theory* (2008) Dover Publications .
31. S. Oller (2014). *Nonlinear Dynamics of Structures*. (2014) CIMNE-Springer, Barcelona, Spain. ISBN. 978-3-319-05193-2.
32. Simo, J.C.; Ju, J.W. Strain- and stress-based continuum damage models. Part I: formulation. *International Journal of Solids and Structures* (1987) **23** (7): 821-840.
33. Lubliner, J., Oliver, J., Oller, S. and Oñate E. A plastic-damage model for concrete, *International Journal of Solids and Structures* (1989) **25**(3):299-326.
34. Luccioni, B.; Oller, S.; Danesi, R. Coupled plastic-damage model. *Computational Methods for Applied Mechanics and Engineering* (1996) **129**(1-2): 81-89.
35. Armero, F.; Oller, S. A general framework for continuum damage models. I. Infinitesimal plastic damage models in stress space. *International Journal of Solids and Structures* (2000), **37**(48-50): 7409-7436.
36. Armero, F.; Oller, S. A general framework for continuum damage models. II. Integration algorithms, with appliactions to the numerical simulation of porous metals. *International Journal of Solids and Structures*, (2000) **37**(48-50): 7437-7464.
37. Oller, S. *Modelización Numérica de Materiales Friccionales* - Monografía CIMNE Nº 3 – Barcelona (1991).
38. Lubliner, J. On thermodynamics foundations of non-linear solid mechanics - *Int. Journal non-linear Mechanics* (1972) **7**: 237-254.
39. A. Green, and P. Naghdi. A general theory of an elastic-plastic continuum. *Archive for Rational Mechanics and Analysis*. 1964, 18(4): 251-281.
40. Malvern, L. Introduction to the Mechanics of Continuous Medium - Prentice Hall USA (1969).
41. Maugin, G. *The Thermomechanics of Plasticity and Fracture*. Cambridge University Press (1992).
42. B.K. Chun, J.T. Jinna and J.K. Lee. Modeling the Bauschinger effect for sheet metals. Part I: theory. *International Journal of Plasticity*. 2002, 18: 571-595.
43. M.E. Kassner, P. Geantil, L.E. Levine and B.C. Larson. Backstress, the Bauschinger Effect and Cyclic Deformation. *Materials Science Forum. Vols. 604-605*: 39-51. Trans Tech Publications. Switzerland, 2009.
44. Oliver, J., Cervera, M., Oller, S., and Lubliner, J. Isotropic damage models and smeared crack analysis of concrete, In *Second international conference on computer aided analysis and design of concrete structures* (1990) **2**:945-958.
45. Salomón, O., Oller, S. and Oñate, E. Fatigue Analysis of Materials and Structures Using a Continuum Damage Model, *International Journal of Forming Processes* (2002) **5:** 493-503.
46. Suero, A. and Oller, S. *Tratamiento del Fenómeno de Fatiga Mediante la Mecánica de Medios Continuos*, Monografía CIMNE Nº 45, Barcelona, Spain (1998).
47. Oller, S., Oñate, E., Canet, J. Miquel and Botello, S. A plastic damage constitutive model for composite materials, *International Journal of Solids and Structures* (1996) **33**:2501-2518.
48. Zienkiewicz, O. C. and Taylor, R. *The Finite Element Method*, 5Th Ed , V 1 and 2, Butterworth-Heinemann, (2000).

49. Martinez, X., Oller, S., Rastellini, F. and Barbat, A. A numerical procedure simulating RC structures reinforced with FRP using the serial/parallel mixing theory, *Computers and Structures* (2008) **86 (**15-16):1604-1618.
50. Martinez, X., Oller, S., Barbu, L. and Barbat, A. Analysis of ultra-low cycle fatigue problems with the Barcelona plastic damage model, *Computational Plasticity XII. Fundamentals and Applications* (2013) 352 – 363, ISBN 978-84-941531-5-0.
51. J.C.R. Pereira, A.M.P. de Jesus, J. Xavier, A.A. Fernandes, B. Martins, Comparison of the monotonic, low-cycle and ultra-low-cycle fatigue behaviors of the X52, X60 and X65 piping steel grades, *Proceedings of the 2014 ASME Pressure Vessels & Piping Conference*, (2014) ASME 2014 PVP, July 20-24, Anheim, California, USA.
52. Barbu, L.G., Oller, S., Martínez, X. and Barbat, A.H Coupled plastic damage model for low and ultra-low cycle seismic fatigue. *11th. World Congress on Computational Mechanics* (2014), p. 2955-2966, ISBN 978-84-942844-7-2.

Time-History Analysis of Reinforced Concrete Bridge Structure by Using Artificial Accelerograms

Georgiana Bunea[1], Dana Ciutea[1] and Gabriela M. Atanasiu[2]
[1] *Master of Structural Engineering, Technical University "Gheorghe Asachi" Iaşi, 700050, Romania*
[2] *Department of Structural Mechanics, Technical University "Gheorghe Asachi" Iaşi, 700050, Romania*

Summary

Time history analysis, which is used in this case, requires the input of accelerogram data. However, for Iasi area there are few accelerograms available which were registered during large magnitude earthquakes. This situation leads to the need of obtaining artificial accelerograms specific for Iasi region, an increased number of this type of data leading to an improvement of the results' quality in what concerns the non-linear dynamic analysis.

The second part of this paper presents the results obtained by performing time-history analysis on a reinforced concrete bridge, using artificial accelerograms. For this paper, three moment magnitudes were considered in generating artificial accelerograms: 7.5, 8 and 8.5. This artificial data are implemented in a structural analysis and design software as an input for time-history analysis.

KEYWORDS: accelerograms, artificial accelerograms, time history, concrete bridge.

1. INTRODUCTION

Bridges are lifeline structures, important links in the infrastructure and their failure during an earthquake will seriously disrupt the circulation of population between emergency locations. It is therefore important that bridges exposed to major earthquakes can survive without structural damages and to be rapidly available for traffic. Several bridges that were subjected to important seismic loading suffer serious damages, due to failure of the structural elements. For this reason, in this paper is studied the behavior of a bridge structure to seismic loading using artificial accelerograms.

There are situations in which the simulation of structural response using an elastic response spectrum is considered inappropriate, and a dynamic analysis is required.

Time histories are used in order to describe the ground motion during an earthquake, and represent graphical representation of the ground acceleration with respect of time. This kind of representations can be obtained by using: artificial accelerograms, synthetic accelerograms and real accelerograms.

For Iasi area there are few accelerograms available which were registered during large magnitude earthquakes. In addition, for the largest earthquake registered in Romania (’77 earthquake), one single complete recording was obtained – in Bucharest. This situation leads to the need of obtaining artificial accelerograms specific for Iasi municipality, an increased number of this type of data leading to an improvement of the results’ quality in what concerns the non-linear dynamic analysis.

2. ARTIFICIAL ACCELEROGRAMS

For developing artificial accelerograms, a *SeismoSoft* software has been used: SeismoArtif, respectively. This program generates artificial earthquake accelerograms which match to a specific target response spectrum. There are several methods of calculation used by SeismoArtif: Synthetic Accelerogram Generation & Adjustment, Artificial Accelerogram Generation, Artificial Accelerogram Generation & Adjustment and Real Accelerogram Adjustment. SeismoArtif software application deals with the three fundamental types of accelerograms: real accelerograms recorded after earthquakes, synthetic accelerograms obtained from seismological models and artificial records consistent with the design response spectrum.

For the purpose of this paper, the Synthetic Accelerogram Generation & Adjustment calculation method will be utilized. By using the Synthetic Accelerogram Generation & Adjustment, it is possible to obtain a series of artificial accelerograms for different earthquake magnitudes which match a certain response spectrum. The advantage of using this method is that it is possible to obtain accelerograms for higher magnitudes than the ones existent in the database.

In Figure 1 is shown the elastic response spectrum used in the analysis, which is in accordance to the Romanian seismic code P100/2012 and it is characteristic for the North-Eastern region.

A number of maximum 8 synthetic accelerograms can be created for a specific moment magnitude, they being used later for the artificial accelerograms generation.

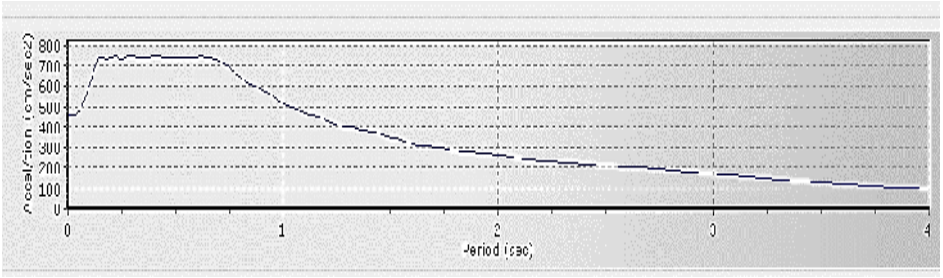

Figure 1. Normalized Elastic Response Spectrum in terms of acceleration, according to P100/2012

The procedure for creating synthetic ground motions is based on the work of Halldorsson and Papageorgiou (2005). The generation criteria used in obtaining synthetic accelerograms are earthquake parameters and soil parameters. In what concerns the earthquake parameters, the moment magnitude of the earthquake must be introduced as input, as well as the distance between the epicenter and the analyzed site. In addition, the type of earthquake regime must be chosen. There are three types available in SeismoArtif application: inter-plate regimes, regimes of active tectonic extension and intra-plate regimes. Vrancea earthquakes are defined by inter-plate regimes.

For this paper, three moment magnitudes were considered in generating synthetic accelerograms: 7.5, 8 and 8.5. The distance between the main event and the station is taken 170 km and the soil influence upon the seismic wave is not taken into account. Figure 2 presents the synthetic accelerograms for 7.5, 8 and 8.5 moment magnitude earthquakes obtained by using SeismoArtif.

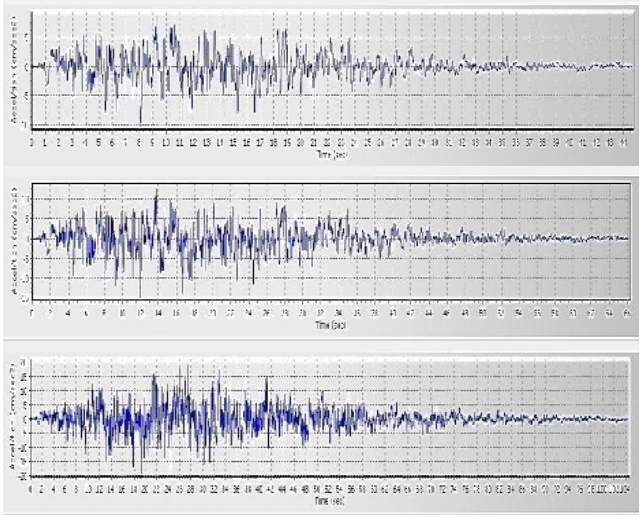

Figure 2. Synthetic accelerograms for 7.5, 8 and 8.5 earthquake moment magnitude

The following step for this calculation method is to generate the artificial accelerograms. A damping coefficient of 5% was considered, along with a time step of 0.02 sec. The synthetic accelerograms obtained in the previous step are matched with the elastic design response spectrum from P100/2012 introduced as input, the result being the artificial accelerograms. Figures 3, 4 and 5 present examples of artificial accelerograms obtained for Iasi region, in case of a 7.5, 8 and 8.5 moment magnitude earthquake, respectively. Four accelerograms were generated for each moment magnitude, a statistics of the obtained results being presented in each case. It contains information on Peak Ground Acceleration, Peak Ground Velocity, Peak Ground Displacement and Significant Duration.

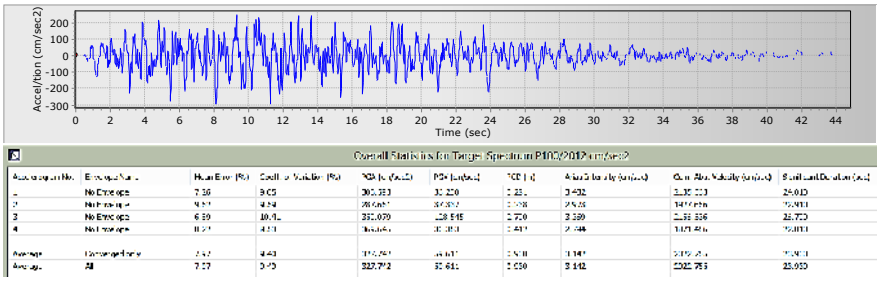

Figure 3. Artificial accelerograms for an earthquake of 7.5 moment magnitude

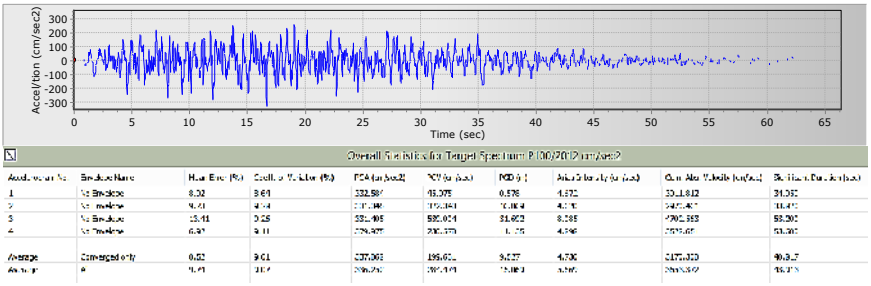

Figure 4. Artificial accelerograms for an earthquake of 8 moment magnitude

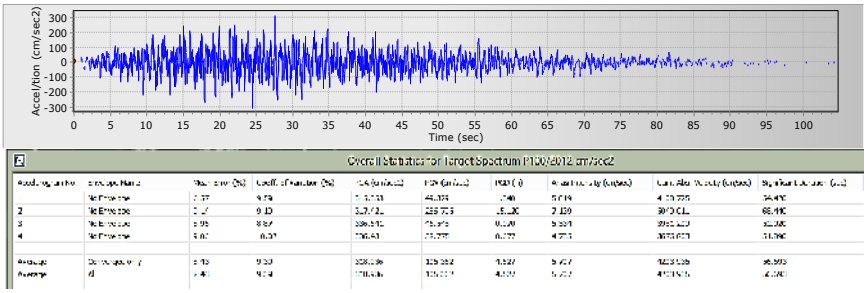

Figure 5. Artificial accelerograms for an earthquake of 8.5 moment magnitude

Another computational program developed by SeismoSoft is SeismoMatch, which is utilized to adjust real accelerograms in order to match a specific target response spectrum. This program uses the wavelets algorithm proposed by Abrahamson [1992] and Hancock et al. [2006], based on the time-domain method of Lilanand and Tseng [1988]. For the biggest seismic event ever recorded in Romania, the 1977 earthquake, only one accelerogram is available and it is characteristic only for Bucharest region. This situation leads to the necessity of obtaining artificial accelerograms specific for other areas, but having the characteristics of the 1977 seismic recording. The considered response spectrum, given in P100/2012, is characteristic for Iasi area, with the corner period $T_C = 0.7s$. The source accelerogram introduced as input is the 1977 recorded acceleration in the North-South direction. Figure 1 is representing the elastic design response spectrum used also in the SeismoMatch analysis and in Figure 6 the input accelerogram is displayed.

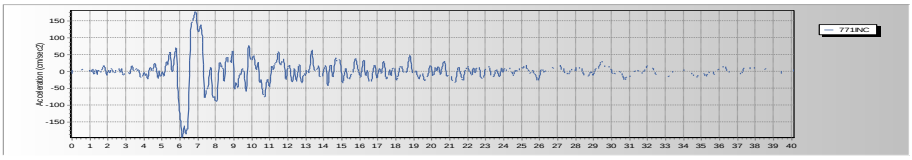

Figure 6. INCERC recorded accelerations of the 1977 Vrancea N-S earthquake

Based on the target response spectrum, SeismoMatch software modified the 1977 accelerogram, the obtained result being presented in Figure 7.

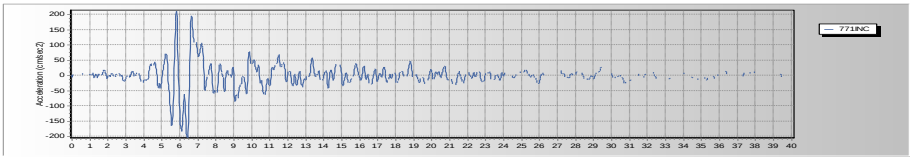

Figure 7. Modified Acceleration time-history of the 1977 seismic record, based on the elastic response spectrum of T_C = 0.7 s

A comparison between the original accelerogram and the one obtained after matching has been done, being illustrated in Figure 8.

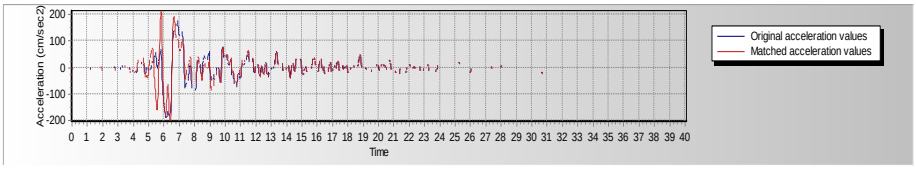

Figure 8. Comparison between the 1977 accelerogram and the artificial accelerogram specific for Iasi region

The Peak Ground Acceleration obtained for the matched accelerogram (212.28 cm/sec^2) is higher than the one registered by INCERC (194.93 cm/sec^2). However, this calculation method does not take into account the distance between the source and Iasi region, smaller values being obtained if this situation is considered. Also, due to the high acceleration values given for the elastic design response spectrum by the seismic code P100/2012, the values of the original accelerogram had to be increased, as illustrated in Figure 9.

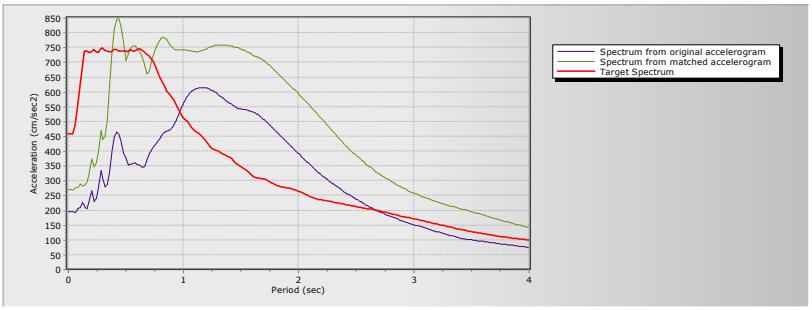

Figure 9. Comparison between the target spectrum, the spectrum from the original accelerogram and the one form the artificial accelerogram

3. BRIDGE STRUCTURAL ANALYSIS

3.1 Description of the bridge

The bridge is designed as an open spandrel arch, with the deck on top connected to the arch with columns. The total span of the bridge is 141.5 m, having 2 spans of 7 m each and 3 spans of 42.5m each. The maximum height is about 10.80m from the ground. The bridge has the main girders as arch systems, which sustain the deck structure.

The arch is made of reinforced concrete with the thickness of 0.4 m and the maximum height at the crown of 3.2 m. The arches are fixed into the columns and represent the primary load-carrying elements of the superstructure. There are two types of columns: ones that resting on ground that are called piers and ones resting on the arch, which are termed spandrel columns. On the central spans, there are eight pairs of spandrel columns, positioned symmetrically on the crown arch, with a constant distance between them of 3.25 m. The bridge deck has a transverse dimension of 6.00m +2x1.00m and a 2.5% inclination at both sides, has two road lanes. The deck section is a solid concrete section of 20 cm thickness and is

supported by spandrel columns and piers and the connection with the abutments is monolithically made.

The substructure is made of massive gravity abutments and reinforced concrete piers with the height of 4.4 m, which are fixed at the bottom level into spread foundations. In order to transfer the axial forces and the bending moments to the bedrock, the foundations have a rectangular section of 7.00x4.00m.

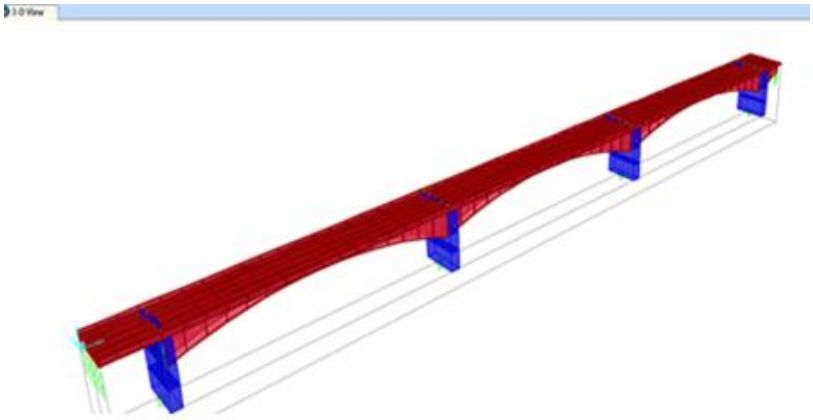

Figure 10. Structural model

3.2 Modal analysis

The principal modes of vibration obtain by using SAP2000 v15.0.0 are presented in Table 1, that provides structure results, including items such as structural periods and frequencies.

Table 1. Modal periods and frequencies

OutputCase	StepType	StepNum	Period	Frequency	CircFreq	Eigenvalue
Text	Text	Unitless	Sec	Cyc/sec	rad/sec	rad2/sec2
MODAL	Mode	1	0.410981	2.4332	15.288	233.73
MODAL	Mode	2	0.336205	2.9744	18.689	349.26
MODAL	Mode	3	0.330782	3.0231	18.995	360.81
MODAL	Mode	4	0.325918	3.0683	19.278	371.66
MODAL	Mode	5	0.297681	3.3593	21.107	445.51
MODAL	Mode	6	0.25336	3.947	24.799	615.01
MODAL	Mode	7	0.205884	4.8571	30.518	931.35
MODAL	Mode	8	0.196448	5.0904	31.984	1023
MODAL	Mode	9	0.183244	5.4572	34.289	1175.7
MODAL	Mode	10	0.173734	5.7559	36.166	1307.9
MODAL	Mode	11	0.170761	5.8561	36.795	1353.9
MODAL	Mode	12	0.169937	5.8845	36.974	1367.1

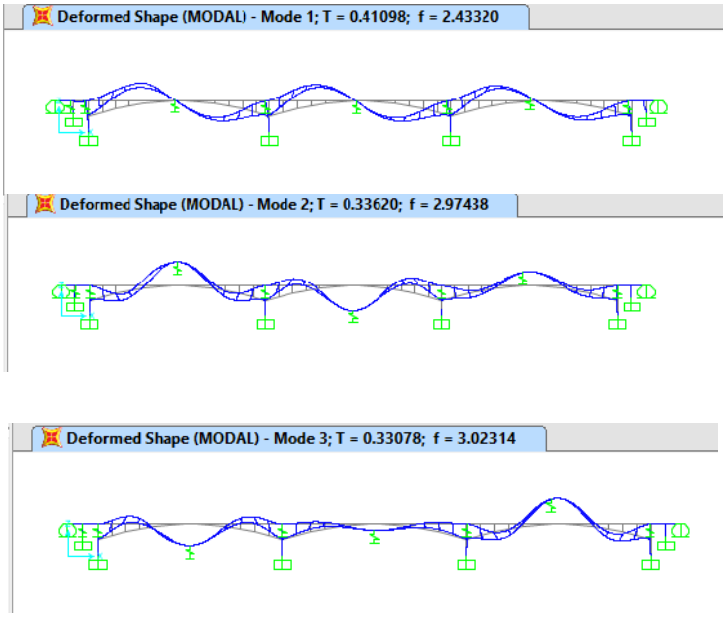

Figure 11. Modes of vibration

3.3 Time history analysis

For performing a time history analysis were utilized the artificial accelerograms obtained by using SeimoSoft and SeismoMatch softwares. The relevant results are:

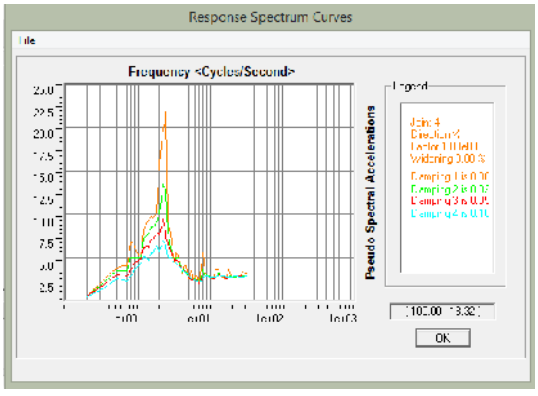

Figure 12. Pseudo Spectral Accelerations obtained for Modified Vrancea ’77 Earthquake motion

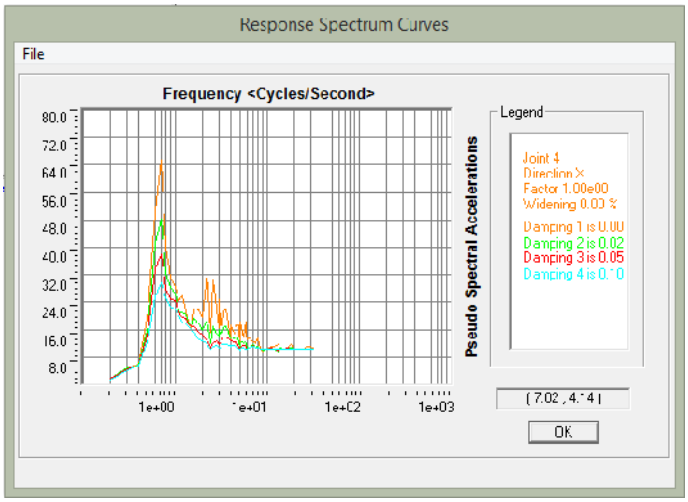

Figure 13. Pseudo Spectral Accelerations obtained for an earthquake of 7.5 moment magnitude

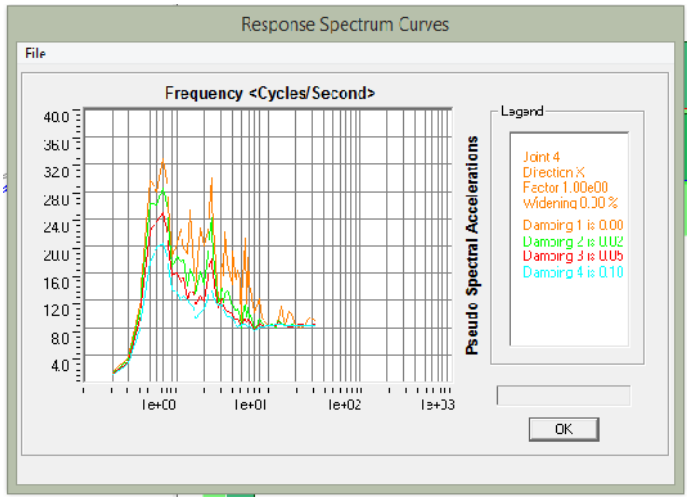

Figure 14. Pseudo Spectral Accelerations obtained for an earthquake of 8 moment magnitude

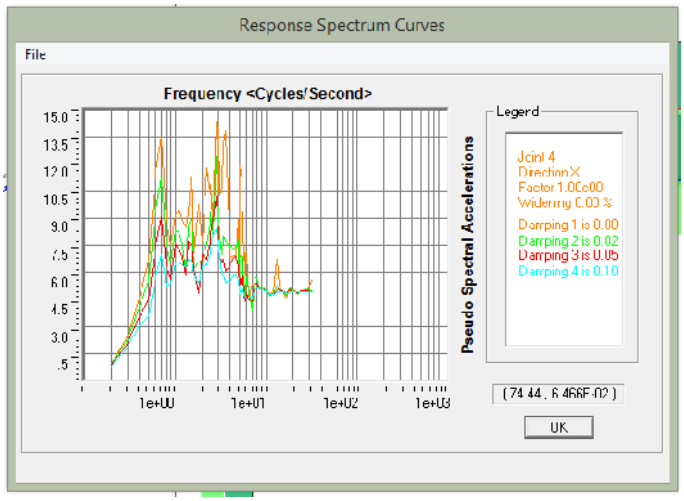

Figure 15. Pseudo Spectral Accelerations obtained for an earthquake of 8.5 moment magnitude

4. CONCLUSIONS

Being situated in a high seismicity area, there is an imperious need of evaluating the seismic risk. The method of analysis presented here has the purpose of diminishing future damages occurred after a large earthquake and of evaluating the damage state. Limitations and incomplete existing seismic data make from the time history analysis a challenge. In the future, more data should be collected in order to be able to analyze properly the structures' situation in what concerns the seismic risk.

References

1. Zanardo, G., C. Pellegrino, C. Bobisut, C. Modena, Performance Evaluation of Short Span Reinforced Concrete Arch Bridges, *Journal of Bridge Engineering 9.5* (2004): 424-434.
2. *CSI Analysis Reference Manual*, Computers and Structures Inc, Berkeley, 2007.
3. Dusseau, R. A. and Wen, R. K., Seismic responses of deck-type arch bridges. *Earthquake Engineering & Structural Dynamics*, 1989.
4. *Cod de proiectare seismică*, Partea I – Prevederi de proiectare pentru cladiri, indicativ P100-1/2012.
5. Atanasiu, G. M., Ciutea, D., *A possible framework for Resilience of Iasi region*, ERA Net FP7 - Concert Japan, ROADERS Project, 2013.
6. Atanasiu, G.M., Bunea, G., *Seismic Hazard Characterization of Romania's North-Eastern Region*, ERA Net FP7 - Concert Japan, ROADERS Project, 2013.
7. http://www.seismosoft.com/en/Company.aspx

Numerical Investigations Regarding the Influence of Failure Criteria on Active Earth Pressure Calculation

Ștefan Cioară[1], Anghel Stanciu[1], Irina Lungu[1]
[1] *"Gheorghe Asachi" Technical University of Iași, Faculty of Civil Engineering and Building Services, prof.dr.doc. Dimitrie Mangeron str., 70050, Romania*

Summary

Along with the extensive use of numerical methods in geotechnical engineering it appears the necessity of selecting a failure model that should be capable to represent the shear strength for all stress paths likely to be encountered. In this respect, the geotechnical engineer can choose from a large variety of constitutive models described in the scientific literature. The best-known failure criterion is that of Mohr-Coulomb and its extensive use is a consequence of its simplicity, as well as due to the fact that most research presented in the literature incline to confirm it. Under the same plasticity criteria category (elastic-perfectly plastic), one can as well find the Drucker-Prager criterion, by means of which the influence of the intermediary stress, σ_2, on soil shear strength was developed. This paper presents a comparison of these two criteria with respect to the failure surface influence on shear strength and active earth pressure. Even though more advanced models are available, one should note that in the Haigh–Westergaard stress space all models are of conical, pyramidal or noncircular cone-shaped form. The comparative analysis of Mohr-Coulomb and Drucker-Prager models becomes, thus, of interest, whereas it can be easily extended to other models.

KEYWORDS: numerical methods, Mohr-Coulomb model, Drucker-Prager model, active earth pressure.

1. INTRODUCTION

The calculation of active earth pressures that a soil exerts on the face of a wall behind a retaining structure is one of the principal knowledge necessities for geotechnicians and the manner that this is resolved is directly reflected in the safety and the costs of this kind of construction. The correctitude of the solutions obtained is significantly influenced by the accepted design hypothesis. Considering that the soil is a material with a complex behavior, one must firstly examine the behavior of the retaining structure-massif ensemble in terms of stress state evolution in the

retained soil in order to enunciate correctly the active earth pressure calculation problem.

After the retaining structure execution, it is subjected to active earth pressures, under the action of which the structure fails either translational or rotational.

As the retaining wall moves up against its initial position, in the soil behind it takes place a mobilization of the angle of internal friction, wherewith the soil resists the motion tendency. This results in the diminution of the pressures that the soil exerts on the wall, and the rotation or translation movement stops when a balanced forces system is reached.

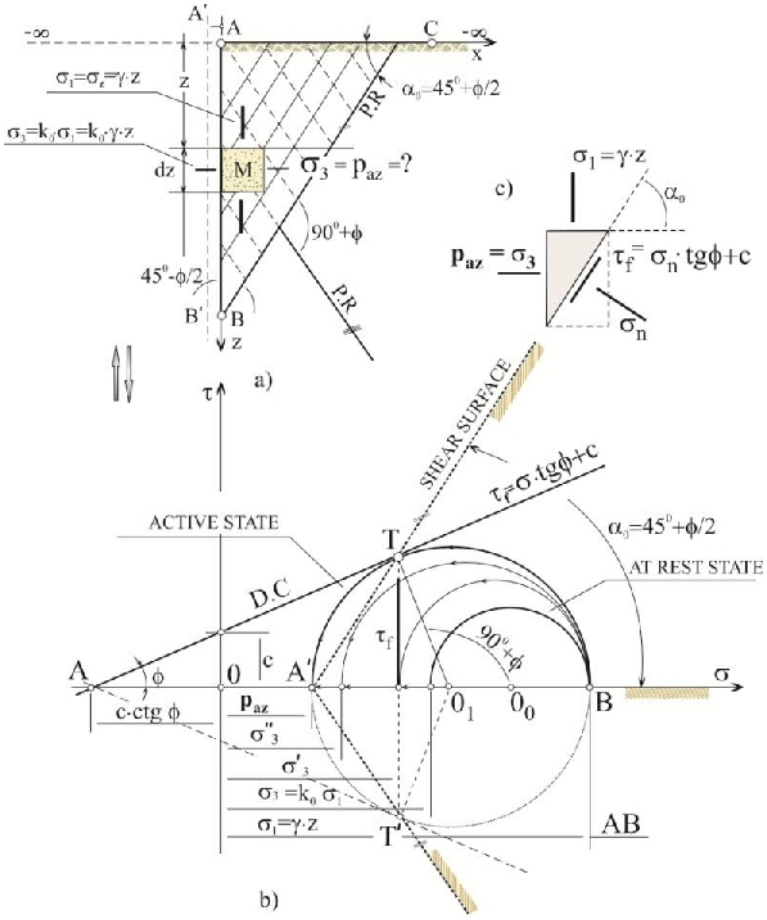

Figure 1. Active earth pressure determination using the Rankine method (Stanciu 2006)

The evolution analysis of stress states that appear in the soil, from resting position up to active state, can be made using the Mohr circles representation. Thereby, while σ1 remains constant, σ3 decreases and a succession of circles of a radius increasing up till the limit circle is obtained in the active state, as presented in Figure 1. It is thus considered that the soil failure appears in the moment that the stress circle becomes tangential to the intrinsic line and the failure surface will be inclined at an angle of $\alpha = 45-\varphi/2$ from the vertical.

It must be as well noted that the classical theories (Rankine, Coulomb) regarding earth pressures were developed on the basis of Coulomb theory and, implicitly, of Mohr-Coulomb failure criterion. Geotechnicians currently dispose of a multitude of plasticity criteria and, accordingly, are able to perform calculations regarding the earth pressures taking into account different Mohr-Coulomb criteria. The thus obtained values are usually evaluated in comparison with the classical methods (Coulomb or Rankine), the latter beneficiating of the advantage of their applicability and validation over time.

2. PLASTICITY CRITERIA

In the following the stress evolution will be analyzed with consideration to Mohr-Coulomb model in comparison to circumscribed and inscribed Drucker-Prager models; in all three cases plastic potential surfaces associated in a deviator plane are considered. The comparative analysis will be made on the basis of the principal stress ratio $Rf=\sigma1/\sigma3$ as well as considering the b parameter defined by Bishop (Bishop 1966):

$$b = \frac{\sigma_2 - \sigma_3}{\sigma_1 - \sigma_3} \tag{1}$$

that, besides its formerly defined significance (relative measure of σ2 stress in relation to σ1 and σ3), it can be interpreted as polar coordinate in the deviatoric principal stress space is directly connected to Lode angle (θ).

From all the main parameters that define elasto-plastic constitutive models (namely yield surface, plastic potential surface, hardening/softening laws etc.) the only one that determines the Rf ratio is the yield surface within its configuration and extent. It can be therefore affirmed that, in this respect, Mohr-Coulomb and Drucker-Prager criteria are representative regarding a series of other much more advanced models (Cap-Model, Hardening Soil etc.) that use yield surfaces similar to the ones presented in this paper.

2.1. Mohr-Coulomb (MC)

Mohr-Coulomb model was extensively used in the calculation of earth pressures on retaining structures. This is firstly due to its simplicity, in order to completely defining it only 5 parameters being necessary and for current geotechnical calculations it is considered that the precision offered by this criterion is suitable. The yield surface in the principal stress space is obtained by representing the 6 equations that define the meridians of the pyramid (Figure 2):

$$\begin{aligned}
F_1(\sigma,c) &= (\sigma_1-\sigma_3)+(\sigma_1+\sigma_3)\cdot\sin\varphi-2\cdot c\cdot\cos\varphi=0\\
F_2(\sigma,c) &= (\sigma_2-\sigma_3)+(\sigma_2+\sigma_3)\cdot\sin\varphi-2\cdot c\cdot\cos\varphi=0\\
F_3(\sigma,c) &= (\sigma_2-\sigma_1)+(\sigma_2+\sigma_1)\cdot\sin\varphi-2\cdot c\cdot\cos\varphi=0\\
F_4(\sigma,c) &= (\sigma_3-\sigma_1)+(\sigma_3+\sigma_1)\cdot\sin\varphi-2\cdot c\cdot\cos\varphi=0\\
F_5(\sigma,c) &= (\sigma_3-\sigma_2)+(\sigma_3+\sigma_2)\cdot\sin\varphi-2\cdot c\cdot\cos\varphi=0\\
F_6(\sigma,c) &= (\sigma_1-\sigma_2)+(\sigma_1+\sigma_2)\cdot\sin\varphi-2\cdot c\cdot\cos\varphi=0
\end{aligned} \tag{2}$$

The irregular shape of the envelopes, resulted from the representation of the previously presented equations in the principal stress space, is a consequence of the fact that within the pale of this model the influence of the intermediary stress σ2 on the soil shear strength is not taken into account (Wai Fah Chen,1988). Therefore, as far as that goes the surfaces of plastic potential associated in the deviatoric plane, numerical problems related to the establishment of the plastic deformations directions appear in the cases that the stress paths intersects one of the meridians formerly defined. Likewise, by not taking into account the intermediary stress σ2, the stress ratio Rf= σ1/σ3 remains constant on the entire yield surface and, regarding the cases that cohesion is null, it can be calculated using the following formula:

$$R_f = \tan^2(45+\phi/2) \tag{3}$$

where: φ = angle of internal friction;

As a result of triaxial tests, the fact that Mohr-Coulomb model approximates sufficiently the real yield surface of soils in the deviatoric plane (Goldsheider-1984, Wood-1981, Dihoru-2005) is confirmed (Figure 2.b).

It is ascertained, however, that σ2 has an influence on soil failure, especially in the area close to the meridian of triaxial extension (θ=-30°). As a result, considering that currently the shear strength is determined after performing triaxial tests of axial symmetrical stress state corresponding to the triaxial compression meridian (θ=30°), one can state that Mohr-Coulomb model underestimates the shear strength of the soils not in axial symmetrical stress and deformation state.

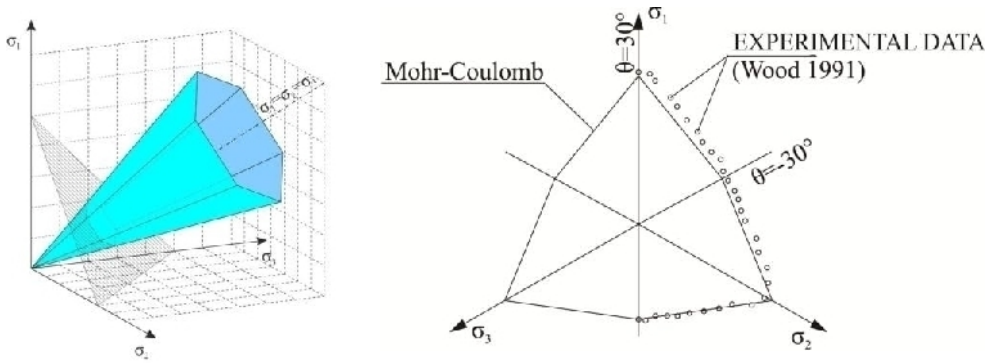

a) General representation b) View in deviatoric plane

Figure 2. Mohr-Coulomb criterion representation

2.2. Drucker-Prager (DP)

Through Drucker-Prager model is tried the consideration of the intermediary stress σ2 influence on the shear strength of soils and, for that purpose, the equation of the failure surface is formulated in the stress state invariants, as following:

$$\sqrt{J_{2D\sigma}} = A + B \cdot I_{1\sigma} \tag{4}$$

where : J2Dσ – the second invariant of the deviatoric tensor;

I1σ – the first invariant of the tensile tensor;

A,B – material constants.

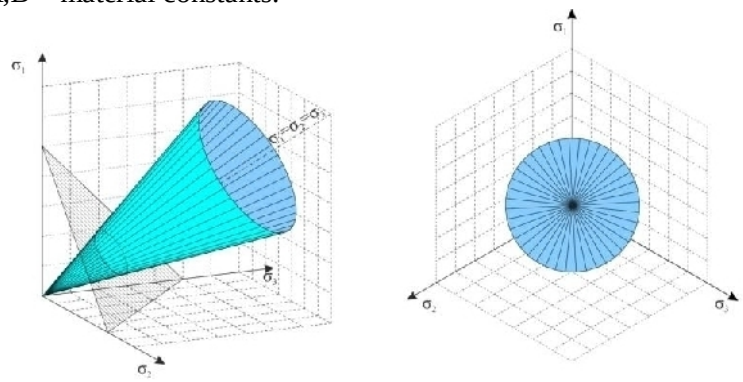

a) General view b) View in deviatoric plane

Figure 3. Drucker-Prager cristerion representation

In the principal stress space this equation represents a cone that can be connected to the Mohr-Coulomb pyramid in more than one variant (Figure 4). Thus, if is supposed that Drucker-Prager envelope is circumscribed to the Mohr-Coulomb

one, then the expressions for the material constants A and B are the following (Hua Jiang, 2011):

$$A = -\frac{6 \cdot \sin\varphi}{(3-\sin\varphi)\cdot\sqrt{3}} \qquad B = \frac{6 \cdot c \cdot \cos\varphi}{(3-\sin\varphi)\cdot\sqrt{3}} \tag{5}$$

If one assumes that the Drucker-Prager envelope inscribes in the Mohr-Coulomb one, then these expressions are (Hua Jiang, 2011):

$$A = -\frac{6 \cdot \sin\varphi}{(3+\sin\varphi)\cdot\sqrt{3}} \qquad B = \frac{6 \cdot c \cdot \cos\varphi}{(3+\sin\varphi)\cdot\sqrt{3}} \tag{6}$$

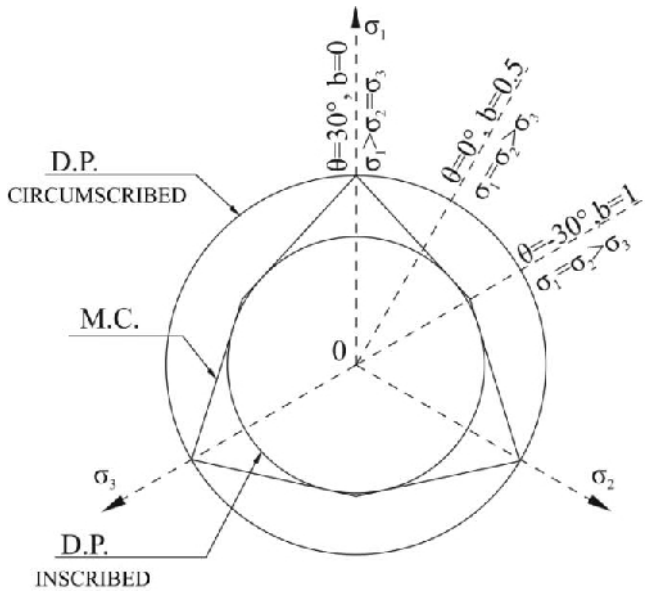

Figure 4. Connexion variants of the Drucker-Prager cone to the Mohr-Coulomb pyramid

Through the circular shape of the yield surface, the problems related to numerical difficulties are resolved as far as that goes for establishing the directions of the plastic deformations. There appear, however, a series of problems reported in literature that limits the use of this failure criterion. Between these, the most notable is demonstrated by Bishop who shows that, for the circumscribed cone, the limit value of the angle of friction is 36.8° (Bishop 1968). At this value, the Drucker-Prager surface is tangent to the σ1 O σ2 plane and, consequently, there exists a meridian for which σ3 is null. For this meridian, the Rf stress ratio and, implicitly, the shear strength tend to infinity.

3. NUMERICAL RESULTS

3.1. Calculation models

The numerical calculations that will be presented in the following were performed by the instrumentality of Flac 2D program that uses the finite differences method. The geometry and static scheme of the analyzed problem are presented in Figure 5. The massif dimensions were imposed in such way that the contour conditions may not influence the studied portion.

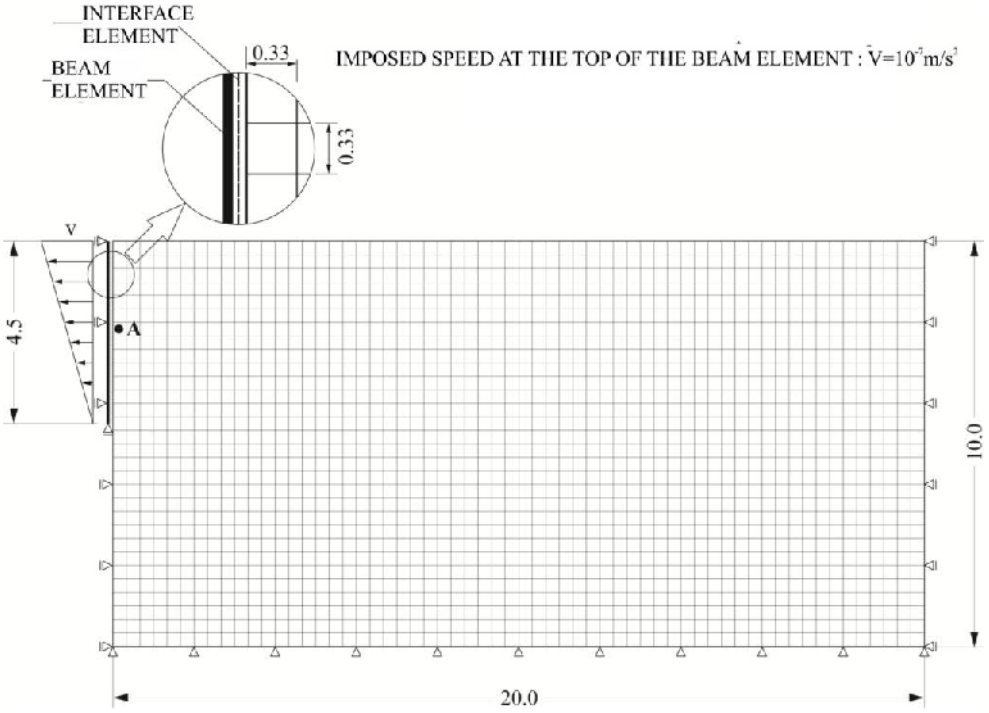

Figure 5. The static scheme considered for numerical simulation

The support was modeled using a "beam" element located on the lateral façade of the massif, as shown in Figure 5. Between the support and the massif an interface element has been disposed so that between the two shapes friction will not be developed but only normal compression stresses. The displacement of the support was simulated by imposing a rotational velocity around its inferior point.

For the elastic behavior of the soil an E=35000kPa was used, the Poisson's ratio being established on the basis of the following formula, derived from Jacky's formula:

$$\nu = \frac{1-\sin\varphi}{2-\sin\varphi}, \; pentru\; \varphi = 33^{\circ} \Rightarrow \nu = 0.31289 \tag{7}$$

By imposing the Poisson's ratio in this manner, the value of at-rest earth pressure is ensured according to the earth pressure calculated using Jacky's formula.

The soil behavior in the plastic range was simulated using the following plasticity criteria: Mohr-Coulomb, circumscribed Drucker-Prager, inscribed Drucker-Prager; the numerical values for the parameters of the models used are presented in Table 1.

Table 1. Numerical values for the parameters of the model used in numerical calculations

Model	E(kPa)	ν	φ(°)	c(kPa)	ψ(°)
M.C.	35000	0.31289	33	0	0
	E(kPa)	ν	A	B	ψ(°)
D.P.-inscribed	35000	0.31289	0.532	0	0
D.P.-circumscribed	35000	0.31289	0.768	0	0

3.2. The principal stresses evolution regarding the A point

The principal stresses evolution, regarding the A point indicated in Figure 5, during the failure of the retaining structure, is represented for each considered criterion in Figures 6, 7 and 8.

Initially, under the action of own weight, the entire simulated earth massif is in the elastic range because none of these hypotheses, in K0 ($\sigma 2=\sigma 3\neq 0, \varepsilon 2=\varepsilon 3=0$) load conditions, the stress path does not reach the yield surface. During this stage, the at-rest earth pressure is the same for every one of the three modeling hypotheses due to the fact that the values of σ2 and σ3 stresses values in this situation are determined by Poisson's ratio.

Once the displacement of the support is initiated, regarding the calculus effectuated in Mohr-Coulomb hypothesis, the of σ2 and σ3 stresses decrease until the moment they reach the plastic failure surface, remaining constant afterwards, while in the case of Drucker-Prager cones it is observed that after reaching the plastic failure surface, the values of the stresses do not remain constant. This difference between the two criteria is due to the laws of the principal stress space plastic potential forms.

On account of the Mohr-Coulomb criterion, the plastic potential law is rectilinear in the deviatoric plane and the plastic deformations vector will have a constant direction during the simulation; the projections after the three coordinate's axes will implicitly present constant ratios.

With respect to the Drucker-Prager model, the plastic potential law is circular in the deviatoric plane and, consequently, the plastic deformations vector tends to "slide" to an equilibrium position.

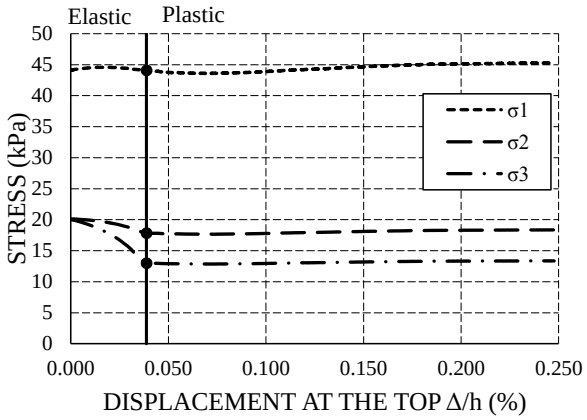

Figure 6. The evolution of point A stresses in Mohr-Coulomb hypothesis

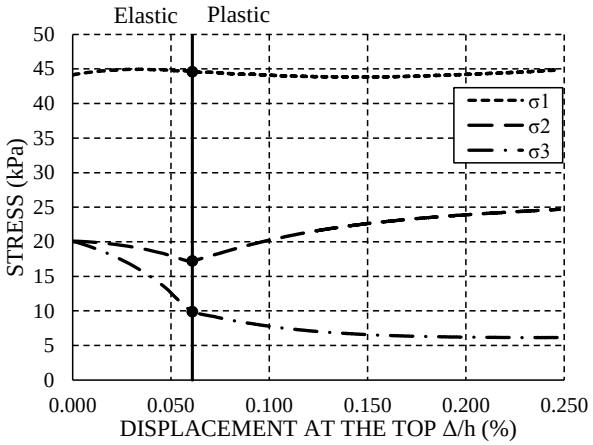

Figure 7. The evolution of point A stresses in circumscribed Drucker-Prager hypothesis

As regards the transition moment from elastic range to plastic one, one can observe that the three hypotheses are ordered by the size of the yield surface in the deviatoric plane. The relative displacements values at the top of the support in order to produce this transition are presented in Table 2.

The shear strength evolution, expressed by Rf ratio, for the A point in the massif, is graphically represented in Figure 9. It is once again noticed that the results of the three hypotheses are ordinate by the size of the yield surface in the deviatoric plane. The maximum value (7.317) appears, thus, in the case of the Drucker-Prager cone utilization, while the minimum value (3.258) appears in the case of the inscribed Drucker-Prager cone. At the same time, regarding the Mohr-Coulomb criterion, the maximum Rf value is of 3.392 and remains constant during the

simulation in the plastic range. Hereinafter, replacing the values obtained for the Rf in the 3rd formula, one can estimate the Mohr-Coulomb equivalent angle of friction (φ_{mc}).

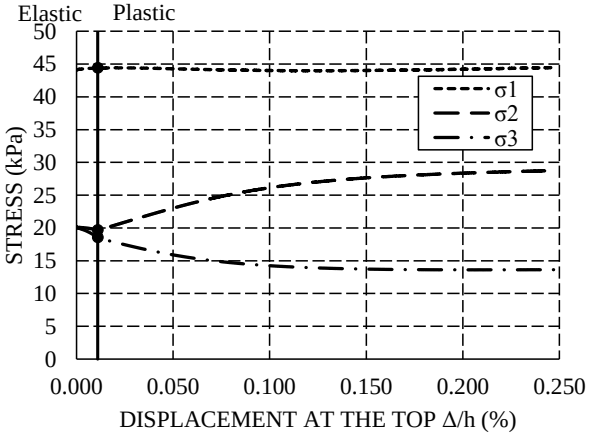

Figure 8. The evolution of point A stresses in inscribed Drucker-Prager hypothesis

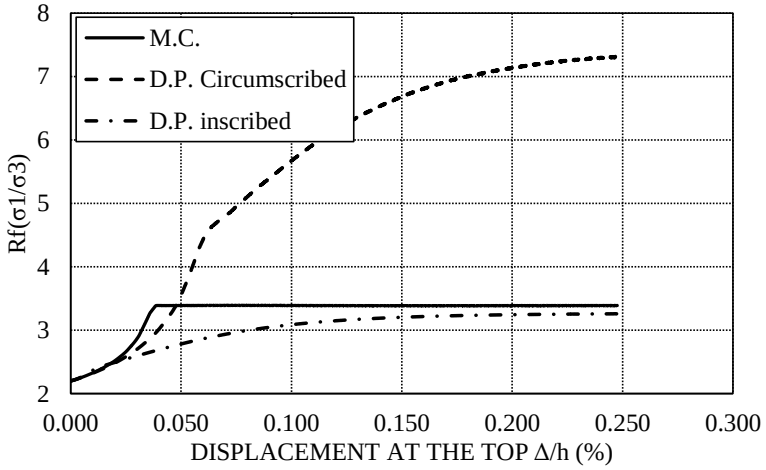

Figure 9. The evolution of R_f ratio in all the three considered hypotheses

Following the variation of the b parameter (Figure 9) one can observe that the two Drucker-Prager criteria fundamentally behave in the same manner, the differences between the calculated stresses being caused, in fact, by the size of the yield surfaces and, implicitly, by the moment when the stress path reaches the failure surface. To note is that in both situations, as the angle of internal friction (φ) is mobilized, the b parameter evolutes from its initial null value to 0.5 which, in the principal stress space, coincides with the pure shear plane (θ=0). Regarding the Mohr-Coulomb failure criteria, the value of the b parameter remains unchanged in the plastic range.

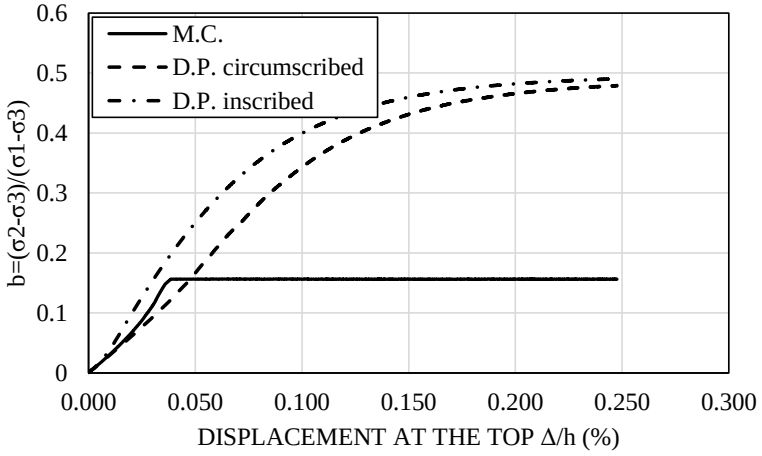

Figure 10. The evolution of *b* parameter in all the three considered hypotheses

In Table 2 the previously presented data is synthesized regarding the values of the relative displacements at the top of the support for which the soil in point A passes from the elastic to the plastic range, as well as the values of the b parameter, of the Rf ratio and of the equivalent angle of friction (φmc) in the moment of plastic deformations initiation and the end of the simulation.

Table 2. Numerical values that characterize the estimated stress states by the used models

Plasticity criteria	Initial (passing to plastic range)				Final (end of simulation)		
	Δ/h(%)	b	R_f	φ_{mc}	b	R_f	φ_{mc}
DP inscribed	0.011	0.045	2.395	24.261	0.490	3.258	32.025
MC	0.039	0.156	3.392	33.000	0.156	3.392	33.000
DP circumscribed	0.061	0.212	4.504	40.005	0.479	7.317	49.423

3.5. Active earth pressures

The most important aspect of numerical simulation for the geotechnicians is the earth pressures calculation. From this point of view, by examining the diagrams presented in Figure 11, one can observe that all the three calculation models approximate very well the at-rest earth pressure as a consequence of imposing the Poisson's ratio after Jacky's formula.

Immediately after the beginning of the retaining wall rotation, the Mohr-Coulomb criterion predicts an earth pressure approximately identical to the active earth pressure calculated by the aid of Rankine's formula; at the same time, the

circumscribed Drucker-Prager criterion surpasses in the superior half the active earth pressure line, after Rankine, as a consequence of partial plasticization (only in the superior half) of the soil behind the retaining wall. In the following, the next positions of the active earth pressures diagram highly underestimate the earth pressure if it is to consider Rankine's theory as reference.

As far as that goes for the inscribed Drucker-Prager criterion, a natural gradual transfer from the at-rest state to the active earth pressure is observed.

Comparing the results of the three models at different moments during the simulation, it can be noticed that as the rotation of the support is produces, the earth pressures predicted by Mohr-Coulomb are in accordance with the inscribed Drucker-Prager. This is a natural consequence of the fact that in Drucker-Prager hypothesis the stress paths of the points in the massif tend to $\theta = 0$ (close to the tangency area between the two criteria), the Rf ratios thus equalize.

If it is to consider the circumscribed Drucker-Prager criterion, the curved allure of the earth pressures diagram is observed, consequence of the gradual plasticization of the massif behind the retaining structure.

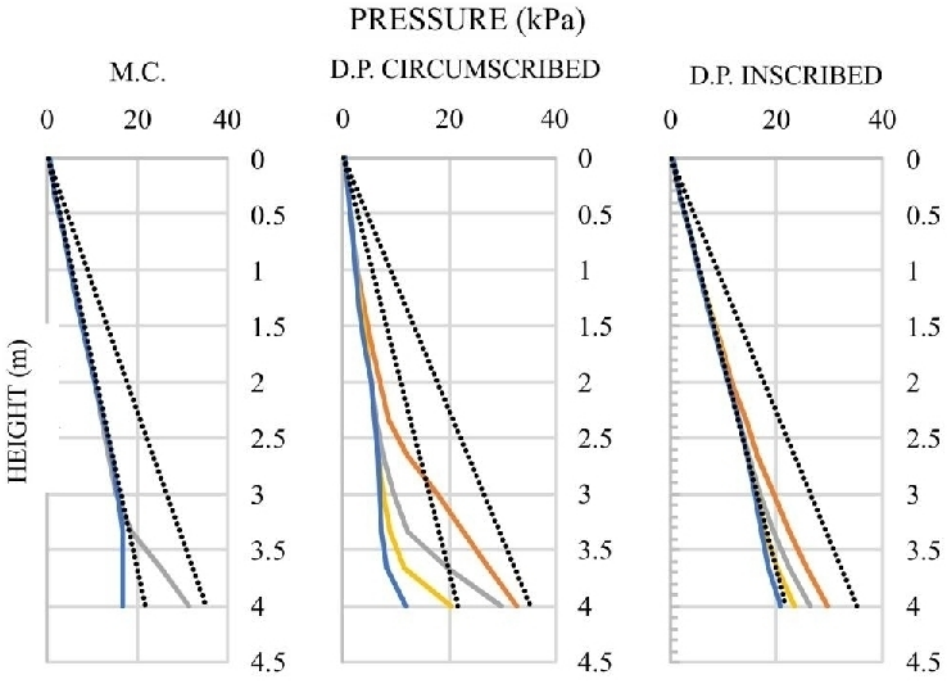

Figure 11. The evolution of the earth pressures in the three considered hypotheses

The diagrams representing the earth pressures resultant were obtained by summing up the horizontal reactions of the retaining structure. It is evident how at the

beginning of the failure of the retaining structure the forces are identical, but once the rotation develops the three graphs separate and for a 4 mm displacement at the top of the structure the circumscribed Drucker-Prager criterion overpasses the calculated active earth pressure value. With respect to Mohr-Coulomb criterion, a descendent trend until a 7 mm displacement is observed, followed by a plateau region that corresponds to the value of the active pressure calculated after Rankine. The inscribed Drucker-Prager criterion predicts the highest earth pressure but it can be also observed that along with the simulation deployment this one tends to reach the same value as in the case of Mohr-Coulomb criterion.

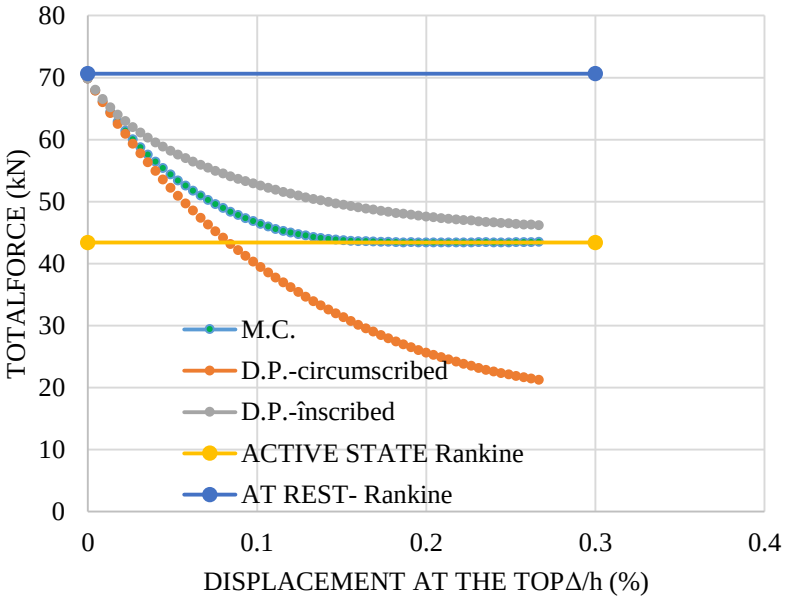

Figure 12. The evolution of the total forces in the three considered hypotheses

4. CONCLUSIONS

The results presented in this paper show that the three considered criteria estimate different values regarding the evolution of the σ2 and σ3 stresses when in the case of the enounced problem; this fact is a natural consequence of the differences between the yield surfaces formulas. It is principally observed that the two Drucker-Prager criterion variants behave in the same manner, the differences being caused by the size of the yield surfaces in the deviatoric plane.

With respect to the calculated active earth pressures, one can conclude that both Mohr-Coulomb and inscribed Drucker-Prager criteria estimate values close to the ones manually calculated using Rakine's theory. At the same time, the

circumscribed Drucker-Prager criterion highly underestimates the value of the active earth pressure if it is to compare with Rankine's theory.

References

1. Bishop, A.W. *The strength of soils as engineering material* -Sixth Rankine Lecture,1966.
2. Chen, Wai Fah, Han, D.J. *Plasticity for Structural Engineers*-1988.
3. Dihoru, L. , Wood, D.M., Sadek, T., Lings, M. A neural network for error prediction in a true triaxial apparatus with flexible boundaries, *Computers and Geotechnics Volume 32*, Issue 2, 59-71, 2005.
4. Goldscheider, M. *True triaxial tests on dense sand-Constitutive relations for soils*. Workshop results, Grenoble, Pages 11-54, 1984.
5. Griffiths, D.V., Failure Criteria Interpretation Based on Mohr-Coulomb Friction, *Journal of Geotechnical Engineering*, 116(6), pp. 986–999, 1990.
6. Hua Jiang, Yongli Xie, A note on the Mohr–Coulomb and Drucker–Prager strength criteria, *Mechanics Research Communications*, 38 (2011) pp. 309–314.
7. Stanciu A., Lungu I., *Fundații*, Vol.1, Editura Tehnică, 2006.
8. Wood, D.M., True triaxial tests on boston blue clay, *International Conference on Soil Mechanics and Foundation Engineering*, Vol. 1, 825-830, 1981.

Green roof performance simulation using WUFI software

Adriana L. Kadhim-Abid[1] and Gabriela M. Atanasiu[2]
[1] *PhD Student, Faculty of Civil Engineering and Building Services, "Gheorghe Asachi" Technical University, Iaşi,700050, Romania*
[2] *Faculty of Civil Engineering and Building Services, "Gheorghe Asachi" Technical University, Iaşi,700050, Romania*

Summary

Urban settlements around the globe deal with issues regarding energy consumption and energy costs for heating and cooling. For the building sector one of the sustainable measures which targets energy saving potential is represented by green roof systems. In order to sustain the feasibility of green roof solutions, a series of numerical simulations are conducted for assessing the energy saving potential and investigate any problems that may occur in real operating conditions.

The study makes use of an energy balance equation used to create a numerical model for green roof systems. The simulation are conducted in WUFI software using interior and exterior climatic parameters according to local climate conditions. This analysis presents the methodology of the study for a roof structure with a vegetative cover, later used for WUFI simulation.

In order to better frame the methodology specific for this type of analysis, the authors present some suggestive results, previously obtained from simulations of an existing roof terrace of a building located in the city of Iassy, under specific climate conditions.

KEYWORDS: green roof performance, numerical simulation, WUFI.

1. INTRODUCTION

Climate changes determined by the massive presence in the atmosphere of greenhouse gases, deforestation, changing water courses and other anthropogenic activities with detrimental impact on the environment have become a certainty, as the fact that the process cannot be stopped on short or medium term. In regards to the relationship between buildings and climate change it can be stated that this is complex and several aspects must be considered such as the fact that buildings are responsible with emissions of greenhouse gases for about 40% at European level [1] and the impact of climate change on buildings manifests by increased air

temperature during warm seasons. Increased air temperature within cities contribute to the intensification of the Urban Heat Island phenomenon. In this context, the attitude of building design responsible as that of construction industry towards climate change is most important and concerns regarding mitigation-adaptation strategies become priority. Mitigation targets to limit and diminish causes of climate change while adaptation aims to lessen the aggressive impact of climate through a series of actions and specific measures [2]. One of the measures, regarding the building sector, is represented by the green system solutions such as green roofs. These type of solutions are suitable for both renovation/rehabilitation phase as well as for new constructions.

In order to demonstrate that green roof systems represent a viable mitigation/adaptation solution achieving both optimal indoor comfort conditions and diminish the Urban Heat Island effect, several analysis have been conducted in order to estimate their performance. These analysis follow a study for energy saving assessment used in cooling and heating as well as identifying problems that may occur in real operating conditions. Main objectives of this study include the identification of the Urban Heat Island phenomena in the city of Iassy, Romania, monitoring local meteorological conditions for both warm and cold seasons, and implement a green roof system on the terrace of a building located on the premises of the Faculty of Civil Engineering and Building Services of Iassy, Figure 1.

Figure 1. Building used for analysis

2. MATERIALS AND METHODS

Numerical simulation for green roof performance were conducted using WUFI® software [3], a program which allows realistic calculations of the transient coupled one and two dimensional heat and moisture transport in multi layer building

components exposed to natural climatic conditions. Simulations complied with the existing situation of the roof terrace and two improved scenarios, Scenario 1 with a green roof system and Scenario 2 with a green roof systems provided with an additional 15 cm insulation layer, according to Figure 2 and Figure 3, respectively.

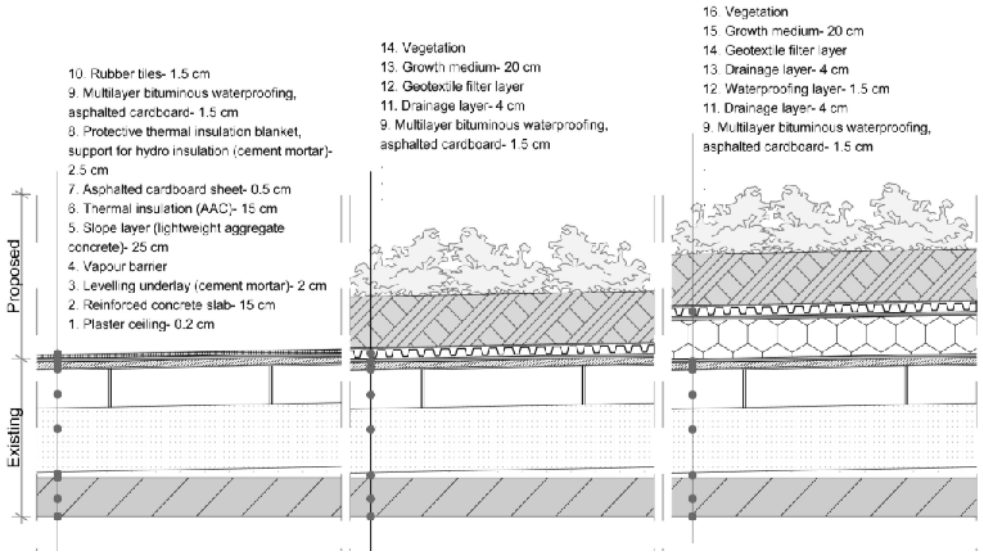

Figure 2 .Scenarios considered for numerical simulation: initial situation (left), scenario 1 (center), scenario 2 (right)

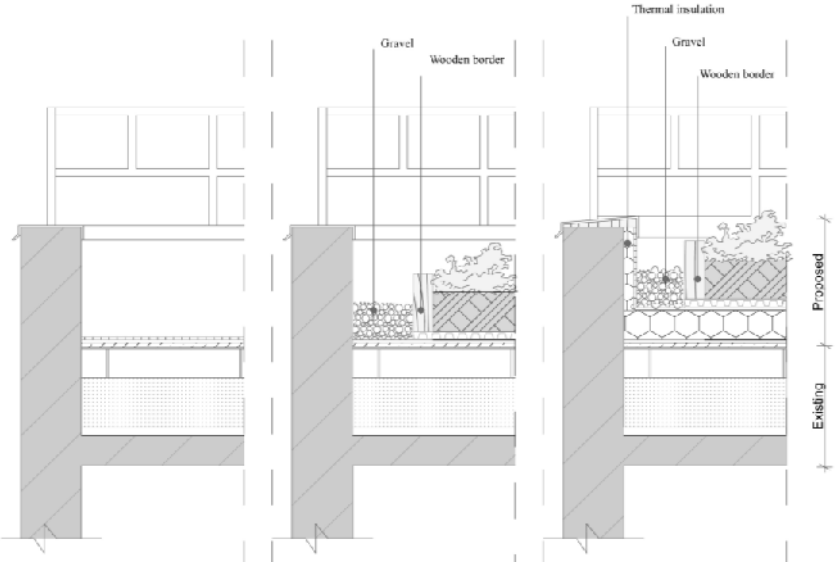

Figure 3. Terrace parapet detail: initial situation (left), scenario 1 (center), scenario 2 (right)

The simulations were performed using WUFI®, version 2.1.1.73, for unidirectional thermal field under variable conditions using real climate data for 2013. Some of the data was obtained courtesy of the Faculty of Geography and Geology of Iaşi and some from direct observations or data from literature. In the scenarios analyzed with WUFI® 2D, for indoor climate conditions, constant values were considered: temperature of 20°C and humidity of 55%. For the outdoor conditions, registered data for 2013 in Iaşi was confronted with the typical climate previously defined for this city [4], comprising values for air temperature, relative humidity, solar global and diffuse radiation, normal rain, wind direction and speed, and air pressure. Complementary to the material hydrothermal characteristics, these are presented in Table 1, and for the roof terrace considered surface coefficients are presented in Table 2.

Table 1. Hydrothermal characteristics of materials

Material	Bulk density [kg/m^3]	Porosity [m^3/m^3]	Specific heat capacity [J/kg·K]	Thermal conductiv. [W/m·K]	Water vapour diffusion resistance factor [-]
Interior plaster	1700	0.49	840	0.87	8.5
Reinforced concrete	2500	0.18	840	1.74	21.3
Cement mortar	1800	0.24	840	0.93	8.5
Vapour barrier	130	0.001	2300	2.3	150000
Light aggreg. concrete	1800	0.2	840	0.93	8.5
AAC insulation	725	0.72	870	0.3	3.9
Asphalted cardboard	600	0.001	1460	0.17	1500
Extruded polystyrene	40	0.95	1500	0.04	100
Drainage air layer	1.3	0.999	1000	0.23	0.38
Soil growth medium	1200	0.41	840	0.8	3.0

Table 2. Surface coefficients

Surface	Heat transfer coefficient [W/m^{2}K]	Short-wave radiation absorptivity [-]	Long-wave radiation emissivity [-]
Interior surface	8	-	-
Exterior surface – initial state	24	0.88	0.9
Exterior surface – improved state	12	0.86	0.9

3. RESULTS AND DISSCUSIONS

From the simulations performed using WUFI® data was obtained regarding information on temperature and humidity regime for the established boundary conditions, layer limits and in any section along their thickness. The program provided data on diurnal temperature regime of outer and inner surface of the terrace, and also specific values for relative humidity in the roof structure for the considered scenarios.

Results obtained highlight the following aspects:

- the presence of vegetation influences the difference between the maximum and minimum temperature by changing the outer surface albedo [5];
- the additional insulation layer is the factor that significantly interferes with the heat flow value which further on determines overheating and over usage of the air condition. Thus, the heat flow is reduced by 15% as shown in Figure 4 [5];
- the humidity level of the soil influence the moisture value of the inward heat flow by increasing the thermal conductivity of the soil and thus reducing the thermal resistance. This is more obvious for cases when the vegetative layer is present and there is no additional insulation layer present [5];

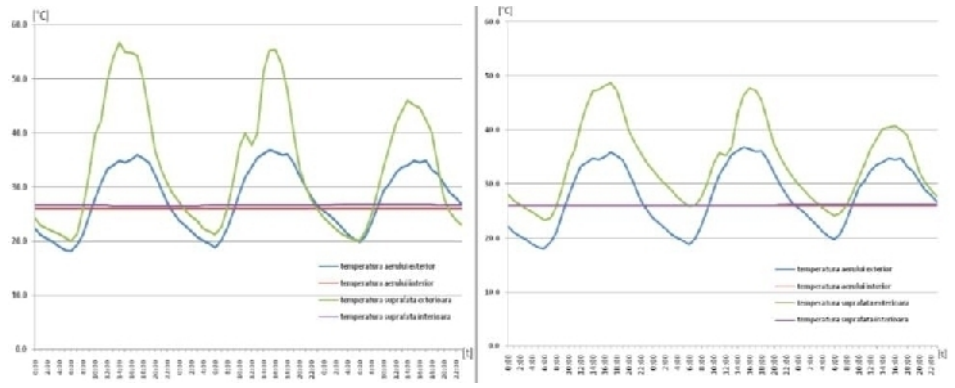

Figure 4. Influence of the vegetative and insulation layers: scenario 1 (left), scenario 2 (right)

Regarding condensation and moisture levels, simulation using WUFI® reveal considerable information concerning values of relative humidity in the roof structure for all scenarios. Specific values for relative humidity as obtained from the program are presented in Figure 5 for the initial situation and respectively, Figure 6 for Scenario 2.

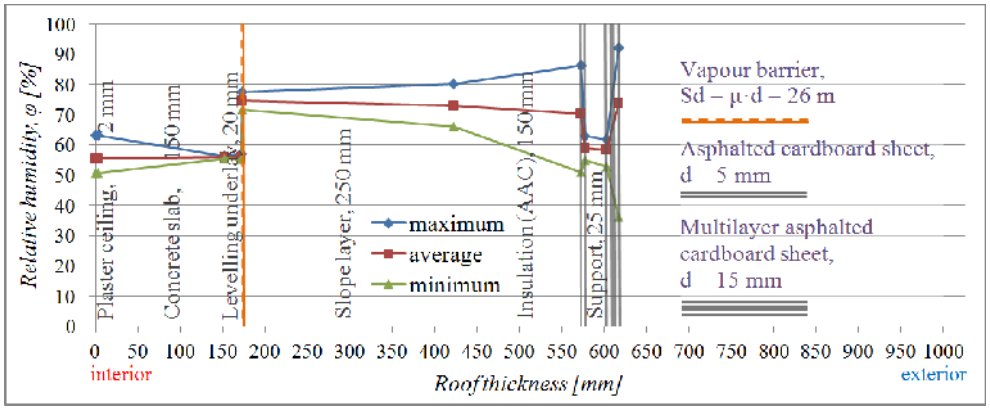

Figure 5. Specific values for relative humidity in roof structure for the initial situation

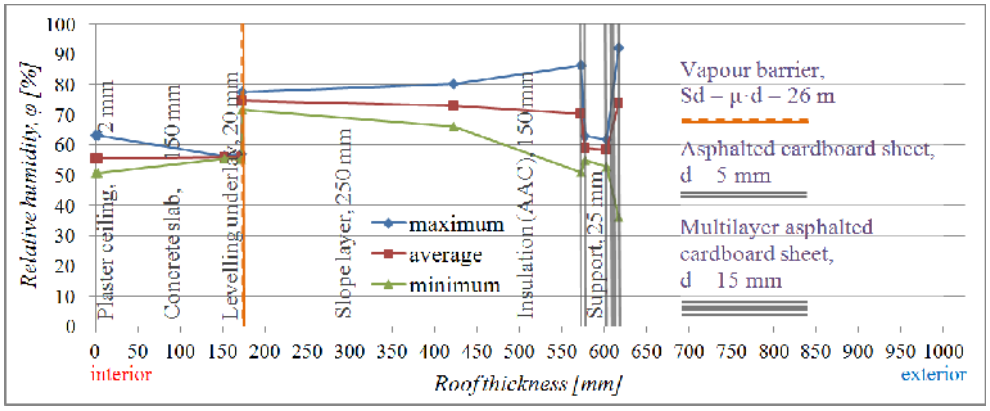

Figure 6. Specific values for relative humidity in roof structure for Scenario 2

As mentioned before, the software provides data regarding humidity variations within the layers. Therefore, comparing humidity levels in the AAC insulation layer (Aerated Autoclaved Concrete) for the initial situation and the improved scenario reveal some improvement regarding the annual and daily amplitude of the humidity variations for the latter, according to Figure 7. Similarly, results are presented for the hydroinsulation support layer in Figure 8, also obtained using WUFI®.

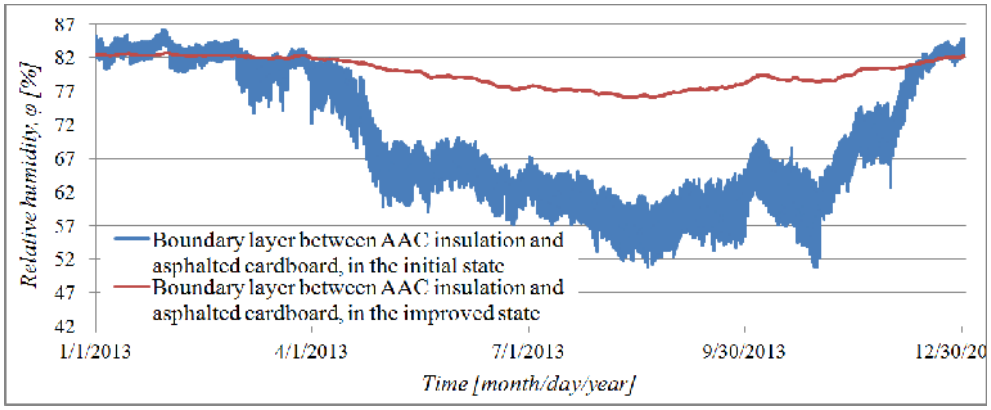

Figure 7. Annual relative humidity in the external boundary layer of AAC insulation

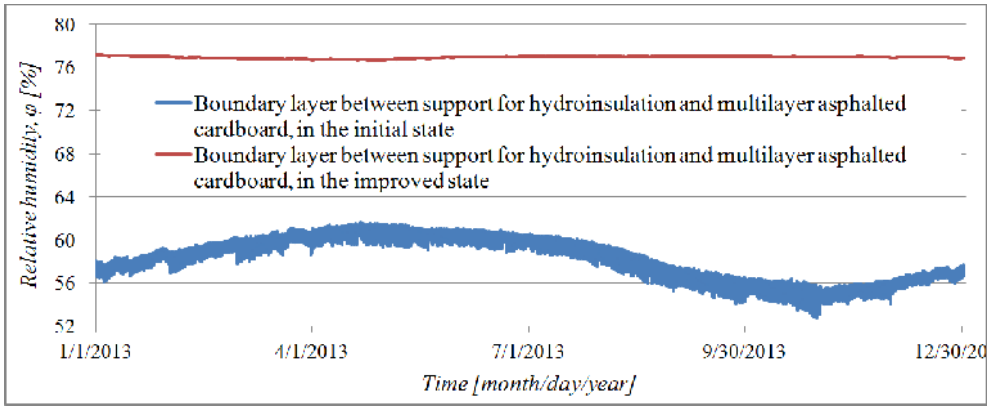

Figure 8. Annual relative humidity in the external boundary layer of hydro insulation support

4. CONCLUSIONS

Results of the research conducted to the present within the numerical simulation regarding green roof system performance lead to the conclusion that these type of solution contribute to mitigating towards the negative effects of the Urban Heat Island phenomena, while also minimizing the heat flux entering the building by changing albedo values of conventional roofs with those characteristic to vegetation.

WUFI® program, as presented above, is a suitable software for green roof performance assessment, capable of delivering information regarding numerical simulation methods taking into account the heat transfer coupled with mass transfer while using specific climate conditions. Also to be mentioned is the fact that WUFI® software used for numerical simulations in this analysis considers only the albedo values which partially modifies the inward heat flux. Actual behavior caused by other components of the energy balance such as evapotranspiration, photosynthesis, latent heat of evaporation and other factors, can only be assessed by observations and measurements in an experimental-model scale, which in essence is the objective of the next stage of research.

References

1. European Commission, *Council Directive 93/76/EEC of 13 September 1993 to limit carbon dioxide emissions by improving energy efficiency* (SAVE), 1993.
2. Fussel, H.M., Klein, R.J.T., *Adaptation to climate change in the context of Sustainable Development, Climate Change and Sustainable Development: A Workshop to Strengthen Research and Understanding*, United Nations Department of Economics and Social Affairs, The Energy and Resources Institute (TERI), New Delhi, April 7-8, 2002.
3. WUFI® Software, version 2.1.1.73, www.wufi.de.
4. Erhan, E., *Clima și microclimatele din zona orașului Iași*, Editura Junimea, Iași, 1979.
5. Kadhim-Abid, A.L., Atanasiu, G.M., Bliuc, I., Diminuarea efectelor Insulei de Căldură în aglomerările urbane utilizând soluții specifice clădirilor verzi, *Proc.: Products and Technologies for Sustainable Development, The VIIIth Edition of the Annual Conference "The academic days of the Academy of Technical Sciences in Romania"*, Brașov 4-5 Octombrie, Editura AGIR, pag. 281-290, 2013.

GRAITEC ADVANCED DESIGN Capacity Design

Adrian Gleja[1],
[1]*Structural Engineer, Graitec Romania, Bucureşti, Romania, www.graitec.ro*

Summary

ADVANCE Design, part of the BIM GRAITEC ADVANCE suite, is dedicated to structural engineers who require a comprehensive solution for simulating and optimizing all their projects. The uniqueness of GRAITEC Advance is to offer a solution that is very efficient because it is dedicated to building professionals: design, calculation and creation of fabrication drawings, easy training, and provides a rapid return on investment, usually from the first project.

ADVANCE Design goes further than ever in helping engineers to optimize the design of concrete, steel and timber structures according to the Eurocodes and Romanian codes. Some of the many new functionalities in regards to Eurocodes are: climatic generator improvements according to latest norms CR 1-1-3/2012 and CR 1-1-4/2012, automatic load combinations according to CR 0-2012, punching verification according to Eurocode 2, checking the overall stability of circular sections of Class 4 according to Eurocode 3, and capacity design according to P100-2013 or Eurocode 8.

KEYWORDS: structural analysis, structural design, reinforced concrete, capacity design.

1. INTRODUCTION

Seismic design of structures is mainly focused on developing a favorable plastic mechanism to render the structure strength, ductility, and stability.

The behavior of a structure regarding the action of a major earthquake is anything but ductile, taking into account the oscillating nature of the seismic action and the fact that plastic hinges appear rather randomly. To achieve the requirements of ductility, structural elements, and thus the entire structural system must be able to dissipate the energy induced by the seismic action, without substantial reduction of resistance.

Both Romanian seismic design code P100-1/2013 and Romanian standard SR EN 1998-1, provide a method for prioritizing structural resilience ("capacity design method") in order to better choose the necessary mechanism for dissipation ofenergy. Determination of the design efforts and the efforts for elements will be in accordance to the rules of this method.

2. CONSTRUCTIVE MEASURES FOR MEETING THE LOCAL AND GLOBAL DUCTILITY

Most of the engineering problems in vibrations are leading to the eigenvalue problem, in the simple or generalized format. It is commonly accepted and convenient to use the real eigenvalues; therefore the matrices of the dynamic system are symmetric and positive defined. In the case of the time history analysis the equations of motion are decoupled, based on the assumption that the damping is proportional (Rayleigh type) to the mass or stiffness or both. The damping matrix C is then written as a linear combination of M and K ($C = \alpha M + \beta K$). Under these circumstances the time responses obtained separately can be superimposed using the modal participations.

Depending on the capacity of energy dissipation, structures are classified into the following classes:

- medium ductility (M),
- high ductility (H).

In order to design in one of the two classes of ductility, the values of the behavior factor "q" must be first elected. For structures made of reinforced concrete, the behavior factor is limited to the values in Table 2.1, both for P100-1/2013 and for SR EN 1998-1-1.

Table 1. Values of behavior factor "q" for regular structures in elevation
(Table 5.1 from P100-1/2013 and SR EN 1998-1-1)

Type of structure	q	
	Class of ductility H	Class of ductility M
Frames, dual system, connected walls	5αu/ α1	3.5 αu/α1
Walls	4 αu/α1	3.0
Core (flexible to torsion)	3.0	2.0
Inverted pendulum structures	3.0	2.0

A favorable plastic mechanism requires a structure of the sections so that the plastic deformations first occur at the end of the beams and later at the base of the column. Also, the nodes between beams and columns must remain in the elastic range of stress.

In order to achieve this, code P100-1/2013 and SR EN 1998-1-1, must be correlated with the design requirements form SR EN 1992-1-1.

The local ductility requirements provide a minimum area of reinforcement for longitudinal reinforcement, both for beams and for columns. Thus, SR EN 1992-1-1 recommends a minimum area of longitudinal reinforcement for columns, As,min, according to chapter 9.5.2 (2):

$$A_{s,min} = \frac{0.1 \cdot N_{Ed}}{f_{yd}} \quad (1)$$

$$A_{s,min} \geq 0.002 A_c \quad (2)$$

Where:

fyd – calculation of yield strength for reinforced concrete; NEd – the value of axial force (maximum axial force in columns)Ac – the concrete cross-section area.

Another condition for the local ductility of columns refers to the normalized values of the axial force – νd. Table 2 lists its limit values.

Table 2. Limit values for νd according to ductility class and standard

Ductility class	P100/2013	EN 1998-1
M	0.55	0.65
H	0.4 ÷0.65	0.55

Similarly, in order to meet the requirements of the local ductility for beams, chapter 5.4.3.1.2 (5) from SR EN 1998-1-1 and chapter 5.3.4.1.2 (4) from P100-1/2013, recommend using a minimum percentage of longitudinal reinforcement for wide areas:

$$\rho_{min} = 0.5 \cdot \frac{f_{ctm}}{f_{yk}} \tag{3}$$

Where:

fyk – characteristic yield point of reinforcements; $f_{ctm} = 0.3 \cdot f_{ck}{}^{2/3}$ [MPa] when the concrete strength class is ≤ C50/60 $f_{ctm} = 2.12 \cdot \ln\left(1 + \frac{f_{cm}}{10}\right)$ [MPa] when the concrete strength class is > C50/60 $f_{cm} = f_{ck} + 8$ [MPa]

Design values of bending moments in beams are determined by the formula (5.3) from P100-1/2013 and (5.8) from SR EN 1998-1-1:

$$M_{d,b,i} and M_{d,b,j} = \gamma_{Rd} \cdot M_{R,b,i/j} \cdot min\left(1, \frac{\sum M_{R,c}}{\sum M_{R,b}}\right) \tag{4}$$

Where:

M(R,b,i/j) - the value of the moment at the end of "i" or "j" of the beam, for the sense of the seismic bending moment; M(d,b,i/j) - the value of the design bending moment for determining the associated shear forces; YRd - over strength factor (Table 3) which takes into account steel strain-hardening of the longitudinal steel and shrinkage of concrete; ∑M(R,c) - the sum of the design valuesof the capable moments of the columns in the nodes;∑M(R,b) - the sum of the design values of the capable moments of the beams in the node.

Table 3. Limit values for ϒRd for beams according to ductility class and standard

	ϒRd	
Ductility class	P100-1/2013	EN 1998-1-1
M	1.0	1.0
H	1.2	1.2

Similarly, design values of bending moments in columns are determined by the formula (5.4) from P100-1/2013 and (5.9) from SR EN 1998-1-1:

$$M_{d,c,i} and M_{d,c,j} = \gamma_{Rd} \cdot M_{R,c,i/j} \cdot \min\left(1, \frac{\sum M_{R,b}}{\sum M_{R,c}}\right) \quad (5)$$

Where:

MR,c,i/j - the value of the moment at the end of "i" or "j" of the column, for the sense of the seismic bending moment;YRd - over strength factor (Table 4) which takes into account steel strain-hardening of the longitudinal steel and shrinkage of concrete; ∑M(R,c) - the sum of the design values of the capable moments of the columns in the node; ∑M(R,b) - the sum of the design values of the capable moments of the beams in the node.

Table 4. Limit values for ϒRd for beams according to ductility class and standard

Ductility class	ϒRd	
	P100-1/2013	EN 1998-1-1
M	1.0	1.1
H	1.3 (for the structure base) 1.2 (for the other levels)	1.3

According to P100-1/2013 (Chapter 5.2.3.3.2. formula 5.1.) and SR EN 1998-1-1 (Chapter 4.4.2.3. formula 4.29.), structure nodes from ductility classes H and M, located in seismic areas will verify the formula:

$$\sum M_{R,c} \geq \gamma_{Rd} \sum M_{R,b} \quad (6)$$

For ductility class H, the formula states that the sum of capable moments of the columns which go into a node must be bigger with 20% and with 30%, than the sum of capable moments of the beams.

3. DESIGNING THE RESISTANCE CAPACITY USING GRAITEC ADVANCE DESIGN

It is considered the modal analysis of a 3 storey steel frame as presented in the Figure no.1. For the dynamic model 3 translational DOFs are granted along the OX and OY orthogonal directions in plane, according to the governing directions of the shaking table.
For the structure in Figure 1, located in an area with high seismicity (ag = 0.28g) design efforts must be determined, in the elements of the transverse frame (Figure3.2), and also the verification of its nodes.
In ADVANCE Design all verifications can be done automatically according to Romanian standard P100-1/2013 (or SR EN 1998-1-1 with the National Appendix) and SR EN 1992-1-1.

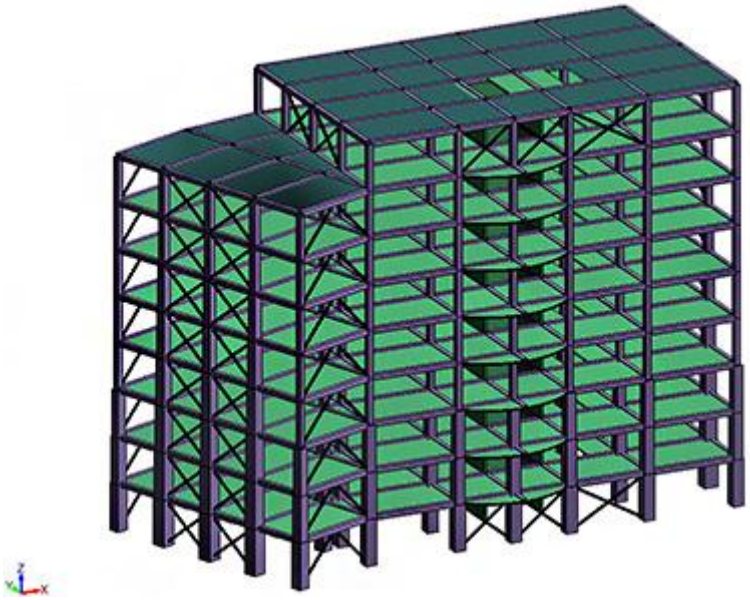

Figure 1. 3D view of the analyzed structure

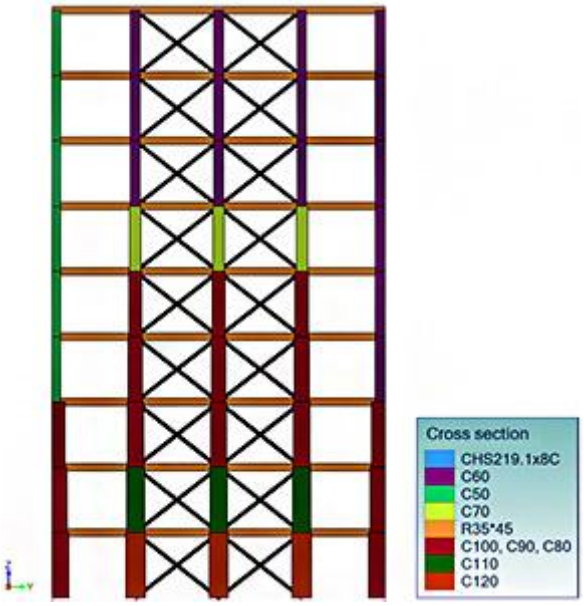

Figure 2. Solicited transverse frame

The structural system consists of reinforced concrete frames (resistance class C30/37) reinforced by the central vertical bracing (made of S355 steel) around the perimeter and a central core made of reinforced concrete walls (resistance class C30/37). The value of the behavior factor q, for both directions of seismic action, is 4.725 placing the structure in the ductility class M.

ADVANCE Design automatically determines, with the Concrete calculation engine, an optimal solution for actual reinforcement areas from beams and columns and later, verifies the prioritizing method for structural elementsfor the nodes of the analyzed frame.The theoretical areas of reinforcement and also the real areas of reinforcement, for beams and columns are calculated automatically according to the Romanian standard SR EN 1992-1-1 and the National Appendix.

Figure 3 gives the longitudinal and transverse reinforcement solution offered by ADVANCE Designfor one of the beams.

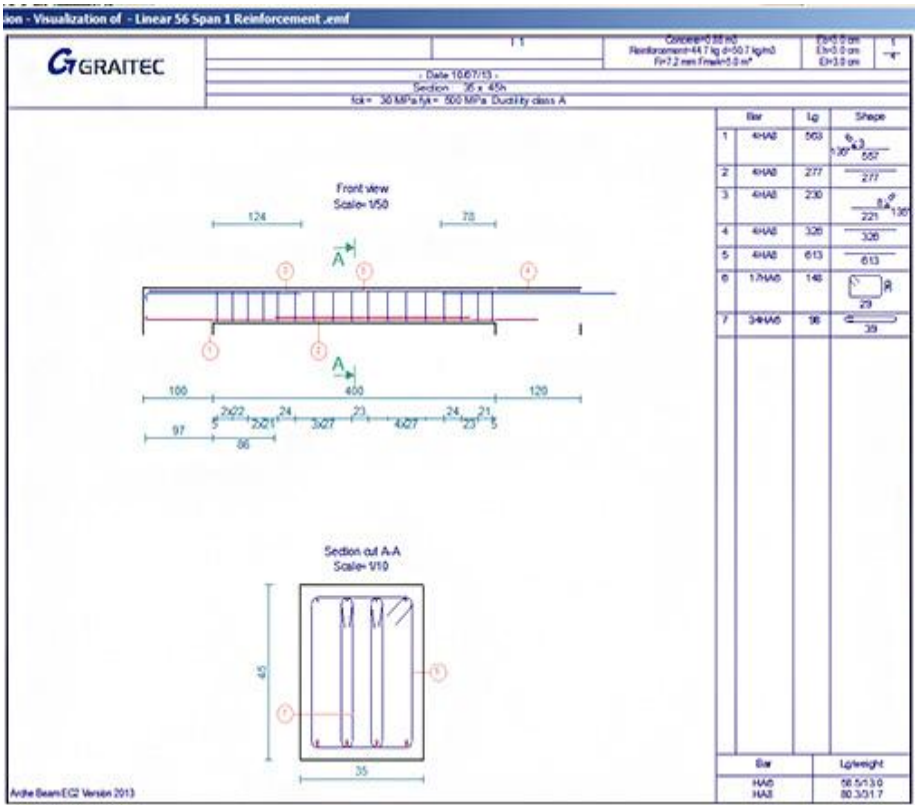

Figure 3. Reinforcement solution offered by ADVANCE Design for a beam

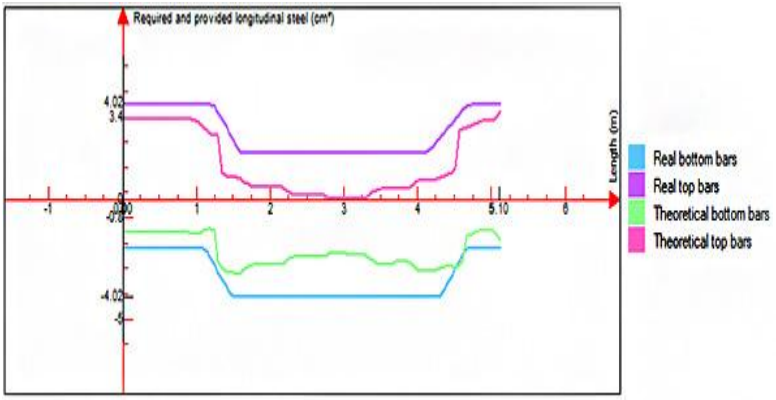

Figure 4. Theoretical and real areas of reinforcement

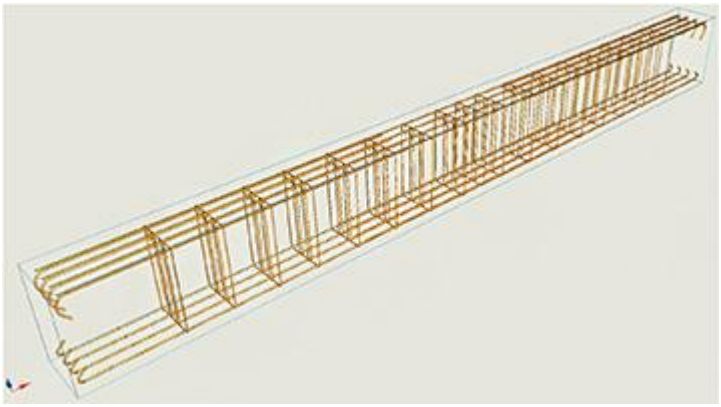

Figure 5. 3D view of the reinforced beam casing

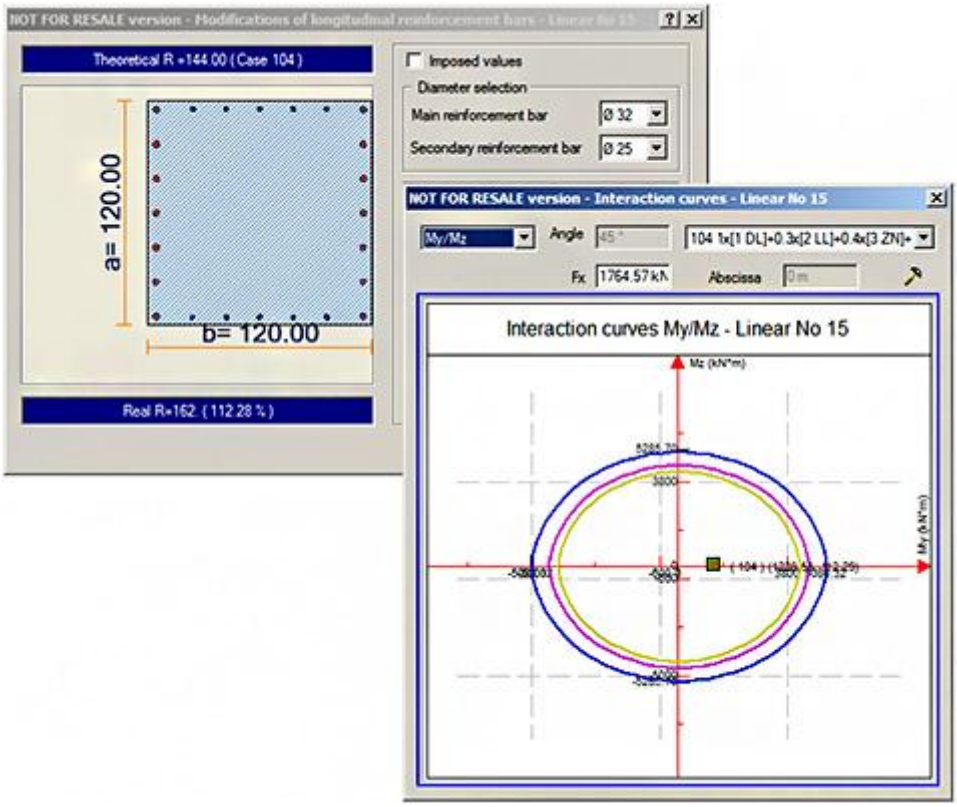

Figure 6. Longitudinal area of reinforcement and interaction curves for columns

The verification of the design capability done with ADVANCE Design requires the verification of reinforced concrete frame nodes. The verification is done with

formula 5.1 (chapter 5.2.3.3.2) if P100-1/2013 is used, and formula 4.29 (chapter 4.4.2.3.) if SR EN 1998-1-1 is used. For the determination of the capable moments from beams and columns (the calculation of parameters MR,c, MR,b from the above relations) real reinforcements will be used, automatically calculated with ADVANCE Design. The nodes which do not meet the verification formula will be marked in a specific calculation note (Figure 7).

Verification of beams-columns nodes (local coordinate system) [kN*m]										
Beam	Comb	Node	Σ(Mrc) Z	γRd	Σ(Mrb) Z	Σ(Mrc) > γRd * Σ(Mrb) Z	Σ(Mrc) Y	γRd	Σ(Mrb) Y	Σ(Mrc) > γRd * Σ(Mrb) Y
417	104	32398	1215.37	1.20	176.11	OK	1215.37	1.20	241.81	OK
	105	32398	1233.08	1.20	176.11	OK	1233.08	1.20	241.81	OK
	108	32398	1210.94	1.20	176.11	OK	1210.94	1.20	241.81	OK
	109	32398	1228.65	1.20	176.11	OK	1228.65	1.20	241.81	OK
	112	32398	1253.88	1.20	176.11	OK	1253.88	1.20	241.81	OK
	113	32398	1236.07	1.20	176.11	OK	1236.07	1.20	241.81	OK
427	104	36535	1144.06	1.20	176.11	OK	1144.06	1.20	241.81	OK
	105	36535	1050.81	1.20	176.11	OK	1050.81	1.20	241.81	OK
	108	36535	1139.58	1.20	176.11	OK	1139.58	1.20	241.81	OK
	109	36535	1046.19	1.20	176.11	OK	1046.19	1.20	241.81	OK
	112	36535	1172.46	1.20	176.11	OK	1172.46	1.20	241.81	OK
	113	36535	1265.30	1.20	176.11	OK	1265.30	1.20	241.81	OK
437	104	39203	154.93	1.20	83.91	OK	154.93	1.20	158.14	Failed
	105	39203	129.12	1.20	83.91	OK	129.12	1.20	158.14	Failed
	108	39203	152.27	1.20	83.91	OK	152.27	1.20	158.14	Failed
	109	39203	126.46	1.20	83.91	OK	126.46	1.20	158.14	Failed
	112	39203	183.33	1.20	83.91	OK	183.33	1.20	158.14	Failed
	113	39203	209.15	1.20	83.91	OK	209.15	1.20	158.14	OK
453	104	40344	287.44	1.20	68.21	OK	287.44	1.20	124.06	OK
	105	40344	281.51	1.20	68.21	OK	281.51	1.20	124.06	OK
	108	40344	286.49	1.20	68.21	OK	286.49	1.20	124.06	OK
	109	40344	280.52	1.20	68.21	OK	280.52	1.20	124.06	OK
	112	40344	291.71	1.20	68.21	OK	291.71	1.20	124.06	OK
	113	40344	297.64	1.20	68.21	OK	297.64	1.20	124.06	OK
463	104	42546	77.73	1.20	176.11	Failed	77.73	1.20	195.66	Failed
	105	42546	58.96	1.20	176.11	Failed	58.96	1.20	195.66	Failed
	108	42546	75.24	1.20	176.11	Failed	75.24	1.20	195.66	Failed
	109	42546	56.46	1.20	176.11	Failed	56.46	1.20	195.66	Failed
	112	42546	85.74	1.20	176.11	Failed	85.74	1.20	195.66	Failed
	113	42546	104.52	1.20	176.11	Failed	104.52	1.20	195.66	Failed
473	104	41771	549.58	1.20	176.11	OK	549.58	1.20	195.66	OK
	105	41771	550.61	1.20	176.11	OK	550.61	1.20	195.66	OK
	108	41771	547.43	1.20	176.11	OK	547.43	1.20	195.66	OK
	109	41771	548.46	1.20	176.11	OK	548.46	1.20	195.66	OK
	112	41771	552.47	1.20	176.11	OK	552.47	1.20	195.66	OK
	113	41771	551.44	1.20	176.11	OK	551.44	1.20	195.66	OK
483	104	41124	549.54	1.20	136.42	OK	549.54	1.20	195.66	OK
	105	41124	532.45	1.20	136.42	OK	532.45	1.20	195.66	OK
	108	41124	547.34	1.20	136.42	OK	547.34	1.20	195.66	OK
	109	41124	530.25	1.20	136.42	OK	530.25	1.20	195.66	OK
	112	41124	556.20	1.20	136.42	OK	556.20	1.20	195.66	OK
	113	41124	573.28	1.20	136.42	OK	573.28	1.20	195.66	OK
493	104	43333	60.52	1.20	88.06	Failed	60.52	1.20	158.14	Failed
	105	43333	52.23	1.20	88.06	Failed	52.23	1.20	158.14	Failed
	108	43333	59.20	1.20	88.06	Failed	59.20	1.20	158.14	Failed
	109	43333	50.91	1.20	88.06	Failed	50.91	1.20	158.14	Failed
	112	43333	68.08	1.20	88.06	Failed	68.08	1.20	158.14	Failed
	113	43333	76.38	1.20	88.06	Failed	76.38	1.20	158.14	Failed

Figure 7. Verification of column-beams nodes in ADVANCE Design

For the reinforced concrete frames nodes which do not meet the verification formula from P100-1/2013 and SR EN 1998-1-1, ADVANCE Design may allow manual modification of the reinforcement solution used or may automatically make iterations in order to find optimal longitudinal reinforcements in columns, so that the specific conditions are met. Manually changing the beam reinforcement solution involves modifying the following parameters: anchorage length, bars longitudinal or transverse diameter, the number of longitudinal or transverse bars.

4. CONCLUSIONS

The Capacity Design method is generally applicable to reinforced concrete frames and enables users a proper sizing of columns and beams by checking the frame nodes, according to SR EN 1992-1-1, SR EN 1998-1-1 or P100-1/2013. GRAITEC ADVANCE Design includes all the norms and requirements, offering civil engineers a superior solution for the structural analysis and design of reinforced concrete.

While resistance capacity should lead to a safer and more accurate design process, engineers should keep in mind that the calculation models are only mathematical simulations of physical phenomena and cannot accurately predict the structural behavior. Too many uncertainties can occur and it is up to civil engineers to characterize as best as they can and as many parameters as they can.

References

1. GRAITEC, *Advanced Design 2014* - Users's Manual.
2. P 100 - 2013 *Romanian Aseismic Design Code*.
3. Octavian V. Roşca, Ioan P. Ciongradi, *"Metode numerice utilizate în programele de calcul automat al structurilor"* Ed. Acad. Society "Matei-Teiu Botez", Iaşi, 2003.

The Computer Analysis of an Offshore Concrete Gravity Platform

Marius-Andrei Miron [1], Octavian V. Roşca [2]
[1]*Research Student, Technical University"Gh. Asachi", Iaşi, 700050, Romania*
[2]*Structural Mechanics Department, Technical University"Gh. Asachi", Iaşi, 700050, Romania*

Summary

The design and analysis of a structure which is not onshore may become a difficult task for a civil engineer uninitiated in the field of offshore engineering. However, the aim of this paper is to provide a detailed evaluation of the loads, the structural analysis and modeling approach of an offshore concrete gravity structure using a finite element software, according to national and international standards. Topics covered range from water wave theories, structure-fluid interaction in waves to the prediction of extreme values of response from spectral modeling approaches.

KEYWORDS: structural analysis, modal analysis, offshore platform.

1. INTRODUCTION

The analysis, design and construction of offshore structures compatible with the extreme offshore environmental conditions is a most challenging and creative task faced by the engineering profession. Over the usual conditions and situations met by land-based structures, offshore structures have the added complication of being placed in an ocean environment where hydrodynamic interaction effects and dynamic response become major considerations in their design.

Gravity-based structures are fixed structures that are held in place against environmental actions solely by their weight plus that of any contained ballast, together with foundation resistance resulting from their weight and lateral resistance for any skirts. The majority of gravity structures are constructed of concrete although a very limited number have been built of steel.

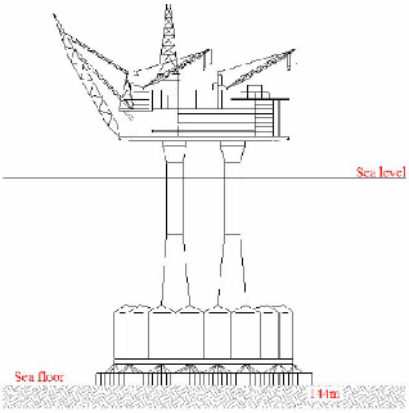

Figure 1. Statfjord B concrete gravity - based platform, Norway

Figure 2. Maureen steel gravity-based platform, U.K.

2. OTNIEL GBS PLATFORM

Despite the occasional setback – political and exploratory – the Black Sea continues to draw interest from international oil companies, including heavy hitters such as ExxonMobil, Total, Shell, and Repsol. Fewer than 100 offshore wells have been drilled in the Black Sea and, until recently, its deeper waters remained mostly unexamined by seismic surveys. Following the Kaliakra completion, Petroceltic mobilized the GSP Prometeu rig to Romania to drill two exploration wells on the Est Cobalcescu and Muridava concessions, Fig.3, in blocks 28 and 27, respectively. The Cobalcescu South-1 well, spudded at the end of August, is targeting two Miocene intervals that that the company says contain a combined 404 billion cubic feet(bcf) of gas. The second well, Muridava-1, has multiple targets in the Eocene, Paleocene, and Creataceous formations with combined resources of 169 bcf. The Muridava concession includes the undeveloped Olimpiskaya discovery. Petroceltic plans to drill four more exploration wells on the two blocks in 2014.

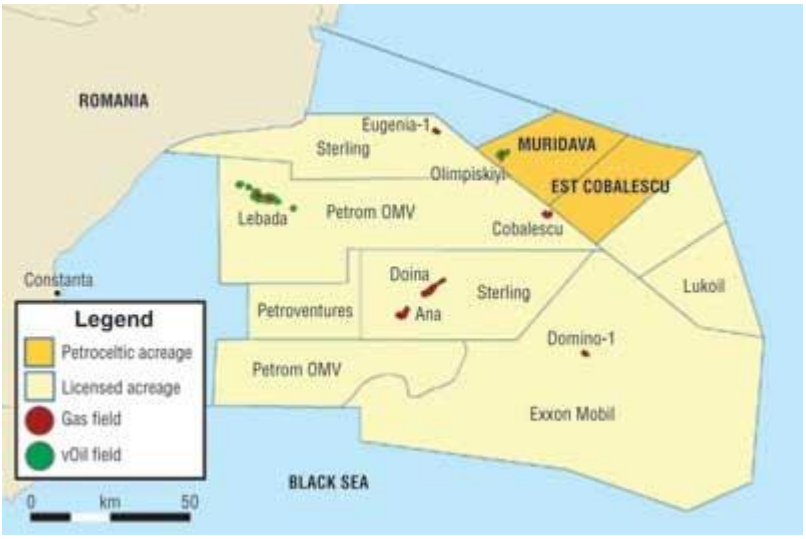

Figure 3. Licensed acreage Offshore Romania

The platform analyzed in this present article may be proposed to be constructed in the Black Sea, Olimpiskaya discovery, in approximately 90 meters of water . Even though this gravity-based structure (GBS) has not a name, yet, we will refer to it as Otniel GBS as this platform is his concept. This structure is constructed of pre-stressed reinforced concrete with a submerged caisson and central shaft. It would have a design lift of 50 years and could support further developments. The topside consists of drilling facilities, wellheads and support services such as accommodations for 120 to 130 persons, utilities and a helicopter pad. The key dimensions are:

- deck: 41.80 x 46.0 m;

- base raft foundation: 78.8 x 78.8 m;

- height of GBS: 104.23 m.

Vertical and horizontal sections are given in below drawings.

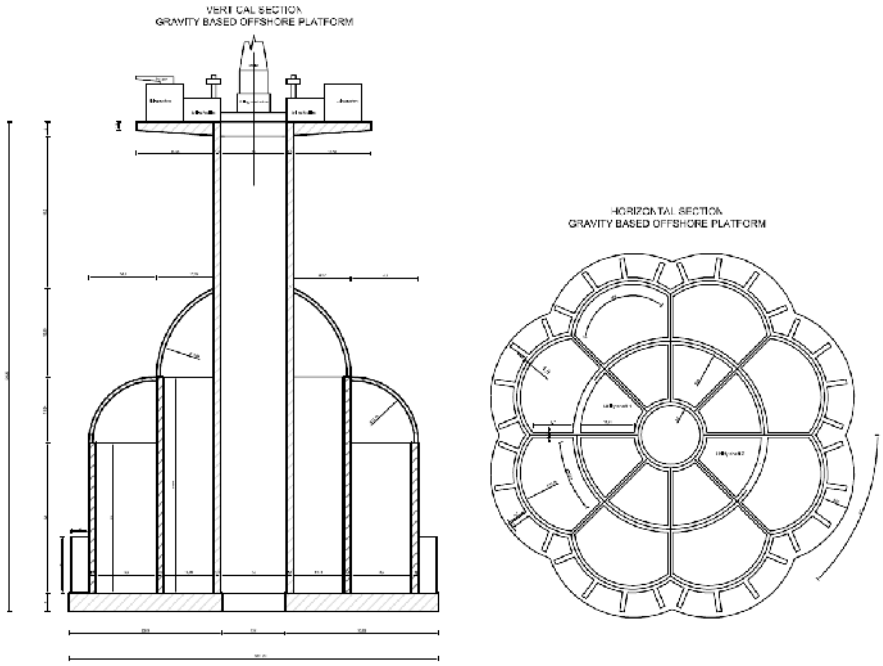

Figure 4. Vertical and horizontal sections of Otniel GBS

3. LOADS ON OFFSHORE STRUCTURES

Loads are differentiated as static and dynamic. The static loading on the structure originates from gravity loads, deck loads, hydrostatics loads and current loads. The dynamic loads come from the variable wind and waves.

Loads may be classified as follows: $\begin{cases} dead\ loads\ (D) \\ deformation\ loads\ (T) \\ live\ loads\ (L) \\ environmental\ loads\ (E) \\ accidental\ loads\ (A). \end{cases}$

3.1 Dead loads

Dead loads are permanent static loads such as:

-weight of the structure: $G = V \cdot \gamma\ [tons]$

$$V_{deck} = 41{,}8 \cdot 46 \cdot 3 - \left(\frac{41{,}8 \cdot 46 \cdot 3}{2}\right) = 2884{,}2\ m^3$$

$$V_{deck\ rigidity} = \left(\frac{24 \cdot 10}{2}\right) \cdot 4 \cdot 0{,}8 + \left(\frac{16 \cdot 10}{2}\right) \cdot 2 \cdot 0{,}8 + \left(\frac{13 \cdot 10}{2}\right) \cdot 2 \cdot 0{,}8 = 616\ m^3$$

$$V_{tower} = 101 \cdot \left(\frac{\pi \cdot 17^2}{4} - \frac{\pi \cdot 14^2}{4}\right) = 7377{,}25\ m^3$$

$$V_{interior\ walls} = 8 \cdot \frac{1{,}5 \cdot (8{,}2 + 11{,}5) \cdot 35}{2} = 4137\ m^3$$

$$V_{truncated\ cone} = \frac{\pi h(R^2 + r^2 + Rr)}{3}$$

$$= \frac{\pi \cdot 34 \cdot (20{,}75^2 + 16{,}5^2 + 20{,}75 \cdot 16{,}5)}{3}$$

$$- \frac{\pi \cdot 34 \cdot (19{,}25^2 + 15{,}9^2 + 19{,}25 \cdot 15{,}9)}{3} = 4120{,}9\ m^3$$

$$V_{well\ walls} = 32 \cdot 1{,}5 \cdot 8 \cdot 20{,}2 = 7756{,}8\ m^3$$

$$V_{cylinder} = 20{,}75^2 \cdot \pi \cdot 32 - 19{,}25^2 \cdot \pi \cdot 32 = 6031{,}86\ m^3$$

$$V_{well} = \left(13{,}95^2 \cdot \pi + \frac{120}{180} - 12{,}45^2 \cdot \pi + \frac{120}{180}\right) \cdot 8 \cdot 1{,}5 \cdot 32 = 48028{,}31\ m^3$$

$$V_{raft} = 4835{,}4 \cdot 4 - (333{,}25 \cdot 2 \cdot 8) = 14009{,}6\ m^3$$

$$V_{domes} = 177{,}9 \cdot 0{,}6 \cdot 8 + (526{,}7 \cdot 0{,}8 \cdot 8) = 4224{,}8\ m^3$$

$$V_{well\ rigidities} = 16 \cdot 4{,}2 \cdot 1 \cdot 12 = 806{,}4\ m^3$$

$$V_{Total} = 99993{,}12\ m^3$$

$$G = V_{Total} \cdot \gamma = 99993{,}12 \cdot 2500 = 249982800\ kg = 250000\ tons$$

-equipment that cannot be removed

-external hydrostatic pressure: $p = \rho g h$

$\rho = water\ density \quad g = gravitational\ acceleration \quad h = water\ depth$

$\rho = 1000\ kg/m^3$

$h = 90\ m$

$g = 9{,}81\ m/s^2$

$p = 1000 \cdot 9{,}81 \cdot 90 = 882900\ Pa = 883\ KN/m^2$

3.2 Deformation loads

Deformation loads consider the effects of the following:
- temperature, including heat of hydration;
- differential settlements and uneven seabed;
- creep and shrinkage;
- initial strains imposed by pre-stressing cables.

3.3 Live loads

Live loads may be static or dynamic, may vary in position and magnitude and may also result from operation of the structure. The following are representative examples:

- helicopters – 43,1 KN;
- loads induced by the operation of equipment;
- liquids stored internally;
- equipment and supplies;
- snow and accumulated ice.

3.4 Environmental loads

Environmental loads are due to natural phenomena such as waves, marine currents, winds and earthquakes.

3.4.1 Waves loads

Water force can be classified as forces due to waves and forces due to current. Wind blowing over the surface of the ocean drags water along with it, thus forming current and generating waves. The forces induced by ocean waves on platform are dynamic in nature. However, it is accepted in practice to design shallow water platforms by static approaches.

$-\ water\ depth, H = 90\ m$
$-\ wave\ height\ (amplitude), h = 12\ m$
$-\ wave\ period, T = 10\ s$
$-\ gravitational\ acceleration, g = 9{,}81\ m/s^2$
$-\ diameter, d = 17\ m$

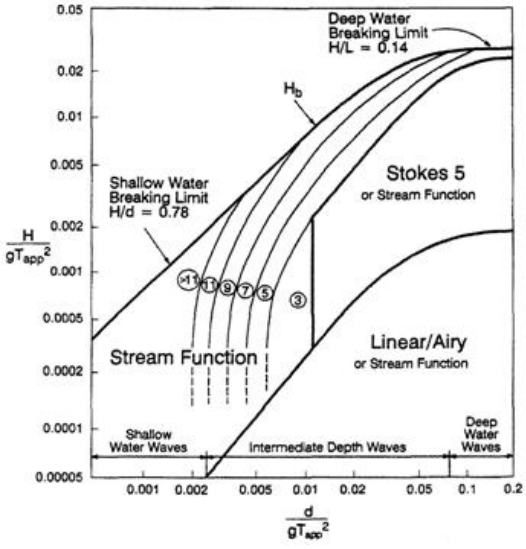

Figure 5. Region of application of wave theories(API, 2000)

$$\frac{H}{gT^2} = \frac{90}{9{,}81 \cdot 10^2} = 0{,}0917$$
$$\frac{d}{gT^2} = \frac{17}{9{,}81 \cdot 10^2} = 0{,}0173$$

Regular wave theories used for calculation of wave forces on fixed offshore structures are based on three parameters: water depth (d), wave height (h) and wave period (T). They are represented in Fig.6. Wave plus current kinematics are generated using 5th order Stokes wave theory and the forces on individual structural elements are calculating with Morison's equation:
$F(t) = F_I(t) + F_D(t)$, based on hydrodynamic drag and mass coefficients (CD and CM) .

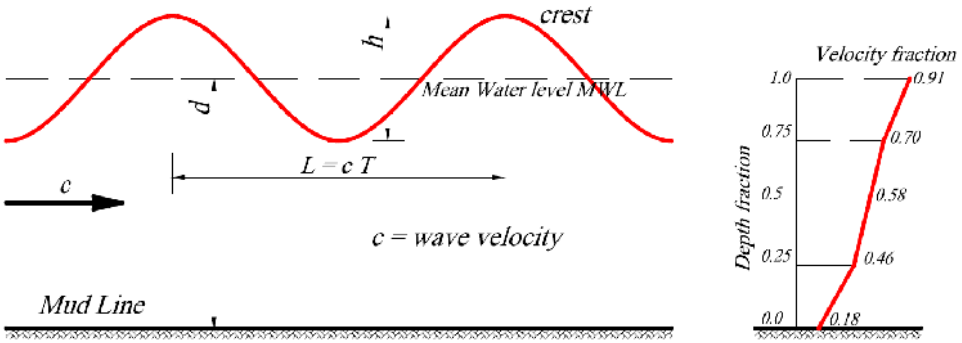

Figure 6. Wave coordinate system and typical wind and tidal current profile

$$F_I = \frac{\pi}{4} C_M \rho d^2 \omega^2 \frac{h}{2k}$$
$$F_D = \frac{1}{2} \rho C_D d \omega^2 \frac{h^2}{4} \frac{\left(\frac{\sinh 2kH}{4} + \frac{kH}{2}\right)}{k \sinh^2 kH}$$
$$L = \frac{gT^2}{2\pi} = \frac{9{,}81 \cdot 10^2}{2\pi} = 156{,}13\ m \qquad L = length\ of\ the\ wave$$
$$k = \frac{2\pi}{L} \frac{2\pi}{156{,}13} = 0{,}040 \qquad k = wave\ number$$
$$\omega = \frac{2\pi}{T} = \frac{2\pi}{10} = 0{,}628\ rad/s \qquad \omega = circular\ frequency$$
$$\rho = 1000 \frac{kg}{m^3} \qquad \rho = water\ density$$
$$F_I = \frac{\pi}{4} \cdot 2{,}0 \cdot 1000 \cdot 17^2 \cdot 0{,}628^2 \cdot \frac{12}{2 \cdot 0{,}040} = 26855192{,}29\ N = 26855{,}192\ KN$$

$$F_D = \frac{1}{2} \cdot 1000 \cdot 1{,}0 \cdot 17 \cdot 0{,}628^2 \cdot \frac{12^2}{4} \cdot \frac{\left[\frac{\sinh(2 \cdot 0{,}040 \cdot 90)}{4} + \frac{0{,}040 \cdot 90}{2}\right]}{0{,}040 \cdot \sinh(0{,}040 \cdot 90)^2} = 1527015{,}041\ N$$

$$= 1527{,}015\ KN$$

$$F = 26855{,}192 + 1527{,}015 = 28382{,}207\ KN$$

3.4.2 Current loads

Waves induce an orbital motion in the water in which they travel. These orbits are closed but experience a slight drift forward to wind surface effects. The current is actually induced by wave.

3.4.3 Wind loads

Wind loads on offshore structures can be evaluated using modelling approaches adopted for land-based structures but for conditions pertaining to ocean environments. The distinction here is that of an open sea presents a lower category of roughness to the free-stream wind, which leads to a more slowly varying mean wind profile with height and lower level of turbulence intensity than encountered on land.

For combination with wave loads we have: 1 minute sustained wind speeds combined with extreme waves and 3 seconds gusts.

$$F_w = \frac{1}{2}\rho v^2 C_s A\ (static\ wind\ force)$$

ρ=air density

v=wind velocity

A=exposed area

C_s=shape coefficient

ρ=1,225 kg/m^3

$$\frac{v_h}{v_H} = \left(\frac{h}{H}\right)^{\frac{1}{n}}$$

v_h=wind velocity at height, h=21 m

v_H=wind velocity at 10 m above water level

v_H=164 km/h

$\frac{1}{n} = \frac{1}{13}$ -for gusts

$\frac{1}{n} = \frac{1}{8}$ -for sustained winds in the open sea

$$\frac{v_h}{164}=\left(\frac{21}{10}\right)^{\frac{1}{13}} \Rightarrow v_h=\frac{164\cdot 21^{\frac{1}{13}}}{10^{\frac{1}{13}}}=173{,}632\ \frac{km}{h}=48{,}23\ \frac{m}{s}$$

$$\frac{v_h}{164}=\left(\frac{21}{10}\right)^{\frac{1}{8}} \Rightarrow v_h=\frac{164\cdot 21^{\frac{1}{8}}}{10^{\frac{1}{8}}}=179{,}937\ \frac{km}{h}=50\ m/s$$

C_s=1,5-beams and sides of buildings
1,0-total projected area of platform
0,5-cylindrical sections

$A_{exposed}=A_{tower}+A_{deck}+A_{buildings}$

$$A_{tower}=\frac{2\pi R}{2}\cdot h=\frac{2\pi\cdot 8{,}5}{2}\cdot 10=267{,}035\ m^2$$

$$A_{deck}=1{,}5\cdot 46=69\ m^2$$

$$A_{buildings}=10\cdot 18+4\cdot 8+2\cdot 9=230\ m^2$$

Sustained wind

$$F_w^t=\frac{1}{2}\cdot 1{,}225\cdot 50^2\cdot 1{,}0\cdot 267{,}035=408897{,}3438\ N=409\ KN$$

$$F_w^d=\frac{1}{2}\cdot 1{,}225\cdot 50^2\cdot 1{,}0\cdot 69=105656{,}25\ N=105{,}6\ KN$$

$$F_w^b=\frac{1}{2}\cdot 1{,}225\cdot 50^2\cdot 1{,}0\cdot 230=352187{,}5\ N=352{,}2\ KN$$

Gusts

$$F_w^b=\frac{1}{2}\cdot 1{,}225\cdot 48{,}23^2\cdot 1{,}0\cdot 230=327693{,}9723\ N=328\ KN$$

$$F_w^t=\frac{1}{2}\cdot 1{,}225\cdot 48{,}23^2\cdot 1{,}0\cdot 267{,}035=380459{,}825\ N=380{,}5\ KN$$

$$F_w^d=\frac{1}{2}\cdot 1{,}225\cdot 48{,}23^2\cdot 1{,}0\cdot 69=98308{,}1917\ N=98{,}3\ KN$$

3.4.4 Earthquake loads

The damaging effect of earthquakes is essentially, but not exclusively, the result of horizontal oscillatory accelerations of the soil being transferred to structures above ground level through their foundations.

The derivation of design parameters to provide for seismic loading is to a large extent a qualitative process. Specialist advice, particularly in relation to geophysical and geological aspects, should be sought where there is significant seismic activity of the danger thereof and reference should be made to local regulations and other authoritative references for guidance on the appropriate seismic loading to be used in design. The seismic action on structure was

calculated according to P100-2013, Romanian Earthquake Standard, and is considered to be damped by water. Although, the seismic action was considered with the following characteristics:
Peak ground design acceleration GDA: a_g=0.3g;
Corner period: T_c=0,7;
Importance factor: Υ_I= 1,4;

3.4.5 Ice (sheet ice, first-year and multiyear ridges, icebergs, etc.)

$F_i = C_i f_c A - impact\ load$

C_i= coefficient accounting for shape, rate of load application and other factors, with usual values between 0.3 and 0.7

$f_c = compressive\ strength\ of\ ice$

$A = exposed\ area\ of\ structure$

$f_c = 9\ MPa$

$d = 0{,}4\ cm,$ crystal size

$\theta = -12°\ C,$ temperature

$$A_{exposed} = \frac{2\pi R}{2} \cdot h = \frac{2\pi \cdot 8{,}5}{2} \cdot 2 = 54{,}035\ m^2$$

$$F_i = 0{,}3 \cdot 9 \cdot 10^6 \cdot 54{,}035 = 145894500\ N = 145894{,}5KN$$

3.5 Accidental loads

Accidental loads result from accidents or misuse, such as:
- collision from service boats, barges, and ships;
- dropped objects;
- explosions;
- loss of assumed pressure differential.

4. STRUCTURAL MODELLING OF THE PLATFORM

4.1 Material characteristics

Concrete C32/40 (Bc40):

f_{ck}= (0, 87-0,002*f_{bk})*f_{bk}= 31, 6 N/mm²
f_{tk}= 0, 22*(f_{ck})$^{2/3}$= 2, 2 N/mm² f_c^*= 22, 5 N/mm² f_t^*= 1, 45 N/mm²
f_{b0}= 35 N/mm² f_c= 19, 125 N/mm² f_t= 1, 123 N/mm²

E_b=36000 N/mm²
Normal renforcement: PC52 →f_a= 300 N/mm²
Post-tensioned reinforcement: SPB-I ϕ7

f_{pk}= 1570 N/mm² f_p= 1260 N/mm² E_p= 200000 N/mm²

4.2 Load cases

Table 1. Load cases and the values

No.crt.	*Load*	*Value*	*Unit*
1	*Self-Weight*	*2499828*	*KN*
2	*Dead Load*	*90290*	*KN*
3	*Hydrostatic pressure (water)*	*883*	*KN/m²*
4	*Hydrostatic pressure (oil)*	*569*	*KN/m²*
5	*Live Load (operating)*	*8,5*	*KN/m²*
6	*Live Load (accommodations)*	*3,2*	*KN/m²*
7	*Live Load (helicopter)*	*43,1*	*KN*
8	*Snow*	*2,5*	*KN/m²*
9	*Waves*	*28382,207*	*KN*
10	*Wind (sustained)*	*866,8*	*KN*
11	*Wind (gust)*	*806,8*	*KN*
12	*Ice*	*145894,5*	*KN*

4.3 Load combinations

The required strength of the structure and each member should be equal to or greater than the maximum calculated by the following:

$U = 1.2(D + T) + 1.6L_{max} + 1.3E_0$

$U = 1.2(D + T) + 1.2L_{max} + \gamma_L E_{max}$

$U = 0.9 (D + T) + 0.9L_{min} + \gamma_L E_{max}$

L_{max} = maximum live load

L_{min} = minimum live load

E_0=frequently occurring environmental load (e.g., monthly)

E_{max} = extreme environmental load

Υ_L = load multiplier

Table 2. Load combinations the partial factors that are affecting them

No. crt.	Loads	Load Combinations									
		Fundamental	Special on Y	Special on X	Special on X−0,3Y	Special on Y−0,3X	Service	Extreme environmental conditions		Storm	Temporary loading cases
								a	b		
		Safety factors									
1	Self-Weight	1,2	0,9	0,9	0,9	0,9	1,0	1,1	0,9	1,2	1,0
2	Dead Load	1,2	0,9	0,9	0,9	0,9	1,0	1,1	0,9	1,2	1,0
3	Hydrostatic pressure (water)	1,2	0,9	0,9	0,9	0,9	1,0	1,1	0,9	1,2	1,0
4	Hydrostatic pressure (oil)	1,6	0,9	0,9	0,9	0,9	1,0	1,1	0,8	1,2	
5	Live Load	1,6	0,9	0,9	0,9	0,9	1,0	1,1	0,8	1,2	
6	Snow	1,6	0,9	0,9	0,9	0,9	1,0	1,1	0,8	1,2	
7	Waves	1,3	1,3		1,3	1,3	1,0	1,35	1,35	1,3	
8	Wind (sustained)	1,3	1,3		1,3	1,3	1,0				
9	Wind (gust)							1,35	1,35	1,3	
10	Ice		1,0	1,0	1,0	1,0	1,0	1,35	1,35		
11	Earthquake on X direction			1,4	1,4	0,3					
12	Earthquake on Y direction		1,4		0,3	1,4					

4.4 Meshing the platform with Autodesk Robot Structural Analysis FE software

Free-meshing is automatically generated by the computational software upon the selection of fine-mesh level . There are few meshing levels available for selection, in which each level assigns specific Qn, in accordance to the model geometry. For fine-meshing, where more elements are employed, longer computation time is required. The free-meshing has the characteristic of equally

distributing the mesh-elements all over the numerical model. As a result, the mesh distribution at the crack-tip zone is similar to the areas remote from the tip. This homogeneous-type of meshing is shown in the Fig.7.

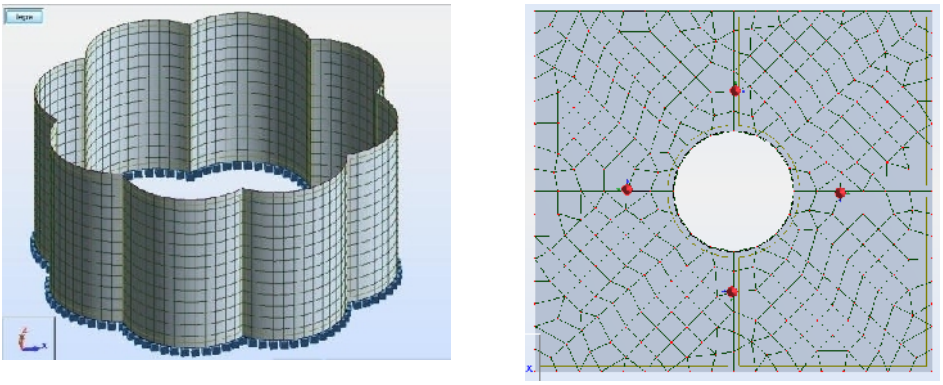

Figure 7. Free meshing of the shells and deck of GBS platform

5. STRUCTURAL RESPONSE OF THE MODEL

5.1 Efforts in the shells

Moments for the shell elements are given in kNm/m in the local system of axes of the plates a) on vertical sections:

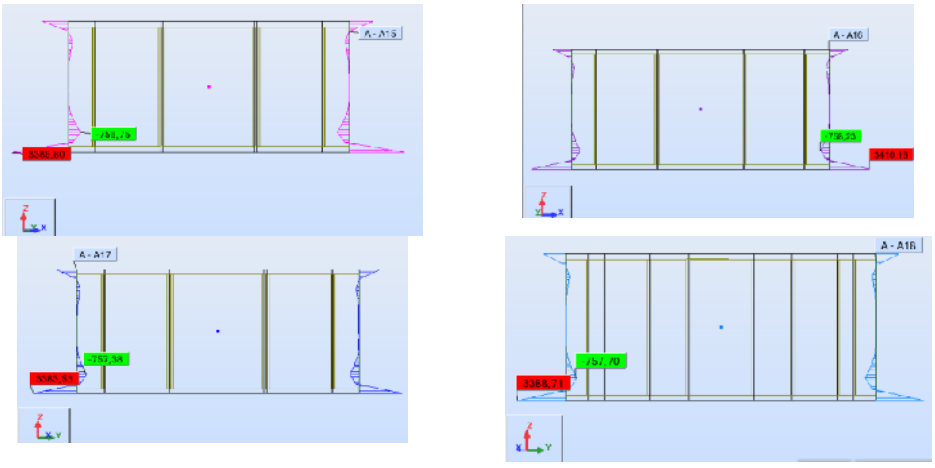

Figure 8. Efforts in the shells on vertical sections

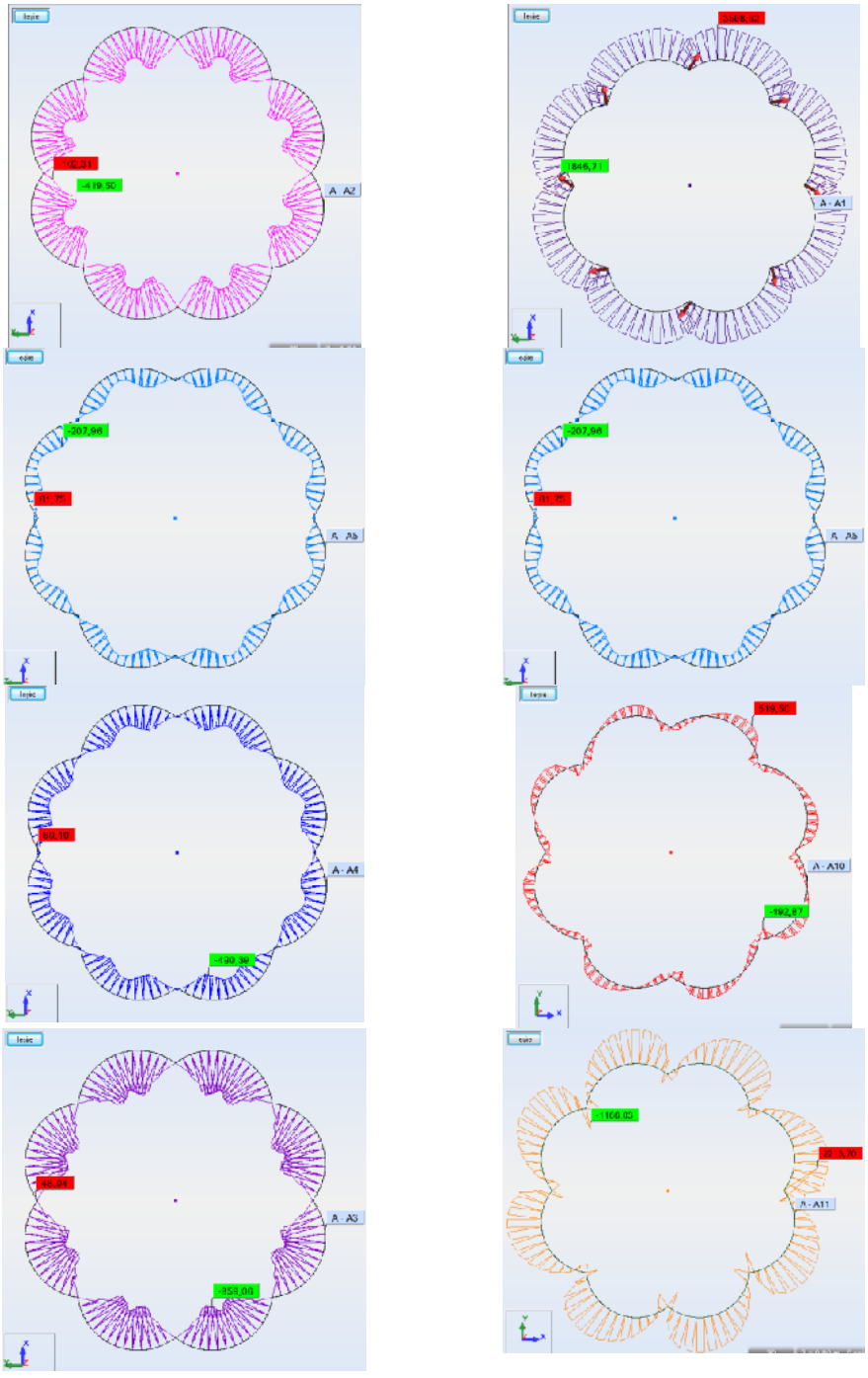

Figure 9. Efforts in the shells on horizontal sections

5.2 Efforts in the shaft tower

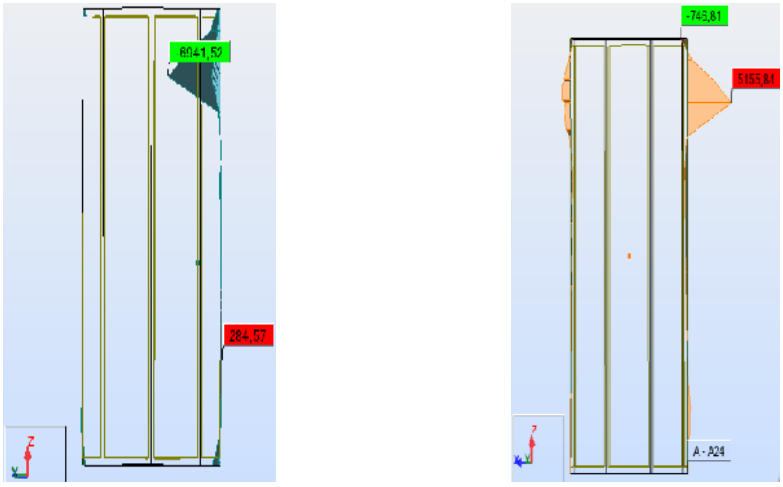

Figure 10. Efforts in the shaft tower on vertical sections

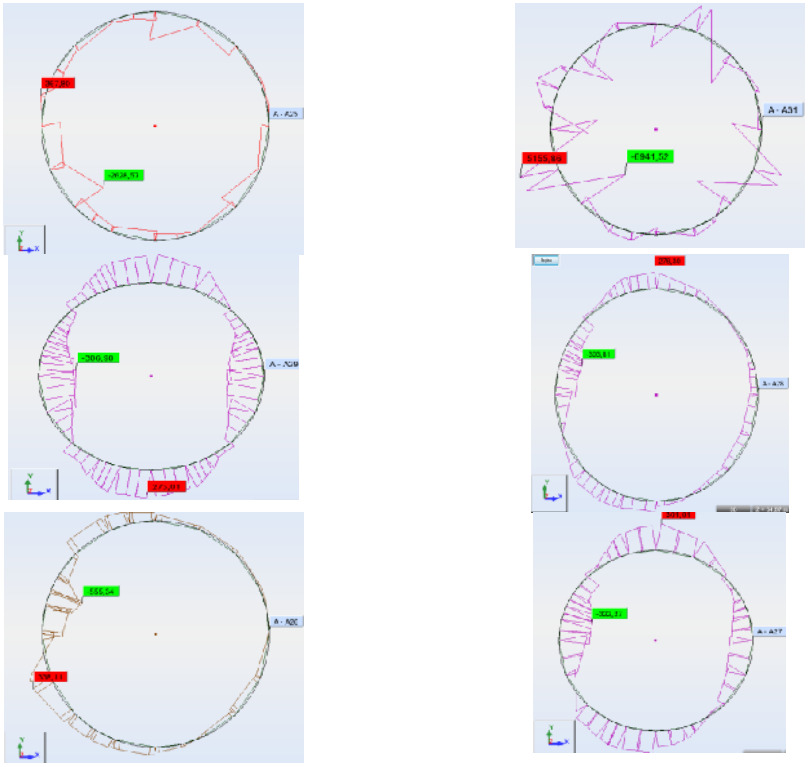

Figure 11. Efforts in the shaft tower on horizontal sections

5.3 Efforts in the deck structure

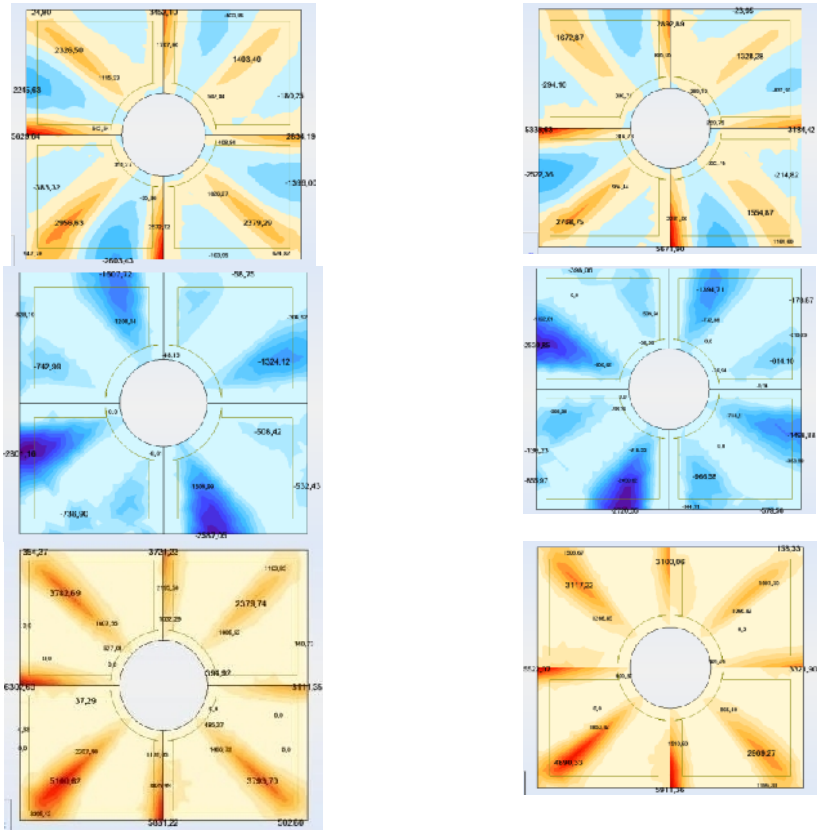

Figure 12. Efforts in the deck structure

5. CONCLUSIONS

The free-meshing technique has shown to be an appropriate approach for designing and analysing the large structure studied in this particular case.

The concrete structure has a large stiffness compared with that provided by steel platforms. Furthermore, the design platform has excellent resistance to impact loads due to the concrete material and the reinforcement system. This is a fact that has been proven through history, and the result is that concrete is widely used in military installations, shelters, in buildings which need to be failsafe and which are regarded as exposed to terror attacks.

The structural response show that this concrete gravity-based structure has been design properly, using the right approaches, and it would be able to resist to the environment provided by the Black Sea.

References

1. Offshore Standard DNV –OS - C502 *"Offshore Concrete Structures"* October 2010.
2. Recommended Practice DNV- RP- C205 *"Environmental Conditions and Environmental Loads"* October 2010.
3. P100-2013, *Romanian Aseismic Design Code.*
4. *Building Code Requirements for Structural Concrete* (ACI 318-05) and commentary (ACI 318R – 05).
5. *Specifications for Structural Concrete* (ACI 301-10).
6. *Guide for Design and Construction of Fixed Offshore Concrete Structures* (ACI 357R-84,Reapproved 1997).
7. *Design and Construction of Circular Pre stressed Concrete Structures with Circumferential Tendons* (ACI 373R-97).
8. *Concrete Shell Structures – Practice and Commentary* (ACI 334.1R-92).
9. Ivar Holand, Ove T. Gudmestad, Erik Jersin *"Design of Offshore Concrete Structures"*, Spoon Press 2000, London.
10. Subrata K. Chakrabarti *"Handbook of Offshore Engineering"*, Elsevier 2005, Oxford
11. Ben C. Gerwick, Jr. *"Construction of Marine and Offshore structures"*, CRC Press 2007, New York.

Hyperelastic Models for Finite Element Analysis of Elastomeric Bearings

Daniela Oanea (Fediuc) [1], Mihai Budescu [1], Vasile-Mircea Venghiac [1], Sergiu Băetu [1]

[1]*Department of Structural Mechanics, "Gheorghe Asachi" Technical University, Iaşi, 700050, Romania*

Summary

The elastomers are materials which present large elastic deformations and return to their initial shape without permanent deformations. High values of elastomer deformations require the use of hyperelastic material models based on the strain energy. The strain energy function can be defined using several models, such as Neo-Hookean, Mooney-Rivlin, Polinomial, Yeoh, Gent, Ogden, Arruda-Boyce. The material constants and the parameters of hyperelastic models can be determined from the experimental tests.

The paper presents the finite element analysis in ANSYS program of an elastomeric bearing used in seismic base isolation under compression, compression and shear respectively.

KEYWORDS: base isolation, elastomeric bearings, hyperelastic models.

1. INTRODUCTION

The finite element computer programs are used for the analysis of elastomeric bearings. The numerical simulation has an important role in the manufacturing process of bearings used in the seismic base isolation obtaining a high performance of the bearings. In most structural analysis programs, mathematical programs which describe the mechanical properties of elastomers used in the design of anti-seismic bearings are implemented.

Elastomers, such as rubber and other polymeric materials, are hyperelastic materials (materials which present large elastic deformations and return to their initial shape without permanent deformations). Elastomers are materials that do not respect the Hooke's law and their Poisson ratio is 0.5.

The hyperelastic material models are characterized by nonlinear behaviour, usually difficult to implement in programs. The accuracy of these models depends on the

load type and deformation range. The steel is modelled as a linear elastic isotropic material (Kumar, M., 2012).

The reinforcement of the bearings restricts the horizontal displacement resulted from vertical loads and thus increases the vertical stiffness and load capacity of the bearing. The vertical stiffness of an elastomeric bearing depends on the geometry, the shear modulus, compression modulus of the elastomer and the elastic modulus of the reinforcement (Gerhaher, U., et *al*., 2011). According to EN 1337-3, the elastomeric bearings may be designed with or without steel cover plates at the bottom and top.

The maximum shear strain of the elastomer is limited to 500% (ASRO, 2006). These high values of the strains require the use of hyperelastic material models based on the strain energy function (Fig. 1), (Gerhaher, U., et *al*., 2011).

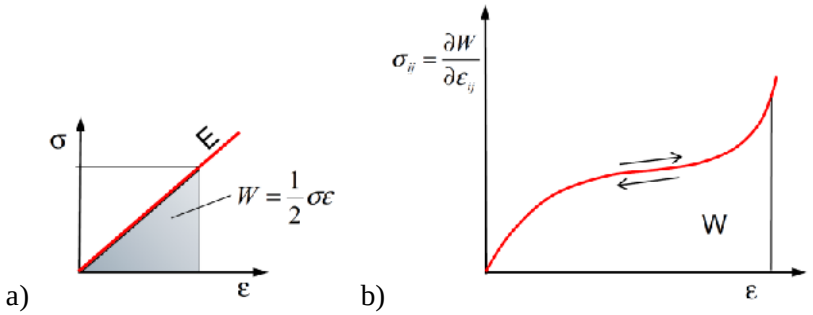

Figure 1. The stress-strain curve for: a) linear elastic material; b) hyperelastic material (Gerhaher, U., et *al*., 2011)

Parts of sulphur bridges connecting the long-chained molecules get broken when the first strains of the elastomer occur. Due to the mechanical degradation of the material (Mullins effect), the elastomer behaves less stiff in the next deformation cycles. Therefore, the elastomer shear modulus presents different values at different load levels depending on the maximum applied strain (Gerhaher, U., et *al*., 2011).

2. HYPERELASTIC MODELS

The strain energy function can be defined using several models, such as Arruda-Boyce, Mooney-Rivlin, Neo-Hookean, Ogden, Polinomial, Van der Waals, Yeoh, Gent etc.

The applicability of hyperelastic models used in the elastomer analysis is presented in Tab. 1 (Bhashyam, G. R., 2002).

Table 1. Hyperelastic models

Material Model	The strain range
Neo-Hookean	< 30%
Mooney-Rivlin	30% - 200%
Polinomial	< 300%
Gent	< 300%
Arruda Boyce	< 300%
Ogden	< 700%

2.1. The Neo-Hookean model

The Neo-Hookean model is a model of hyperelastic materials that is used to describe the stress-strain behaviour of the material; the model is similar to Hooke's law. For most materials, the relationship between the stress-strain is initially linear, but at some point it becomes nonlinear (Kim, B., et *al*., 2012).

The Neo-Hookean model describes the form of strain energy function as (Kumar, M., 2012):

$$W = C_{10} \cdot (\mathrm{I}_1 - 3) + \frac{1}{D_1} \cdot (\mathrm{J}_e - 1)^2 \tag{1}$$

where: C_{10} is the material constant which depends on the deformation of the material;

I_1 – first invariant of deformation tensor;

D_1 – material incompressibility parameter;

J_e – elastic volume ratio.

The two parameters C_{10}, D_1 are determined with the relationship (Jakel, R., 2010):

$$C_{10} = \frac{G}{2};\ D_1 = \frac{2}{K} \tag{2}$$

where: G is the initial shear modulus of material; K – bulk modulus, defined by:

$$K = \frac{E}{3 \cdot (1 - 2\nu)} = \frac{2G \cdot (1 + \nu)}{3 \cdot (1 - 2\nu)} \tag{3}$$

where: E is the elastic modulus of the material.

2.2. The Mooney-Rivlin model

The strain energy function developed by Mooney is (Kar Kamal, K., et *al*., 2007):

$$W = C_{10} \cdot (I_1 - 3) + C_{01} \cdot (I_2 - 3) + \frac{1}{D_1} \cdot (\mathrm{J}_e - 1)^2 \tag{4}$$

where: C_{01} is a material constant;

I_2 – the second invariant of deformation tensor.

The Mooney-Rivlin model can be defined by 2, 3, 5 or 9 parameters. The strain energy function for the Mooney-Rivlin model with two parameters is (Jakel, R., 2010):

$$C_{10} + C_{01} = \frac{G}{2} \tag{5}$$

Tensile strain up to 100% and compression strain up to 30% can be obtained with the Mooney-Rivlin model with two parameters.

The Mooney-Rivlin coefficients can be determined in several ways, namely (Gent, A. N., 2012):

- the elastomer hardness (H_A) is measured and the elastic modulus (E) and parameter C_{10} are calculated:

$$E = \frac{17.75 + 2.15 \cdot H_A}{100 - H_A}; C_{10} = \frac{E}{6} \tag{6}$$

- a shear test is carried out, the shear modulus is determined from the stress-strain curve and the parameter C_{10} is calculated, the parameter C_{01} is zero:

$$C_{10} = \frac{G}{2} \tag{7}$$

- if it is desired a value other than zero for C_{01}, it is chosen $C_{01} = 0.25 \cdot C_{10}$, resulting:

$$6 \cdot (C_{10} + C_{01}) = E \Rightarrow 6 \cdot (C_{10} + 0.25 \cdot C_{10}) = E \Rightarrow C_{10} = \frac{E}{7.5} \tag{8}$$

2.3. The Ogden model

The Ogden model has an unlimited number of parameters:

$$W = \sum_{i=1}^{N} \frac{\mu_i}{\alpha_i} \cdot (\bar{\lambda_1}^{\alpha_i} + \bar{\lambda_2}^{\alpha_i} + \bar{\lambda_3}^{\alpha_i} - 3) + \sum_{i=1}^{N} \frac{1}{D_i} \cdot (\mathrm{J}_{el} - 1)^{2i} \tag{9}$$

where: λ_p (p = 1,2,3) – the three principal stretches of material;

N, μ_i, α_i and D_i – material constants.

$$\sum_{i=1}^{N} \mu_i \cdot \alpha_i = 2\mu; \mu = G_0 \tag{10}$$

where: G_0 is the initial shear modulus of material.

For $N = 1$ and $\alpha_1 = 2$, the Ogden model is equivalent to the Neo-Hookean model. For $N = 2$, $\alpha_1 = 2$ and $\alpha_1 = -2$, the Ogden model is equivalent to the Mooney Rivlin model.

2.4. Parameter identification

The material constants and the parameters of hyperelastic models are determined from experimental tests based on the first load cycle.

The model parameters can be defined depending on the loads to which the elastomeric bearings is subjected (Fig. 3, 4), Eqs (12), (15):

a) Uniaxial compression:

The deformed shape of an elastomer under compression is presented in Fig. 2:

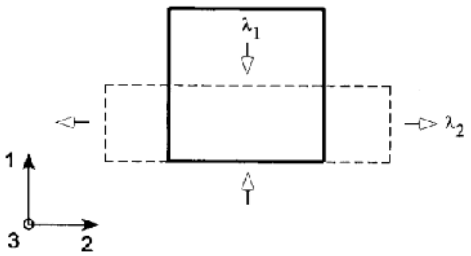

Figure 2. The elastomer deformation under compression (Amin, A.F.M.S., et *al*., 2006)

$$F = \begin{pmatrix} \lambda_1 & 0 & 0 \\ 0 & \sqrt{\frac{1}{\lambda_1}} & 0 \\ 0 & 0 & \sqrt{\frac{1}{\lambda_1}} \end{pmatrix}; B = \begin{pmatrix} \lambda_1^2 & 0 & 0 \\ 0 & \frac{1}{\lambda_1} & 0 \\ 0 & 0 & \frac{1}{\lambda_1} \end{pmatrix} \tag{11}$$

where: F is the deformation gradient tensor;

B – left Cauchy-Green deformation tensor.

$$I_1 = \lambda_1^2 + \frac{2}{\lambda_1}; I_2 = \frac{1}{\lambda_1^2} + 2\lambda_1; I_3 = 1 \tag{12}$$

$$\lambda_1 = \varepsilon_1 + 1 \tag{13}$$

where: ε_1 is the material strain.

b) Simple shear:

The deformed shape of an elastomer under shear is presented in Fig. 3:

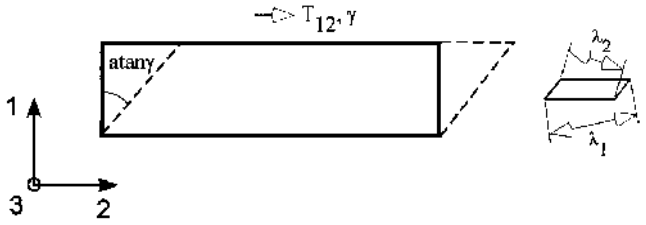

Figure 3. The elastomer deformation under shear (Amin, A.F.M.S., et *al*., 2006)

$$F = \begin{pmatrix} 1 & \gamma & 0 \\ 0 & 1 & 0 \\ 0 & 0 & 1 \end{pmatrix}; B = \begin{pmatrix} 1+\gamma^2 & \gamma & 0 \\ \gamma & 1 & 0 \\ 0 & 0 & 1 \end{pmatrix} \tag{14}$$

$$I_1 = I_2 = 3 + \gamma^2; I_3 = 1 \tag{15}$$

where: γ is the shear strain.

3. MODELING OF ELASTOMERIC BEARINGS

The shear modulus of elastomers is the most significant parameter in the design of bearings. The horizontal stiffness of the bearing, the restoring force and dynamic properties of isolation system depend on this parameter. The choice of material model depends on the problem to be analysed. The vertical stiffness of the bearing under load combinations is important for the design process and development of numerical models. (Gerhaher, U., et *al*., 2011).

The choice of finite element type heavily depends on the geometry and strain bearing material to obtain accurate numerical results.

The type of model for an elastomer can be selected in the finite element analysis program ANSYS from the hyperelastic materials library and experimental data are

inserted into the stress-strain curve values or the model parameters calculated from experimental tests are defined.

Reference parameters are defined in the computing program for the hyperelastic models, but it is indicated to introduce the model parameters depending on the mechanical characteristics of the elastomer in order to obtain accurate results.

The analysed elastomeric bearing consists of 6 elastomeric layers with thickness of 8 mm interspersed with metal plates of 3 mm thickness. The outer metal plates have a thickness of 8 mm. The shear modulus of the bearing is 0.9 MPa obtained from the shear test according to SR EN 1337-3.

The elastomeric bearing was modelled under compression, compression and shear with three hyperelastic models: Neo-Hookean, Mooney-Rivlin, Ogden. The model parameters introduced into the ANSYS program were:

- Neo-Hookean: $G_0 = 0.9$ MPa, $D_1 = 0.001$ MPa^{-1};
- Mooney-Rivlin: $C_{10} = 0.36$ MPa, $C_{01} = 0.09$ MPa, $D_1 = 0.001$ MPa^{-1};
- Ogden: $\mu_1 = 1.8$ MPa, $\alpha_1 = 1$, $D_1 = 0.001$ MPa^{-1}.

3.1. Compression

In the first case, a compression force was applied with a value of 7.5 kN. The results are shown in the Fig. 4.

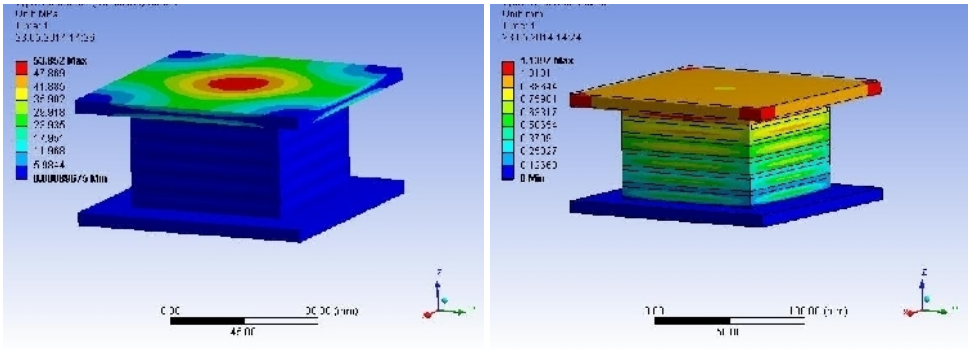

Figure 4. Equivalent stress and total deformation

3.2. Compression and shear

In the second case a vertical force of value 7.5 kN and a horizontal displacement of 34 mm (70% of elastomer height) were applied. The results are shown in the Fig. 5.

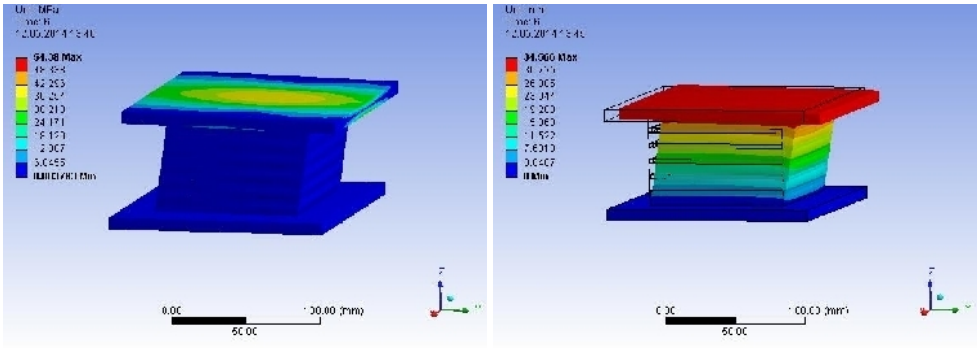

Figure 5. Equivalent stress and total deformation

The equivalent stress (von-Mises) resulted 53.8 MPa and a total deformation of 1.1 mm under compression, in all three cases, and the equivalent stress (von-Mises) resulted 54.3 MPa and a total deformation of 34.5 mm under compression with shear. Considering the fact that a strain of 30% was applied, the bearing could be modelled with those three models, but for larger deformations in Neo-Hookean model errors occur due to the strain range.

4. CONCLUSIONS

To analyse a material with hyperelastic models it is sufficient to know the parameters and to introduce them into a computer program.

There are many types of elastomers characterized by different mechanical properties and therefore the parameters of hyperelastic materials models are not given in the literature. In order to accurately define the parameters of strain energy function it is necessary to carry out experimental tests.

The finite element analysis of the elastomeric bearing was performed under compression and compression with shear. The Neo-Hookean, Mooney-Rivlin and Ogden models were used. In all cases, the results obtained were approximately equal.

The Neo-Hookean and Mooney-Rivlin models are easy to use but have limitations for large deformations of elastomers. Advanced models, such as Ogden, are indicated to obtain specific results for large deformations of these materials.

References

1. Amin, A.F.M.S., Wiraguna, S.I., Bhuiyan, A.R., Okui, Y., Hyperelasticity Model for Finite Element Analysis of Natural and High Damping Rubbers in Compression and Shear, *Journal of Engineering Mechanics*, vol. 132, 1, pp 54-64, 2006.
2. Bhashyam, G.R., *Ansys Mechanical - A Powerful Nonlinear Simulation Tool*, 2002.
3. Gent, A.N., *Engineering with Rubber: How to Design Rubber Components*, 3rd Edition, Carl Hanser Verlag GmbH, Munich, 2012.
4. Gerhaher, U., Strauss, A., Bergmeister, K., Numerical modeling of elastomeric bearings in structural engineering, *Advances in Materials Science*, *vol. 11*, 3 (29), pp 51-63, 2011.
5. Jakel, R., *Analysis of Hyperelastic Materials with Mechanica - Theory and Application Examples*, Presentation for the 2nd SAXSIM, 2010.
6. Kar Kamal, K., Sharma, S.D., Kumar, P., Ramkumar, J., Appaji, R.K., Reddy, K.R.N., Analysis of Rubber ressure Molding Technique to Fabricate Fiber Reinforced Plastic Components, *Polymer Composites*, *28*, pp 637-649, 2007.
7. Kim, B., Lee, S.B., Lee, J., Cho, S., Park, H., Yeom, S., Park, S.H., A Comparation Among Neo-Hookean Model, Mooney-Rivlin Model, and Ogden Model for Chloroprene Rubber, *International Journal of Precision Engineering and Manufacturing*, vol. 13, 5, pp 759-764, 2012.
8. Kumar, M., *Analysis of Elastomeric Bearings in Compression*, Departament of Civil Structural and Environmental Engineering, University at Buffalo, 2012.
9. SR EN 1337-3:2005, *Aparate de reazem pentru structuri, Partea 3: Aparate de reazem din elastomeri*, Asociația de Standardizare din România, București, 2005, (in Romanian).

Case Study on Shelter Proposal With and Without Dampers

Ioana Olteanu[1]
[1]*Structural Mechanics Department, Faculty of Civil Engineering and Building Services, Technical University "Gheorghe Asachi", Iaşi, 700050, Romania*

Summary

Major disasters from the last 10 years reveal the necessity to create more efficient temporary solution. Combining this necessity with the current trend in construction, with the use of light weight materials, or recycled materials lead to an innovative shelter solution.

The paper briefly presents the considered solution, emphasizing on the advantages to transform this temporary solution in a permanent one. Among the advantages of the proposed structure are: the light weight, adaptability in any climatic environment and possibility to build an assembly of more than two modules interconnected in different ways.

In order to prove the efficiency of the permanent solution, numerical simulations were performed in order to check the differences in two major situations – with and without dampers. Computational simulations in all loading cases have been performed according to European design codes, using FEM analysis - based programs.

The article proves that beside being an innovative alternative for the classic shelter solution in case of disaster, the project can be easily transformed into a permanent one, making it useful in worldwide, in any period of the year.

KEYWORDS: temporary shelter, damper, numerical simulation, polycarbonate.

1. INTRODUCTION

Natural hazards are unpredictable and damages caused can affect a neighborhood, a city, a region, a country. Until recovering measures can be adopted, temporary shelters can be used in order to host people whose houses were damaged. Temporary shelters have to be easy, resist, be reusable and offer a minimum comfort until the affected area is rebuilt or alternative measures are adopted.

One of the main goals of temporary shelters is to be adaptable to any context or location and to be independent of soil conditions. Also, after the reconstruction of

the affected area, the temporary structures should be easily to move to another disaster area or recycled.

Timber and steel are the main structural materials for building emergency shelters, but the execution time is quite high (1-2 days for structures in Figure 1).

Figure 1. Types of traditional shelter (courtesy of http://www.doubleharvest.org/where/haiti/housing, http://newseq.blogspot.ro/2011/05/poompuhar-safer-homes-post-tsunami.html)

Maintenance processes and costs have to be as low as possible in order to make the project a sustainable one. Even though traditional steel shelters can be made out of recycled materials, the structure cannot be re-used as a whole. Only some parts can be remodeled or used in other constructions.

The main disadvantage of traditional design of temporary dwellings is the loss of materials after their use. Even though recycling is possible, a great quantity of material can be deteriorated or destroyed. Also, if they were to be re-used completely, shelters have no architectural value, since they are designed to be as basic as possible.

Research in optimizing shelter design and functionality increased the choice for temporary houses. In this direction, figures 2 and 3 present some modern shelter structures available around the word.

Figure 2. Air shelters (courtesy of http://www.igreenspot.com/kahuna-the-perfect-shelter-for-post-disaster-situation/)

Figure 3. Other types of modern shelters (courtesy of http://www.tuvie.com/haven-rapid-deployment-temporary-shelter-system/, http://changeobserver.designobserver.com/feature/state-of-shelter/12527/)

2. INNOVATIVE SHELTER CONCEPT

An arch is an excellent choice in supporting long span structures due to their ability to reduce bending moments in the structure while carrying the load mainly in compression.

This is why the structural system for the proposed shelter is represented by a deployable arch, increasing building efficiency, making it easy to transport and to erect. The adaptable system enables numerous spatial layouts for hosting temporary or long-term events, being adaptable.

Based on the same principle as Lego bricks, the structure comes totally dismantled to the site, in order to facilitate transportation. Each modulated part will be connected to the others by simple, but strong and effective joints.

Aside from the temporary shelter function, the structure can be incorporated to other buildings, having also a permanent role, for example covering pedestrian bridges or providing cover on terrace roofs. In case this solution is adopted, special connections should be provided at the base of the arches.

Taking into account the weather conditions, the needed lighting intensity and the need to provide the proper humidity and temperature, the ideal material for the exterior insulation is considered - polycarbonate. The polycarbonate is a rigid, homogenous, chemically neutral material, with a fine cellular structure. It is a fireproof material of C class with molecular adherence. The material has good thermal conductivity 0.02-0.028 W/mK, high maximum service temperature (90-100ºC) and is waterproof.

The insulating polycarbonate shell will be pinned to the arched structure with simple connections. The holes where the connections will be made can be pre-drilled, in order to shorten the building process. A variety of colors can be used, giving the structure great architectural value and facilitating the integration of the structure in different landscapes, figure 4.

Figure 4. Innovative shelter layout

The deployable arched temporary shelter is made of slender steel arches, with polycarbonate coating, using efficiently the materials and considering the chemically neutral composition of the outer shell does not affect the ozone layer and is not carcinogenic. The structure can be considered an environmentally friendly one because of its properties.

3. INNOVATIVE SHELTER NUMERICAL SIMULATION

The arch span is of 7 m, height of 3.5 m and the modulus length is 6 m, Figure 4. These dimensions were carefully chosen. If a greater surface is needed, several modules can be assembled in order to get the desired result. The used materials are S235 steel for arches, purlins and bracings and polycarbonate for the covering. Steel provides excellent strength and can be easily assembled or dismantled in order to obtain the final structure.

The numerical simulation was performed in Axis VM 11 Academic Edition and Graitec. Both software are based on the finite element method (FEM) to obtain stresses in the structure elements.

For polycarbonate the following characteristics were considered: the modulus of elasticity $E_x=E_y=2300$ N/mm^2, the Poisson's coefficient of $\nu=0.2$ and the material density $\rho=1200$ kg/m^3.

Live loads were neglected. The numerical values for the loading were according to EuroCode 1. The considered snow load was of 2 kN/m^2 and wind pressure was 0.7 kN/m^2. The self weight of the structure has been taken automatically by the software.

For the earthquake scenario, coefficients according to the Romanian design code P100-1/2013 were considered: peak ground acceleration, $a_g=0.25g$; vibration period of control, $T_C=0.7$ s; behavior factor, q=2 and importance factor, $\gamma_I=1$.

Several load combinations were considered in accordance with CR0 code in order to reveal the most unfavorable scenarios and ensure that the structure will behave as expected.

Modal and static analyses were performed in both software environments. Table 1 shows the result from the modal analysis, where *f* is the natural frequency, *T* the period of vibration and ω is the angular frequency. It can be noticed that the results for the fundamental vibration mode are similar in both analyses.

Table 1 - Modal analysis results

	Graitec			**AxisVM**		
	f (Hz)	**T (s)**	**ω (rad/s)**	**f (Hz)**	**T (s)**	**ω (rad/s)**
1	2.25	0.44	14.12	2.34	0.428	14.69
2	5.32	0.19	33.42	4.03	0.248	25.34
3	9.03	0.11	56.76	4.08	0.245	25.63
4	10.04	0.10	63.10	5.02	0.199	31.55
5	10.21	0.10	64.16	5.17	0.193	32.47

A linear static analysis was performed in order to check the chosen cross section of the elements. The internal forces obtained through a linear static analysis are presented in Figure 5. It can be noticed that the results are similar. If the stresses and strength are compared for the Ultimate Limit State, the following results are obtained: the maximum principal tensile stress by seismic combination, 7.66 N/mm^2, is significantly smaller than the tensile strength of the polycarbonate membrane, 63 N/mm^2. In terms of compression, the maximum compression stress by fundamental combination is 5.83 N/mm^2, less than 78 N/mm^2 that is the compressive strength of the polycarbonate membrane.

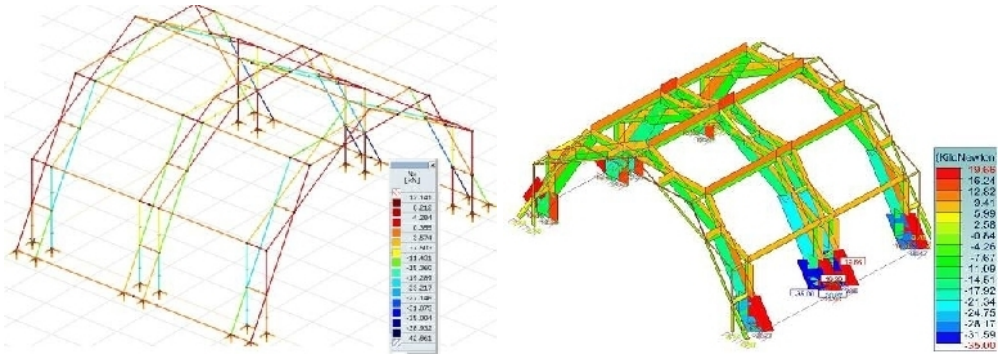

Figure 5. Results for axial internal effort in Axis and Graitech

In terms of maximum displacements the results were also within the maximum allowable limits. For the vertical displacements a 15 mm displacement was obtained which is less than 40 mm, meanwhile for the maximum horizontal displacement a 13 mm displacement resulted, less than the maximum allowable horizontal displacement which is 20 mm.

In order to enhance the behavior of the structure, especially in case of permanent house, the use of dampers at the foundation level was proposed, Figure 6. The fundamental period increased from 0.428 s to 1.77 s and also the strains in the elements decreased due to the dampers introduction.

Figure 6. Base isolating system

Due to the low cost and efficient use of materials, the total cost has been reduced, offering the possibility to buy the adaptable structure for a low price. Given the fact that polycarbonate is a relatively cheap material (up to 30$/square meter for larger quantities) and that the needed steel quantity is low, the cost of a module is estimated to be around 4500$.

4. CONCLUSIONS

The main goal of this project was fast mitigation strategies in case of natural disasters. The importance of temporary shelters for humanitarian help has become higher and higher. Thus, the proposed project is easy to erect in a very short time, has a good deploying ratio and is cost-effective.

The originality of the project is sustained by several elements. First of all, the use of kinetic arches proves that scissor like elements could be used, at a larger scale, in the future as reliable structural parts. Also, the use of polycarbonate is an innovative way of creating a great quality indoor space, from both technical and architectural point of view. Last, but not least, re-using the structure is one of the aims of this project, having temporary structures incorporated further on to permanent buildings.

The importance of base isolating system is obvious for horizontal loading and in the case the shelter becames a permanent building. The structure is an environmentally friendly one bringing architectural value to any location where a temporary shelter is needed, and not only.

References:

1. *Transitional shelters. Eight designs.* International Federation of Red Cross and Red Crescent Societies http://www.sheltercentre.org/sites/default/files/900300-transitional_shelters-eight_designs-en-lr.pdf, 2011.
2. EUROCODE 1 - EN 1991, parts 1-3, 1-4.
3. P100-1/2006 - The Romanian Standard For Design Of Structures For Earthquake Resistance.
4. C107/1-3/2005 - Romanian standard for the calculus of the global thermal insulation coefficients for the civil residences.
5. Maden F., Korkmaz K., Akgün Y. A review of planar scissor structural mechanisms: geometric principles and design methods, *Architectural Science Review*, Vol 54, Issue 3, 2011.
6. http://www.gplastics.com/pdf/polycarbonate.pdf.
7. Yenal Akgün, A novel transformation model for deployable scissor-hinge structures, *PhD Thesis*, TU Stuttgart, Germany, 2010.
8. *Emergency Family Shelter System* developed by Cambridge University in collaboration with Oxfam's Emergencies Department, http://www.shelterproject.org/downloads/tom2.pdf.
9. Igor Raskin, Strength and Stiffness of Deployable Pantographic Columns, *PhD Thesis*, Waterloo, Ontario, Canada, 1998.
10. Gantes C., Connor J.J., Logcher R.D., Combining Numerical Analysis and Engineering Judgement to Design Deployable Structures, *Computer & Structures*, Vol 40, No 2, pp 431-440, 1991.
11. http://www.designbuzz.com/small-shelter-offers-instant-refuge-during-emergencies/
12. http://changeobserver.designobserver.com/feature/state-of-shelter/12527/
13. http://www.tuvie.com/haven-rapid-deployment-temporary-shelter-system/
14. http://www.igreenspot.com/kahuna-the-perfect-shelter-for-post-disaster-situation/
15. http://www.archiexpo.com/prod/polypiu-plast/curved-polycarbonate-sheets-71669-841504.html.

Evaluation of the Dynamic Structural Characteristics

Octavian Victor Roşca[1], Eduardo D. Caracciolo[2]
[1]*Structural Mechanics Department, Technical University"Gh. Asachi", Iaşi, 700241, Romania*
[2]*Ricerca Sistema Energetica S.P.A., Milano, Italy*

Summary

In the structural analysis there are situations when the eigenvalues and eigenvectors of non- symmetric matrices are requested, even of the complex matrices. Non- proportional damped structures are a part of these systems. The hypothesis of proportional damping is advantageous from the numerical point of view and the experimental tests show that this approximation leads in most cases to acceptable results. However it is not demonstrated yet the proportional behavior of the damping.

This paperwork deals with the numerical problem of the complex eigen values. A structural case study of a 3 storey frame tested on the master shaking table of the Laboratory of Earthquake Engineering from the Structural Mechanics Department of the Faculty of Civil Engineering and Building Services from Iaşi it is presented.

The analysis conducted to the complex eigenvalues and modal shapes of vibration.

In the end the conclusions of the analysis and the computational effort are depicted.

KEYWORDS: structural analysis, modal analysis, complex eigenvalues.

1. INTRODUCTION

This paperwork deals with the problem of the natural modes vibration for civil engineering structures. The natural frequencies are squared and correspond to the eigenvalues of the generalized problem of M, the mass matrix and K, the stiffness matrix. The natural deflected shapes correspond to the eigenvectors of the same problem. A case study of a 3 storey frame tested on the master shaking table of the Laboratory of Earthquake Engineering from the Structural Mechanics Department of the Faculty of Civil Engineering and Building Services from Iaşi it is presented.

2. THEORETICAL BACKGROUND

Most of the engineering problems in vibrations are leading to the eigen value problem, in the simple or generalized format. It is commonly accepted and convenient to use the real eigenvalues; therefore the matrices of the dynamic system are symmetric and positive defined. In the case of the time history analysis the equations of motion are decoupled, based on the assumption that the damping is proportional (Rayleigh type) to the mass or stiffness or both. The damping matrix C is then written as a linear combination of M and K ($C = \alpha M + \beta K$). Under these circumstances the time responses obtained separately can be superimposed using the modal participations.

In the structural analysis there are situations when the eigenvalues and eigenvectors of non- symmetric matrices are requested, even of the complex matrices. Non-proportional damped structures are a part of these systems. The hypothesis of proportional damping is advantageous from the numerical point of view and the experimental tests show that this approximation leads in most cases to acceptable results. However it is not demonstrated yet the proportional behavior of the damping.

Let us consider the solution of the NDOFs dynamic system in the linear vibration:

$$M\ \ddot{X} + C\ \dot{X} + K\ X = 0\,. \tag{1}$$

The solution can be written in the vector form:

$$x = q\ e^{st}\ . \tag{2}$$

The substitution of (2) in (1) leads to the equation:

$$\left(s^2\,M + s\,C + K\right)q = 0 \tag{3}$$

that has to be provided with the zero determinant in order to obtain a non- trivial solution

$$\det\left(s^2\,M + s\,C + K\right) = 0\,. \tag{4}$$

The characteristic eq. (4) is also known as the quadratic form of the eigen value problem. The solution leads to "2 N" eigenvalues and the corresponding "2 N" eigen vectors (with N components). The general solution of the motion is obtained after the modal superposition of the 2 N solutions:

$$x = \sum_{i=1}^{2N} \xi_i\, q_i\, e^{\,s_i t} \tag{5}$$

where ξ_i are arbitrary constants that are find out from the initial coditions. The eigen values are obtained as complex conjugated pairs $s^m = \mu_m + i\,\nu_m$ şi $s^*m = \mu_m - i\,\nu_m$ and the corresponding eigen vectors are written as $q_m = a_m + i\,b_m$ şi $q^*m = a_m - i\,b_m$. The sollution that corresponds to the "m" DDOF is written:

$$x_m(t) = \left(c_m + i\,d_m\right)e^{\left(\mu_m + i\,\upsilon_m\right)t}\left(a_m + i\,b_m\right) + \left(c_m - i\,d_m\right)e^{\left(\mu_m - i\,\upsilon_m\right)t}\left(a_m - i\,b_m\right) \tag{6}$$

wher c_m and d_m are arbitrary constants. In order to obtain a damped oscillation in time it must that

$$\mu_m < 0\,. \tag{7}$$

If all the roots of the eigen value problem are complex conjugated, then there will be N solutions of the type and the total response shall be provided by:

$$x = \sum_{m=1}^{N} x_m\,. \tag{8}$$

The eq. (6) can also be expressed in tthe exponent form:

$$x_m(t) = e^{\mu_m\, t}\left(v_m \sin \upsilon_m t + w_m \cos \upsilon_m t\right) \tag{9}$$

where:

$$v_m = -2\left(d_m a_m + c_m b_m\right) \tag{10.a}$$

$$w_m = 2\left(c_m a_m - d_m b_m\right) \tag{10.b}$$

and c_m şi d_m are arbitrary constants that are calculated from the "2 N" initial conditions. The final solution is of real type. The quadratic eigen value can be transformed into a linear or standard problem. The transformation to the generalized (linear) form is presented.

A displacement and velocity vector will be assembled, in a similar manner as that used in the state-space:

$$\mathrm{z} = \begin{bmatrix} \dot{\mathrm{x}} \\ \mathrm{x} \end{bmatrix} \tag{11}$$

and the equations of motion are written as:

$$\begin{cases} M\,\dot{x} - M\,\dot{x} = 0 \\ M\,\ddot{x} + C\,\dot{x} + K\,x = 0 \end{cases}. \tag{12}$$

The above system is written in matrix format:

$$\begin{bmatrix} 0 & \mathrm{M} \\ \mathrm{M} & \mathrm{C} \end{bmatrix} \begin{bmatrix} \ddot{\mathrm{x}} \\ \dot{\mathrm{x}} \end{bmatrix} + \begin{bmatrix} -\mathrm{M} & 0 \\ 0 & \mathrm{K} \end{bmatrix} \begin{bmatrix} \dot{\mathrm{x}} \\ \mathrm{x} \end{bmatrix} = \begin{bmatrix} 0 \\ 0 \end{bmatrix} \tag{13}$$

and leads to

$$A\,\dot{z} = B\,z\,. \tag{14}$$

The system matrices A and B are:

$$\mathrm{A} = \begin{bmatrix} 0 & -\mathrm{M} \\ -\mathrm{M} & -\mathrm{C} \end{bmatrix} \tag{15}$$

and

$$B = \begin{bmatrix} -M & 0 \\ 0 & K \end{bmatrix}. \tag{16}$$

It is selected a soution of the form $\mathrm{z} = \mathrm{v}\, \mathrm{e}^{\mathrm{s\,t}}$. The replacement in (14) leads to the generalized eigenvalue problem:

$$B\,v = s\,A\,v\,. \tag{17}$$

Just like in the case of undamped vibrations, the $\mathrm{v_i}$ vectors are orthogonal with respect A and B:

$$\mathrm{v_i^T A\, v_j} = 0 \quad , \quad \mathrm{s_i} \neq \mathrm{s_j} \tag{18.a}$$

$$v_i^T B\, v_j = 0 \quad , \quad s_i \neq s_j\,. \tag{18.b}$$

The $\mathrm{v_i}$ vectors and are normalized over the A matrix, thus leading to:

$$v_m^T A\, v_m = 1 \quad , \quad m = 1, 2, \ldots, 2\,N\,. \tag{19}$$

If we define the modal matrix V and the spectral matrix S of the 2 N eigen vectors v, like in the case of the standard eigen problem, we obtain:

$$\mathrm{V^T\, A\, V = I} \tag{20}$$

$$\mathrm{V^T\, B\, V = S}\cdot \tag{21}$$

The shift from the generalized problem to the standard one is performed by pre-product of B^{-1},

$$B^{-1} A v = \frac{1}{s} v \tag{22}$$

thus leading to:

$$D v = \gamma v . \tag{23}$$

wher $D = B^{-1} A$ and $\gamma = 1 / s$. The D is the dynamic matrix and is defined thereby:

$$D = \begin{bmatrix} 0 & I \\ -K^{-1} M & -K^{-1} C \end{bmatrix} \tag{24}$$

where K-1· M is the dynamic matrix in the case of the free undamped vibrations.

3. CASE STUDY

It is considered the modal analysis of a 3 storey steel frame as presented in the Figure no.1. For the dynamic model 3 translational DOFs are granted along the OX and OY orthogonal directions in plane, according to the governing directions of the shaking table.

Figure 1. General view of the shaking table and the specimen

The 3 storey steel frame model with additional weights has a geometrical scale of 1/4.

The columns are made of I80 Romanian steel profiles. The beams and joint assemblages at each storey level assure a rigid plate behavior "in plane". The physical model acts merely as a consequence of the column bending effect.

The span on OX is of 1.40 m and the bay on OY is of 1.20m. Each storey height is of 1.10m. In the figure no. 2 there are depicted some details of the instrumentation that was applied on the test frame.
The mass matrix is considered diagonal, with equal uncoupled masses at each level:

$$M = \begin{bmatrix} 300 & 0 & 0 \\ 0 & 300 & 0 \\ 0 & 0 & 300 \end{bmatrix} [kg]. \tag{25}$$

Figure 2. Instrumentation at the base plate level

The stiffness matrix was evaluated analytically and by the means of some software to be:

$$K = \begin{bmatrix} 1.501x10^3 & -267.189 & -178.14 \\ -267.189 & 594.494 & -315.355 \\ -178.14 & -315.355 & 468.635 \end{bmatrix} [KN/m]. \tag{26}$$

4. THE ANALYSIS RESULTS

The first testing phase consisted of the low level sweep sine tests (OX & OY directions). After the sweep there were obtained the frequencies of the real model on the shaking table as given in the Table 1.

Table 1. Modal quantities (experimental)

Natural mode of vibration	Frequency (Hz)	Modal shapes (normalized)		
1	3.8	0.0128	0.0319	0.0447
2	8.2	0.0361	0.0293	-0.0317
3	11.7	-0.0410	0.0357	-0.0319

After the scanning of the frequencies the model was subjected to sine motions in order to check out the modal behavior i.e. real mode shapes and the damping characteristics. Natural frequencies were applied at different amplitudes and input energies. In the next figure we depict an example of the measurements when the motion was applied with f1 = 3,8 Hz.

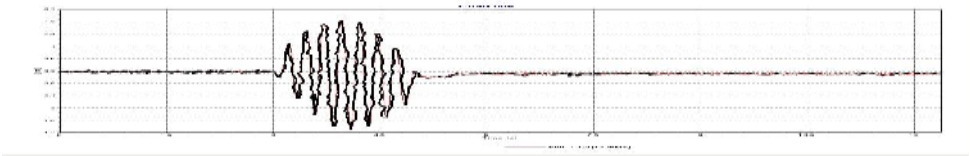

Absolute displacement at the base plate level (shaking table motion OX direction)

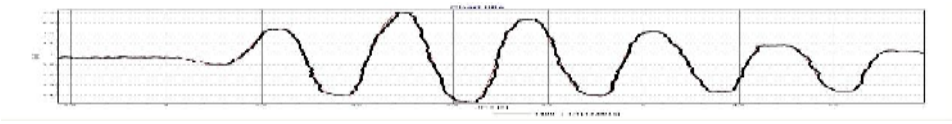

displacement at the first floor level (OX)

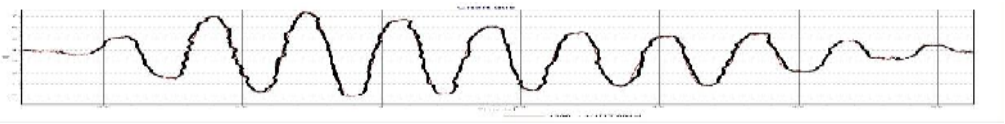

displacement at the second floor level (OX)

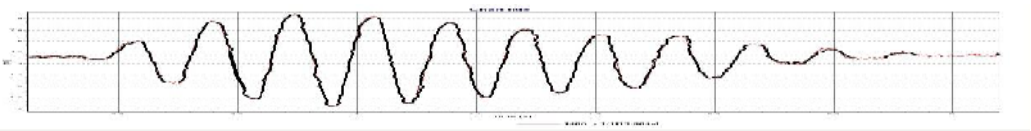

displacement at the 3rd floor level (OX)

Figure 3. Sine motion along OX direction -displacement control

Even the logarithmic decrements were almost simple to evaluate, the selection of the appropriate method to calculate them leaded to a sensitive selection. Then several difficulties arise in the estimation of the damping matrix.

The testing program continued with earthquake type excitations at several degrees of intensity. There were used the "Bucureşti 1986" and the "Vrancea 1986 - Focsani" accelerograms at several PGAs up to 0.6g. The significant earthquake duration was about 30 seconds.

Several computer dedicated programs were used to advocate the analytical models. Taking into account this simple geometry no significant differences occured, no matter what software was used. In the following we present a model realized with the SAP 2000 computer program which provided also the input for the analysis with the FEMtools software.The computed natural frequencies, for instance, look a little bit far from the experimental frequencies.

The model validation was carried on by the means of the FEM Tools software, which is a multi-functional, cross-platform and solver- independent CAE software suite used for the structural dynamics simulation, model validation, validation and updating.

The parameter validation included the spectral matrix and some material properties (i.e. Young modulus and Posion's ratio). The correlation was achieved mainly on the basis of the MAC (Modal Assurance Criterion) that is the correlation vector between the analytical and experimental mode shapes. The MAC matrix is depicted in the figure No. 4.

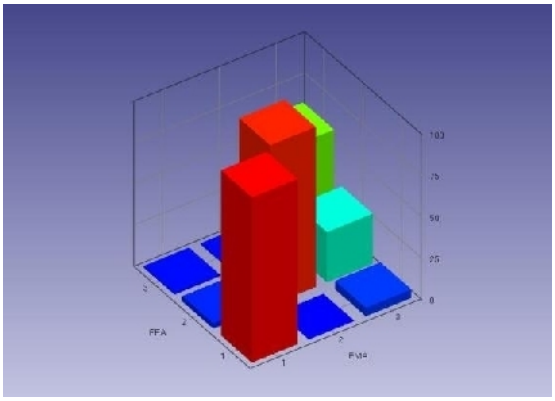

Figure 4. Model validation - MAC criterion

After the FEM updating the new modal quantities are those from the Table no. 2.

Table 2. Modal Quantities (Numerical, after the model updating)

Natural mode of vibration	Frequency - tests (Hz)	Frequency - model (Hz)
1	3.8	3.439
2	8.2	8.433
3	11.7	11.558

The modal analysis in the field of real eigenvalues was performed by taking into account an assumed stiffness proportional damping (i.e. C = β K, β = 0.01 (1%)).

The test measurements of the logarithmic decays of damping leaded to non-proportional values between the mass matrix and stiffness matrix coefficients.

After applying the complex eigen value process described in the previous chapter one obtains the complex spectral matrix:

$$\Lambda_{np} = \begin{bmatrix} -2.5801 + 21.4608i & 0 & 0 & 0 & 0 & 0 \\ 0 & --2.5801 - 21.4608i & 0 & 0 & 0 & 0 \\ 0 & 0 & -14.1022 + 51.0875i & 0 & 0 & 0 \\ 0 & 0 & 0 & -14.1022 - 51.0875i & 0 & 0 \\ 0 & 0 & 0 & 0 & -31.0565 + 65.5804i & 0 \\ 0 & 0 & 0 & 0 & 0 & -31.0565 - 65.5804i \end{bmatrix} \quad (27)$$

After sorting descending the diagonal elements and the computation of their modulus, one obtains the circular frequency vector:

$$\omega_{np} = \begin{bmatrix} 21.6153 \\ 21.6153 \\ 52.9982 \\ 52.9982 \\ 72.5624 \\ 72.5624 \end{bmatrix} \text{[rad/s]} . \quad (28)$$

The complex modal matrix is:

$$V_{np} = \begin{bmatrix} -0.0017 - 0.0101i & -0.0017 + 0.0101i & -0.0009 - 0.0018i & -0.0009 + 0.0018i & 0.0057 + 0.0121i & 0.0057 - 0.0121i \\ -0.0036 - 0.0294i & -0.0036 + 0.0294i & -0.0037 - 0.0134i & -0.0037 + 0.0134i & -0.0017 - 0.0024i & -0.0017 + 0.0024i \\ -0.0041 - 0.0337i & -0.0041 + 0.0337i & 0.0036 + 0.0121i & 0.0036 - 0.0121i & -0.0006 - 0.0011i & -0.0006 + 0.0011i \\ 0.2204 - 0.0102i & 0.2204 + 0.0102i & 0.1059 - 0.0198i & 0.1059 + 0.0198i & -0.9722 & -0.9722 \\ 0.6400 - 0.0016i & 0.6400 + 0.0016i & 0.7349 & 0.7349 & 0.2122 - 0.0400i & 0.2122 + 0.0400i \\ 0.7346 & 0.7346 & -0.6692 + 0.0126i & -0.6692 - 0.0126i & 0.0893 - 0.0049i & 0.0893 + 0.0049i \end{bmatrix} . \quad (29)$$

The above matrix is computed for the standard problem of 2N order, $D_{np}\ v_{np} = \gamma_{np}\ v_{np}$ and the eigen vectors are transformed for the real system with N GLD. The complex shapes of vibration are:

$$X_{np} = \begin{bmatrix} 0.3020 + 0.0000i & 0.3020 - 0.0000i & 0.1571 + 0.0000i & 0.1571 - 0.0000i & 1.0000 & 1.0000 \\ 0.8714 + 0.0000i & 0.8714 - 0.0000i & 1.0000 & 1.0000 & -0.2413 + 0.0000i & -0.2413 - 0.0000i \\ 1.0000 & 1.0000 & -0.9189 + 0.0000i & -0.9189 - 0.0000i & -0.0917 + 0.0000i & -0.0917 - 0.0000i \\ 0.3000 - 0.0139i & 0.3000 + 0.0139i & 0.1442 - 0.0269i & 0.1442 + 0.0269i & 1.0000 - 0.0000i & 1.0000 + 0.0000i \\ 0.8711 - 0.0021i & 0.8711 + 0.0021i & 1.0000 & 1.0000 & -0.2182 + 0.0411i & -0.2182 - 0.0411i \\ 1.0000 + 0.0000i & 1.0000 - 0.0000i & -0.9106 + 0.0171i & -0.9106 - 0.0171i & -0.0919 + 0.0050i & -0.0919 - 0.0050i \end{bmatrix} . \quad (30)$$

The complex modal shape of the first mode of vibration is depicted in the complex space in the Figure No. 5.

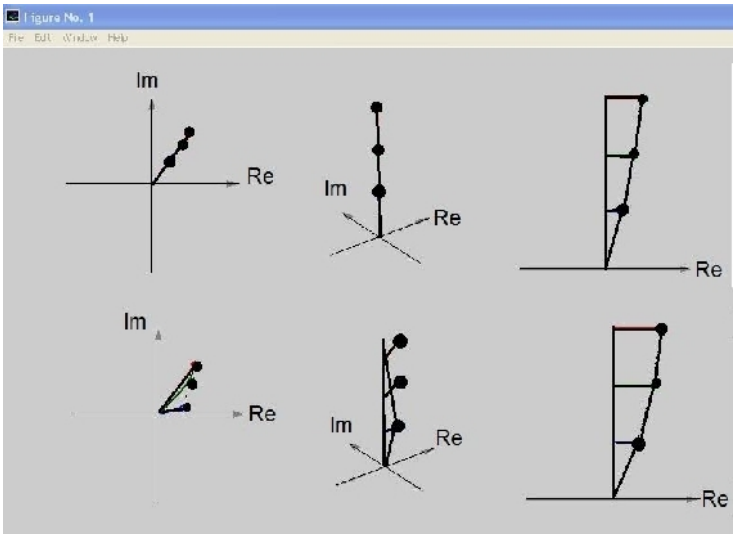

Figure 5. The complex modal shapes of vibration

5. CONCLUSIONS

This paperwork deals with the problem of the natural modes vibration for civil engineering structures. The natural frequencies are squared and correspond to the eigenvalues of the generalized problem of M, the mass matrix and K, the stiffness matrix. The natural deflected shapes correspond to the eigenvectors of the same problem. A case study of a 3 storey frame tested on the master shaking table of the Laboratory of Earthquake Engineering from the Structural Mechanics Department of the Faculty of Civil Engineering and Building Services from Iaşi it is presented. The 3 storey steel frame model with additional weights has a geometrical scale of 1/4.

The modal analysis was carried out in the first step after assuming a proportional damping, merely "stiffness" type. Next, after measurement regarding the logarithmic decays of damping a non- proportional damping was assumed. The solution of an eigen value problem consumes N3 operations (3rd order problem). The quadratic problem requires the solution of a 2N order system and it follows that the number of operations is 8 times bigger. In the case of a large eigen value problem, the performance of the solver is dramatically decreased. Under these circumstances, a ballance between the costs and the Rayleigh assumption might be useful, thus leading to good results, but not necessarily exact.

References

1. J. L. Humar, *Dynamics of Structures*, Prentice-Hall, N.J., 1990.
2. K. J. Bathe, Edward L. Wilson, *Numerical Methods in Finite Element Analysis*, Prentice-Hall Inc., Englewood Cliffs, New Jersey, 1976.
3. K.J. Bathe, *Finite Element Procedures in Engineering Analysis*, Prentice-Hall Inc., Englewood Cliffs, New Jersey, 1982.
4. J. H. Wilkinson, C. Reinsch, Linear Algebra, vol. II of *Handbook for Automatic Computation*, Springer Velrag New York, 1971.
5. J. H. Wilkinson, *The Algebraic Eigenvalue Problem*, Clarendon Press, Oxford, 1978.
6. P. Hood, "Frontal Solution Program for Unsymmetric Matrices", *Int. J. Num. Meth. Engng*, 10, 379-399, (1976).
7. K. J. Bathe, EE. Wilson, "Large Eigenvalue Problems in Dynamic Analysis", *J. Engng. Mech Div*., ASME, 1972, 98, pp.1471-1485.
8. A. Perdon, G. Gambolati, "Extreme Eigenvalues of Large Sparse Symmetic Matrices by Rayleigh Quotient and Modified Conjugate Gradients", *Comput. Meth. Appl. Mech. Engng.*, 1986, 56, 251-254.
9. X. Wang, J. Zhou, "An Accelerated Subspace iteration Method for Generalized Eigenproblems" *Comps. & Struct.*, 1999, 71, pp. 293-301.
10. Octavian V. Roşca, Ioan P. Ciongradi, *Metode numerice utilizate în programele de calcul automat al structurilor* Ed. Acad. Society "Matei-Teiu Botez", Iaşi, 2003.
11. M. Friswell J.E. Mottershead, *Finite Element Model Updating in Structural Dynamics*, Kluwer Academic Publisher, 1995.
12. E. Dascotte, J. Strobbe, U.T. Tygesen, Continuous stress monitoring of large structures, *IOMAC 2013 5th International Operational Modal Analysis Conference*, 2013 May 13-15 Guimarães - Portugal.
13. Dascotte, E. (2007) Model Updating for Structural Dynamics: Past, Present and Future Outlook. *Proc. Int. Conference on Engineering Dynamics* (ICED 2007), Carvoeiro, Algarve, Portugal.

Probabilistic Seismic Risk Assessment of Lorca, Spain

Mario A. Salgado-Gálvez[1], Martha L. Carreño[1,2], Alex H. Barbat[1,2], Omar Darío Cardona A.[3]

[1]*Centro Internacional de Métodos Numéricos en Ingeniería, CIMNE, Barcelona, 08034, Spain*
[2]*Departamento RMEE, Universitat Politècnica de Catalunya, Barcelona, 08034, Spain*
[3]*IDEA, Universidad Nacional de Colombia, Manizales, 170004, Colombia*

Summary

A fully probabilistic risk assessment has been conducted for the building portfolio (both public and private) in Lorca, Spain. The city was heavily affected by the earthquake occurred in May 2011 and several damage surveys were conducted after that event. Exposed assets information is of high quality in Lorca and a building by building resolution level database is available. Making use of that information a comparison of the recorded damage levels against modelled losses was performed and after concluding that the estimations lie within acceptable orders of magnitude, a fully probabilistic risk assessment was performed. Risk results are obtained in terms of the loss exceedance curve from where other relevant risk metrics such as the average annual loss and probable maximum losses can be derived. Since risk has been calculated using a geocoded database, risk maps in terms of absolute and relative average annual losses were obtained for Lorca.

KEYWORDS: seismic hazard, probabilistic risk assessment, loss exceedance curve, risk maps.

Computational Civil Engineering - CCE 2014
International Symposium, Iaşi, Romania, May 24, 2014
ISSN 2285 - 2735, Pages 146 - 163

1. INTRODUCTION

Even low to moderate magnitude earthquakes can generate important losses as observed during the Lorca earthquake on May 11th 2011, when a 5.1 magnitude event stroke the city causing important casualties, damages and service disruptions. From the earthquake engineering perspective, disasters constitute interesting case studies since, given that communities that perceive seismic hazard as low, usually have exposed assets with high vulnerability levels, aggravating the potential damages and losses, which is the physical risk, when an earthquake strikes the area of interest.

Lorca, a city located in the Murcia region, south-eastern Spain has almost 60,000 inhabitants and was one of the most affected areas due to the 2011 earthquake given that the epicenter was located just 5km north of the city and besides that, it was very shallow.

A probabilistic and spectral hazard assessment was conducted for the Iberian Peninsula using the most updated information in terms of tectonic zonation, earthquake catalogue and ground motion prediction equations from where a set with 50,982 stochastic scenarios was derived. Those scenarios were later used in the computation of the expected damages on all the elements included in the exposed assets database.

The city has a cadastral database that allows identifying and characterizing the building stock on element by element basis, which corresponds to the highest possible resolution level for probabilistic risk assessment purposes. The available information allowed the assignation of parameters such as age, number of stories, building class and replacement value among others.
A unique seismic vulnerability function was assigned to each identified building class to account for the direct physical losses which are the ones intended to be quantified on this study.

Several tools are available to perform a seismic risk assessment in probabilistic metrics. We selected the CAPRA[1] platform (ERN-AL 2010; Cardona et al. 2010, 2012; Salgado et al. 2013; 2014; Marulanda et al. 2013) which consists of different modules enabling the evaluation of the seismic hazard, earthquake vulnerability and seismic risk. The Lorca case constitutes an opportunity and a challenge to understand the strengths and weaknesses of the probabilistic seismic risk evaluation approach, highlighting the improvements required regarding exposure input data as well as for hazard, vulnerability and risk assessment. The convolution

[1] Comprehensive Approach to Probabilistic Risk Assessment

between the hazard and the vulnerability provided the expected losses, obtained in terms of the loss exceedance curve from where other relevant risk metrics such as the average annual loss and probable maximum loss can be derived. The second order effects, such as business disruption, damage to cars and other indirect damage and the socio-economic impact, were not included in the estimation.

2. PROBABILISTIC SEISMIC HAZARD ASSESSMENT

2.1 Bedrock level

The probabilistic risk assessment methodology that is applied in this study requires an exhaustive set of stochastic scenarios that characterize, in a comprehensive way, the seismic hazard in Lorca. To represent the seismic hazard in this way, the best approach was to conduct a probabilistic and spectral seismic hazard analysis in the Iberian Peninsula and its neighbouring regions. Accordingly, a seismic hazard assessment is performed considering different seismogenetic sources that were characterized by a Gutenberg-Richter (G-R) (1944) model. The employed tectonic zonation corresponds to the one proposed in the framework of the SHARE project (GRCG 2010) where 51 seismogenetic sources were defined. An additional source was located in northern Africa to account for the seismicity occurring in that area which may affect the Peninsula. Figure 1 presents this zonation.

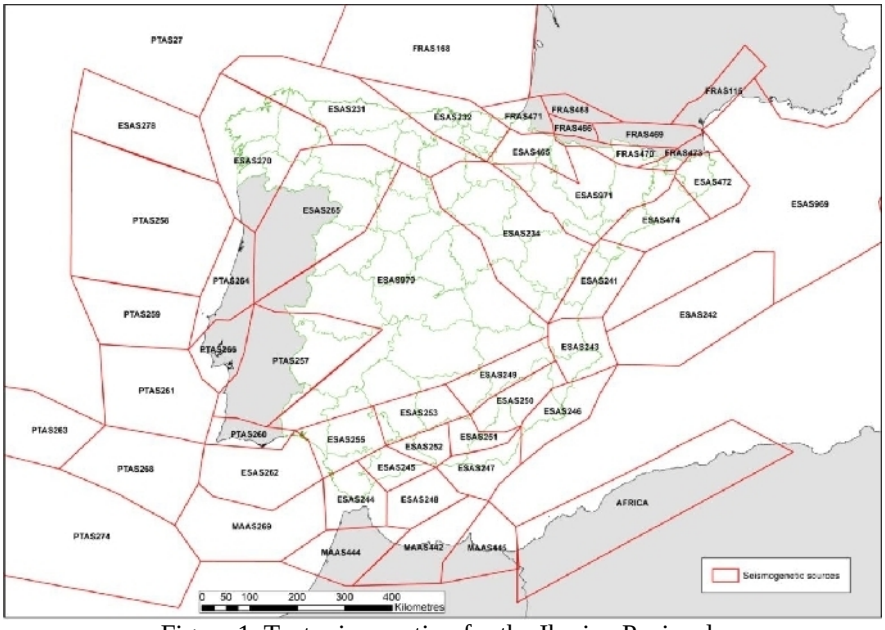

Figure 1. Tectonic zonation for the Iberian Peninsula

Since the occurrence of earthquakes over the time cannot be predicted, and a complete time window is an unknown quantity, a set of 1,991 stochastic events was generated. To characterize the seismicity occurrence process at each source, a Poisson model was selected. Seismic activity is determined based on the magnitude recurrence rates, relating the frequencies with which earthquakes with a given magnitude occur at each seismogenetic source. Seismicity is defined by Equation 1 which corresponds to a modified version of the G-R model (Cornell and Van Marke 1969).

$$\lambda(M) = \lambda_0 \frac{e^{-\beta M} - e^{-\beta M_U}}{e^{-\beta M_0} - e^{-\beta M_U}}, M_0 \leq M \leq M_U \quad (1)$$

where $\lambda(M)$ is the recurrence frequency for events with magnitude equal or higher to the selected threshold; λ_0, β y M_U are the seismicity parameters of each seismogenetic source and M is the general random variable that represents the magnitude for each source. λ_0 describes the annual occurrence rate of events with magnitude equal or higher than the selected threshold, which was set equal to 3.5 for all sources in this study; β represents the initial slope of the logarithmic regression and M_U the maximum magnitude associated to each seismogenetic source, which is the largest magnitude expected to occur at each seismogenetic source. The seismic catalogue employed corresponds to the one published by the Spanish National Geological Institute (IGN 2013a) where a completeness verification for the selected threshold magnitude, following the approach proposed by Tinti and Mulargia (1985) was done. The λ_0 and β parameters were calculated using the maximum likelihood method (McGuire 2004) while the assigned M_U values correspond to those published in the SHARE project (GRCG 2010). Historically, several earthquakes have stroke the region such as the ones occurred in March 1911, January 1917, June 1948, August 2002 and January 2005 (Benito et al. 2012), but only the one that occurred in May 2011 caused important damage, casualties, injuries and disruption.

European calibrated ground motion prediction equations (Ambraseys et al. 2005) were assigned to the seismogenetic sources according to their tectonic environment, and then the seismic hazard assessment was conducted by integrating the contribution of each source considering its distance to the point of interest. Intensity exceedance rates were obtained for several spectral ordinates and with them, uniform hazard spectra (UHS) can be obtained. The seismic hazard calculation was performed using CRISIS 2007 V7.6 (Ordaz et al. 2007) which is the seismic hazard module of the CAPRA platform. Figure 2 shows the UHS at bedrock level in Lorca for 200, 500 and 1,500 years return period. Peak ground acceleration (PGA) for 10% exceedance probability in 50 years is estimated at 0.17g, compared to the 0.19g established in the latest national seismic hazard analysis (INE 2013b) and to the 0.12g in the Spanish building code NSCE (NSCE

2002) for the city. This result takes into account the contribution of all seismogenetic sources considered in the model whose distances are within the integration ratio, equal to 300 km for this study.

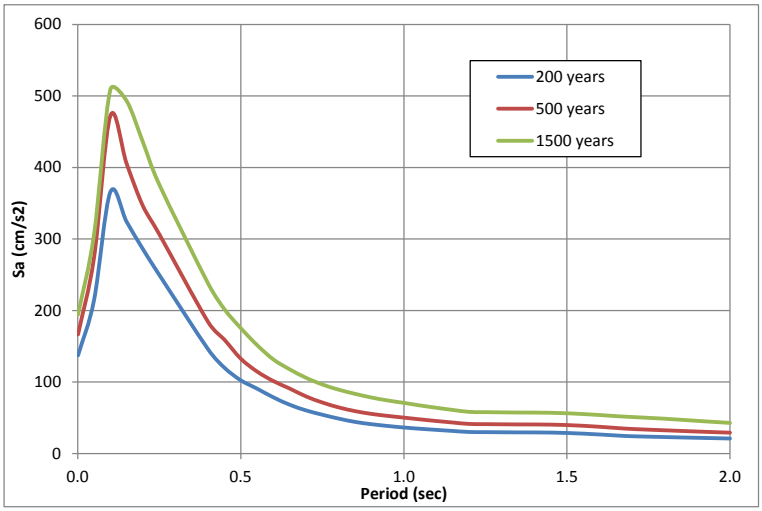

Figure 2. UHS at bedrock level in Lorca for 200, 500 and 1,500 years return period

2.2 Site effects

A microzonation study was recently published for Lorca (Navarro et al. 2014) and from it different homogeneous soil zones were identified as presented in Figure 3. Zones were assigned a soil classification according to the Eurocode-8 and spectral transfer functions were defined to account for the dynamic soil response and calculate the seismic hazard not at bedrock level but at the surface for the risk calculation process.

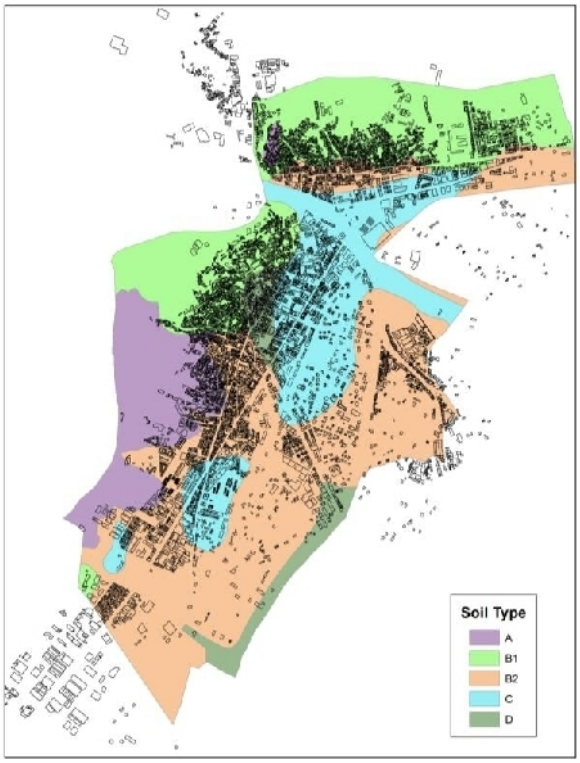

Figure 3. Homogeneous soil zones for Lorca

3. EXPOSED ASSETS OF LORCA

For a probabilistic risk assessment, the required database comprised by the portfolio of the exposed buildings of Lorca, both public and private, has been assembled. Such databases can be constructed using different scales or resolution levels. For this case, a detailed building by building resolution level was chosen since the required information was available. This process has always presented challenges in modelling since usually the required information is not available directly from a unique source and, in many cases it needs to be inferred or generated through indexes obtained from several sources. In this case, information about the geographical location and structural characteristics such as age, material, structural system, number of stories and building class is required for each element. Those parameters were assigned to each of the elements included in the final database using the data and procedure explained in this section.

When conducting a probabilistic seismic risk analysis, the main assumption is related to the law of large numbers, that is, a large set of elements are to be included in the database; thus even if over or under estimation errors are expected, they tend to be compensated on the final results.

3.1 Available information from the cadastral data

Updated cadastral information is available for Lorca (MHAP 2013) with a building by building resolution level. Since the information was generated for cadastral and tax purposes, several properties other than buildings such as terraces, squares and balconies are originally included. Initially, a total of 42,062 elements were included in the database. After a depuration process, intended to include only the buildings, only 17,017 elements remained; in this process, the buildings classified as ruins (before the 2011 earthquake) by the cadastral office were also removed. The cadastral information contains data about the geographical location and number of stories of each building. Building footprints were compared with an aerial image (ESRI 2010) and 599 additional elements were included in the database for a total of 17,064 buildings. Most of the buildings in Lorca are classified as low-rise from a structural point of view; i.e., buildings of 1 to 3 stories.

3.2 Vulnerability classification of the building portfolio

From the most recent Spanish population and housing census (INE 2011), it is possible to define the age distribution of the buildings in Lorca. Using the data of Table 1, this parameter was assigned to the elements on the database.

Table 1. Age distribution for the buildings in Lorca

Age	Distribution
Before 1900	4.4%
1900-1920	2.8%
1921-1940	4.0%
1941-1950	4.8%
1951-1960	11.1%
1961-1970	13.5%
1971-1980	19.4%
1981-1990	13.3%
1991-2001	13.1%
2002-2011	13.6%

Based on previous studies (Benito et al. 2005) and making use of the age distribution, a vulnerability classification based on the EMS-98 scale (Grünthal 1998) using the data of Table 2 was prepared. It can be seen from the table that structures are classified in categories between A and D on this scale. Figure 4 shows the geographical distribution of the vulnerability classes for the buildings of Lorca.

A field visit was conducted in February 2014 to determine the geographical distribution of the vulnerability official statistics. For that purpose, the city was divided into 11 zones.

Table 2. EMS 98 vulnerability class for the buildings in Lorca according to the age

	EMS98 vulnerability class	A	B	C	D
Age	**Before 1900**	80%	20%	-	-
	1900-1920	72%	28%	-	-
	1921-1940	72%	28%	-	-
	1941-1950	69%	28%	3%	-
	1951-1960	46%	49%	5%	-
	1961-1970	18%	38%	44%	-
	1971-1980	5%	40%	55%	-
	1981-1990	-	38%	57%	5%
	1991-2001	-	28%	62%	10%
	2002-2011	-	18%	69%	13%

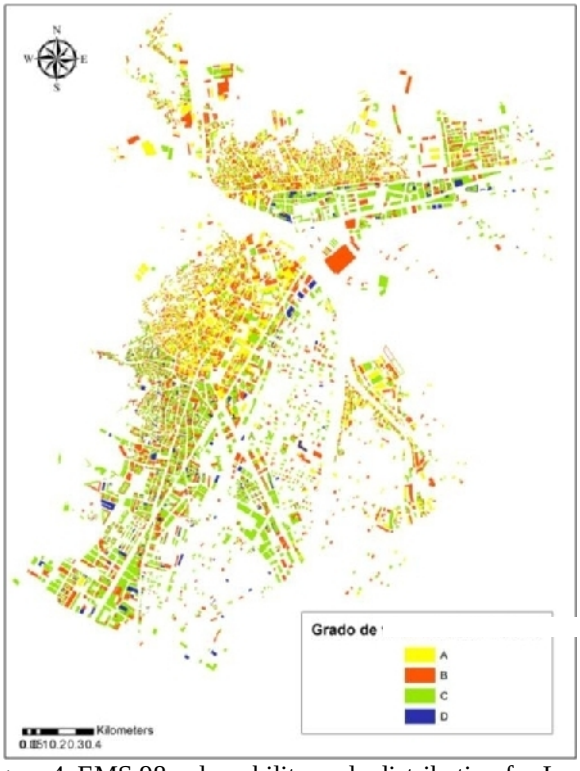

Figure 4. EMS 98 vulnerability scale distribution for Lorca

3.3 Portfolio appraisement

No cadastral price information was available in the database and for that reason an index based on the total constructed area was obtained to capture the replacement value of each element. The replacement cost is intended to capture the repair or replacing cost of the buildings to bring them to exactly the same condition as was initially characterized. The main objective of this appraisal is to establish an order of magnitude for the replacement cost of the buildings in Lorca as a whole. In this study, replacement costs do not take into account historical or heritage values of the structures.

Based on INE (2011) a base value of 1,247 euros per constructed square meter was established for the city; in addition to this, and in order to take into account the fact that all elements do not have the same price, age was selected as a differentiation parameter. Since repairing stone and brick masonry buildings is more expensive than repairing reinforced concrete buildings due to the necessity of specialized manpower, a factor that increases with the age was defined (see Table 3).

Table 3. Replacement costs and age factors for Lorca

Age	Age factor	Cost per constructed m2
Before 1900	2.00	2,494 €
1900-1920	2.00	2,494 €
1921-1940	1.75	2,182 €
1941-1950	1.75	2,182 €
1951-1960	1.50	1,871 €
1961-1970	1.50	1,871 €
1971-1980	1.50	1,871 €
1981-1990	1.25	1,559 €
1991-2001	1.25	1,559 €
2002-2011	1.00	1,247 €

By using this approach, the total replacement cost of the buildings in Lorca has been established in 6,927 millions of euros.

3.4 Building classes in Lorca

By having defined the age and vulnerability class distribution, several building classes were identified from the information collected by Benito et al. (2005). A vulnerability class according to the EMS-98 scale has been assigned to each building class. Buildings in Lorca are mostly made of different types of masonry (bricks and stone) for the low-rise structures while for medium- and high-rise buildings reinforced concrete (R/C) waffled slab buildings are mostly used. Steel frames and prefabricated R/C structures are found mostly in the industrial facilities

of the city.

By combining the above mentioned two parameters for all the elements, a building class was assigned to each dwelling and a total of 10 building classes were identified for the analysis. Table 4 shows the building classes which were identified and assigned for this study. In the second column an abbreviation code is included whereas in the third column the classification according to the EMS-98 vulnerability scale is shown.

Table 4. Building classes, abbreviation codes and EMS 98 vulnerability levels

Building class	Abbreviation code	Vulnerability class (EMS-98)
Stone masonry	M-PP	A
Earthen	M-TA	A
Toledo masonry	M-ET	B
Brick masonry	M-L	B
Masonry walls and R/C slabs	M-H	C
Pre 1995 R/C frames	E-H	C
Post 1995 R/C frames	E-H2	D
R/C frames with steel braces	E-HX	D
Prefabricated R/C structures	E-HF	C
Steel buildings	E-MT	D

Table 5 shows a summary of the exposed assets in terms of building classes and replacement values of each of them.

Table 5. Summary of exposed assets statistics

Building class	Exposed value	% of exposed value
Earthen	977,778,277 €	14.1
Stone masonry	848,085,666 €	12.2
Brick masonry	2,056,528,834 €	29.7
Masonry walls and R/C slabs	1,273,306,066 €	18.4
Stone and brick blocks	202,882,314 €	2.9
Steel buildings	8,205,336 €	0.1
R/C frames with steel braces	8,137,821 €	0.1
Pre 1995 R/C frames	1,292,810,399 €	18.7
Prefabricated R/C structutres	216,445,210 €	3.1
Post 1995 R/C frames	43,540,816 €	0.6
TOTAL	**6,927,720,740 €**	**100.0**

4. VULNERABILITY OF THE EXPOSED ASSETS

For this study only the physical vulnerability quantification is of interest from a structural engineering perspective. A vulnerability function approach (Miranda 1999; Ordaz et al. 1998) was selected for the damage and loss calculation process. Damage is represented through a continuous function that relates hazard intensities which in this case is the spectral acceleration for 5% damping, to the MDR, also considering its variance to account for the uncertainties. The value of the dispersion of the MDR changes along the intensity levels, being equal to zero at the extreme values of the interval and taking its maximum value for the intensity corresponding to a mean damage equal to 50%.

Vulnerability functions are a description of the variation of the first two statistical moments of loss with respect to the hazard intensity. A Beta probability distribution function is assigned and, in this case, the mean value and the standard deviation correspond to the mentioned statistical moments. Once this distribution function is computed, all the parameters required to compute risk in a probabilistic way are available (Ordaz 2000). This approach is compatible with the probabilistic risk assessment approach selected for the study. Each of the building classes has an associated vulnerability function. The replacement cost of each asset is needed to quantify the expected losses in monetary units since what it is obtained at each intensity level is the ratio of the repair cost relative to the total value of the building.

Structures with different characteristics behave and might be damaged in a different way when subjected to the lateral forces imposed by the same event and, therefore, hazard intensities for different spectral ordinates are calculated. This difference in the behavior of the buildings can be accounted using the fundamental period of each building class. Each vulnerability function has also an associated spectral ordinate that corresponds to the typical elastic fundamental period of the building class whose expected damage is being characterized, establishing the link between the vulnerability functions and the building classes.

A total of 22 vulnerability functions were used in the analysis, which have been developed for the Global Risk Model by CIMNE et al. (2013) and included in the Global Assessment Report on Disaster Risk Reduction 2013 (UNISDR 2013). Figure 8 shows the different vulnerability functions from where it is clear that some building classes, especially those made of unreinforced masonry, are far more vulnerable in seismic terms than others, having for the same intensity level a higher associated MDR. The codes of Table 4 are used to denote the vulnerability functions, and the height of the structures is included in the analysis through three different categories: low-rise (L) for buildings between 1 and 3 stories, medium-

rise (M) for those that have 4 to 7 stories and high-rise (H) for 8 and more. These abbreviations are also included in the notation used in Figure 5.

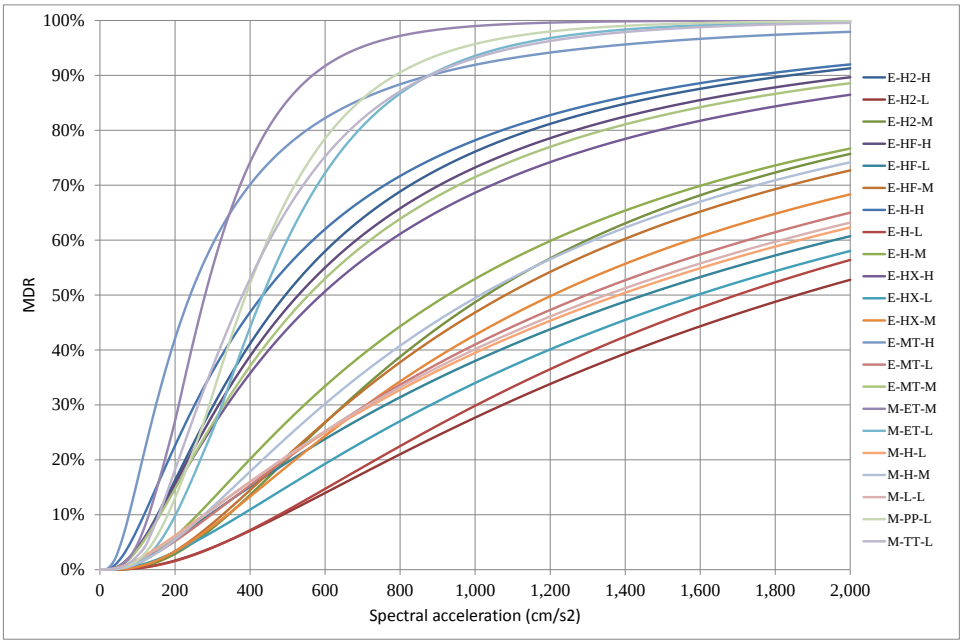

Figure 5. Vulnerability functions used for the buildings in Lorca (L=Low rise; M=Medium rise; H=High rise)

5. PROBABILISTIC SEISMIC RISK ASSESSSMENT

5.1 Methodology

A probabilistic risk analysis is usually conducted for the complete set of stochastic scenarios that are the outcome of a probabilistic seismic hazard assessment. Nevertheless, if it is required, the analysis can be performed for a single scenario. Using the methodology proposed by Ordaz (2000) and used in the CAPRA platform (ERN-AL 2010), the probability density function is $f(loss_j | Event_i)$ which allows calculating the loss on the j^{th} exposed asset, conditional to the occurrence of the i^{th} scenario. However, it is not possible to calculate this probability distribution directly; therefore, a chaining process between two different conditional probability distributions is required using:

$$f(loss_j \mid Event_i) = \int_0^\infty f(loss_j \mid Sa) \cdot f(Sa \mid Event_i) dSa \qquad (2)$$

where $f(loss_j|Sa)$ has to do with the vulnerability (the expected loss given a hazard intensity) and $f(Sa|Event_i)$ with the hazard (the hazard intensity given the occurrence of the event). Details about the aggregation of the losses can be found in Salgado et al. (2014) and in Torres et al. (2013).

Seismic risk, when calculated in a probabilistic way, should be expressed in terms of a loss exceedance curve that relates the frequencies with which losses exceeding a certain amount occur. It is usually computed in terms of the annual exceedance rate and calculated by using the following expression:

$$v(l) = \sum_{i=1}^{N} \Pr(L > l \,|\, Event_{\,i}) \cdot F_A(Event_{\,i}) \qquad (3)$$

where $v(l)$ is the rate of exceedance of loss p, N is the total number of hazard scenarios, $F_A\,(Event_{\,i})$ is the annual frequency of occurrence of the i^{th} hazard event, while $\Pr(L>l|Event_{\,i})$ is the probability of exceeding l, given that the i^{th} event occurred. The risk analysis was done in the CAPRA-GIS platform (ERN-AL, 2010) that constitutes the risk calculator of the initiative. Figure 6 presents a flowchart of the process.

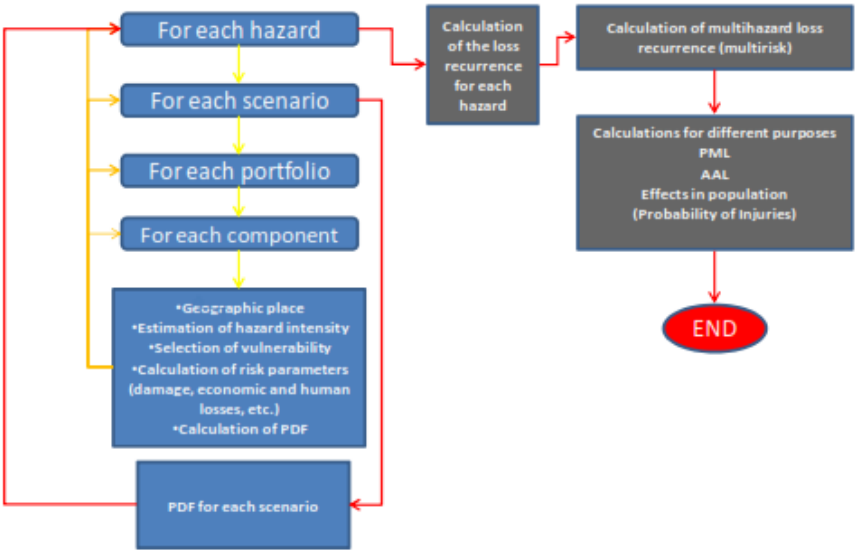

Figure 6. Probabilistic risk assessment flowchart

5.2 Seismic risk results for Lorca

Once the convolution process of hazard and vulnerability input information is performed, the expected loss information is obtained for the whole portfolio. These results include the consideration of the complete set of stochastic events, the representation of small, moderate and big events, the amplification provided by the soil conditions through the transfer functions, and finally the expected losses in each exposed element according to the assigned vulnerability function. The results are expressed in terms of the loss exceedance curve (LEC), and from it the average annual loss (AAL) and probable maximum losses (PML) for different return periods can be derived. Figure 7 presents the LEC for Lorca. Figure 8 presents the PML plot (left) and the loss exceedance probability for different exposure time frames (right). Table 6 summarizes the obtained seismic risk results.

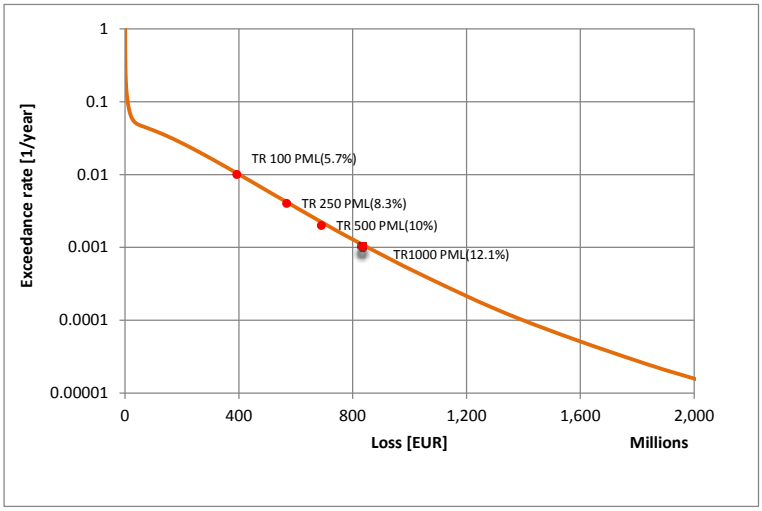

Figure 7. Seismic LEC for Lorca

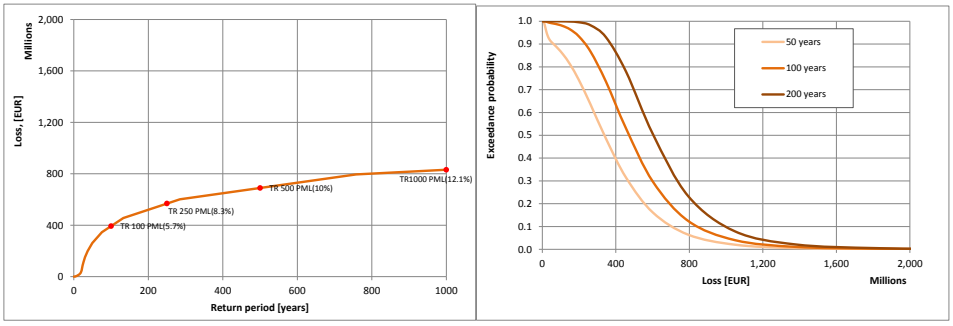

Figure 8. PML plot and loss exceedance probability for different timeframes

Table 6. Summary of the seismic risk results for Lorca

Restuls		
Exposed value	EURx10^6	6,927.72
Average annual loss	EURx10^6	16.329
	‰	2.357
PML		
Return period	Loss	
years	EURx10^6	%
100	$393.37	5.68
250	$568.50	8.21
500	$689.83	9.96
1000	$831.38	12.00

Another common way to express risk results is through maps where the spatial distribution of the expected losses can be visualized. Figure 9 presents the AAL for each of the elements comprised in the exposed assets database in terms of relative losses (to its replacement cost). Relative loss distribution is important because it is this parameter that allows the comparison between risk levels across the analysis area.

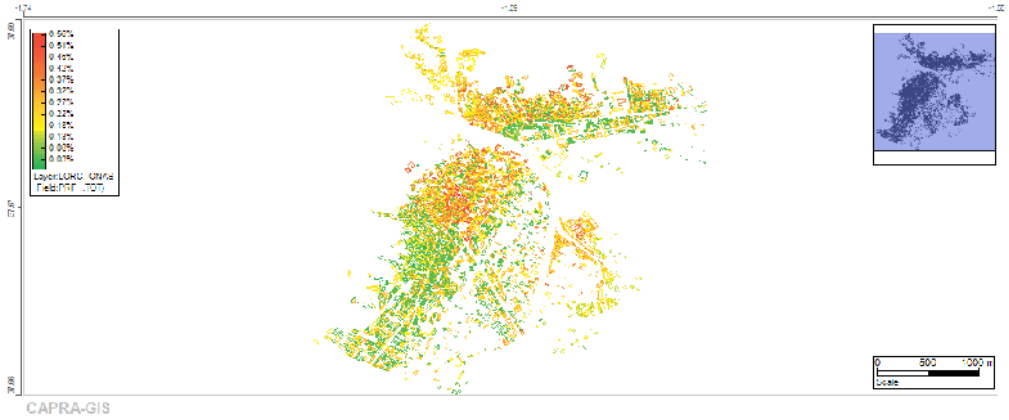

Figure 9. Risk map in terms of relative AAL for Lorca

Damage distribution is located mainly on the historical centre of the city. These zone has the oldest building stock of the city that subsequently has associated the highest seismic vulnerability levels. Maximum AAL values for buildings are around 5.6‰ which is a large risk figure. In the northern part of the city, where also old buildings exist, mainly comprised by masonry units, seismic risk results are high.

6. CONCLUSIONS

Earthquake risk models at urban level provide overall estimations that can be useful for decision-makers in terms of required resources and expected damage of the portfolio even if the exact location cannot be established. Therefore, if the results are mapped, a building by building resolution level risk assessment can be misleading since the simulated results could be interpreted as an exact prediction for each building, whilst they only represent mean values. Therefore, results in the best case should be grouped by categories, such as building classes, neighborhoods, counties, etc.

Lorca besides having a moderate seismic hazard level as presented in the UHS on section 2 has high physical vulnerability levels that lead to high risk values. Though so far the effects have been assessed only for the direct physical losses, these results can be used as input values to consider second order effects and other potential losses.

Physical risk in terms or AAL and PML can be later used in the design of risk retention and transfer schemes through classical insurance-reinsurance contracts or making use of alternative risk transfer instruments such as contingent loans, catastrophe bonds or even off-shore cautives.

In terms of the exposure database used in this study, many parameters could be captured without an individual survey and, therefore, a grouping process among building classes was followed. Data gathering processes should be encouraged at different resolution levels so that the collected and organized information can be used to refine and improve the damage and loss estimations.

Acknowledgements

The authors are grateful for the support of the Ministry of Education and Science of Spain "Enfoque integral y probabilista para la evaluación del riesgo sísmico en España"— CoPASRE (CGL2011-29063) and to the Spanish Ministry of Economy and Competitiveness in the framework of the researcher's formation program (FPI).

References

1. Ambraseys N., Douglas J., Sarma K., Smit P. (2005). Equations for the estimation of strong ground motions from shallow crustal earthquakes using data from Europe and the Middle East: Horizontal peak ground acceleration and spectral acceleration. *Bull. of earthq. En.* 3(1). 1-53.
2. Benito B., Rivas A., Gaspar-Escribano J., Murphy P. (2012). El terremoto de Lorca (2011) en el contexto de la peligrosidad y el riesgo sísmico en Murcia. *Fís. de la Tierra*. 24:255-287.
3. Benito B., Carreño E., Jiménez M., Murphy P., Martínez J., Tsige M., Gaspar J. García M., García J., Canora C., Álvarez J. García I. (2005). *Riesgo Sísmico en la Región de Murcia* – RISMUR. Instituto Geográfico Nacional. España.
4. Cardona O., Ordaz M., Reinoso E., Yamín L., Barbat A. (2012). CAPRA – Comprehensive Approach to Probabilistic Risk Assessment: International Initiative for Risk Management Effectiveness. *Procedures of the 15th World Conference on Earthquake Engineering*, Lisbon, Portugal.
5. Cardona O., Ordaz M., Reinoso E., Yamín L., Barbat A. (2010). Comprehensive Approach to Probabilistic Risk Assessment (CAPRA). International initiative for disaster risk management effectiveness. *Procedures of the 14th European conference on earthquake engineering*, Ohrid, Macedonia.
6. CIMNE, EAI, INGENIAR, ITEC (2013). *Probabilistic modeling of natural risks at the global level: Global Risk Model.* http://www.preventionweb.net/english/hyogo/gar/2013/en/home/documents.html Accessed on January 03, 2014.
7. Cornell A., Van Marke E.H. (1969). The major influences on seismic risk. *Procedures of the 3rd World Conference on Earthquake Engineering*. Santiago, Chile.
8. ESRI ArcMap (2010). Basemap imagery.
9. Evaluación de Riesgos Naturales América Latina - ERN-AL (2010). *Comprehensive Approach to Probabilistic Risk Assessment*, http://www.ecapra.org. Accessed on January 03, 2014.
10. German Research Center for Geosciences – GRCG (2010). *Seismic Hazard Harmonization in Europe SHARE*. Development of a common methodology and tools to evaluate earthquake hazard in Europe. Theme 6: Environment. German Research Center for Geosciences.
11. Grünthal G. (1998). *European Macroseismic Scale*. Centre Européen de Géodynamique et de Séismologie.
12. Gutenberg R., Richter C.F. (1944). Frequency of earthquakes in California. *Bull. of the seismol. soc. of am.* 34:185-188.
13. Instituto Geográfico Nacional - IGN (2013a). "Catálogo de terremotos". http://www.ign.es/ign/layoutIn/sismoFormularioCatalogo.do, Accessed on September 1, 2013.
14. Instituto Geográfico Nacional - IGN (2013b). *Actualización de mapas de peligrosidad sísmica de España 2012*. Ministerio de Fomento. Gobierno de España.
15. Instituto Nacional de Estadística - INE (2011). Censo de población y vivienda 2011. http://www.ine.es/censos2011_datos/cen11_datos_res_pob.htm. Accesed on December 10, 2013.
16. Marulanda M., Carreño M., Cardona O., Ordaz M., Barbat A. (2013) *Probabilistic earthquake risk assessment using CAPRA: application to the city of Barcelona*, Spain. Nat. Hazards. DOI: 10.1007/s11069-013-0685-z.
17. McGuire R. (2004). *Seismic hazard and risk analysis*. Earthquake Engineering Research Institute. Oakland, California, United States of America.
18. Ministerio de Hacienda y Administración Pública – MHAP . (2013). Dirección General del Catastro. http://www.catastro.meh.es/. Accessed on September 15, 2013.
19. Miranda E. (1999). Approximate seismic lateral deformation demands in multistory buildings. *J. of Struct. Eng. 125*(4): 417-425.
20. Navarro M., García-Jerez A., Alcalá F.J., Vidal F., Enomoto T. (2014). Local site effect microzonation of Lorca town (SE Spain). *Bulletin of Earthquake Engineering. 12*:1933-1959.

21. Norma de la Construcción Sismorresistente Española (NCSE-02). (2002). Real Decreto 997/2002 de 27 de septiembre por el que se aprueba la norma de construcción sismorresistente: parte general y edificación (NCSR-02). Boletín Oficial del Estado. 244. 35898-35967.
22. Ordaz M, Aguilar A, Arboleda J, (2007). CRISIS 2007 V7.6, Program for computing seismic hazard. Instituto de Ingeniería. Universidad Nacional Autónoma de México.
23. Ordaz M. (2000) *Metodología para la evaluación del riesgo sísmico enfocada a la gerencia de seguros por terremoto*. Universidad Nacional Autónoma de México, México D.F.
24. Ordaz M., Miranda E., Reinoso E., Pérez-Rocha L. (1998). Seismic loss estimation model for Mexico City. *Procedures of the 12th World Conference on Earthquake Engineering*. Auckland, New Zealand.
25. Salgado M., Zuloaga D., Bernal G., Mora M., Cardona O. (2013a). Fully probabilistic seismic risk assessment considering local site effects for the portfolio of buildings in Medellín, Colombia. *Bull. of earthq. eng.* DOI: 10.1007/s10518-013-9550-4.
26. Salgado M., Zuloaga D., Cardona O. (2013b). Evaluación probabilista del riesgo sísmico de Bogotá y Manizales con y sin la influencia de la Caldas Tear. *Rev. de ing. 38*:6-13. Universidad de Los Andes, Bogotá, Colombia.
27. Tinti S., Mulargia F. (1985). An improved method for the analysis of the completeness of a seismic catalogue. *Lett. al nuovo cim.* Series 2. 42(1):21-27.
28. Torres M., Jaimes M., Reinoso E., Ordaz M. (2013). Event-based approach for probabilistic flood risk assessment. *Intern. j. of river basin manag*. DOI: 10.1080/15715124.2013.847844.
29. United Nations International Strategy for Disaster Risk Reduction-UNISDR (2013). *Global Assessment Report on Disaster Risk Reduction* 2013. Geneva, Switzerland.

Survey on Methods for Parametric Identification

Lăzărică Teșu[1], Gabriela M.Atanasiu[1]
1 Department of Structural Mechanics, "Gheorghe Asachi" Technical University, Iaşi, 700050, Romania

Summary

The goal of this article is to offer a brief survey in the field of system identification methods, which can be applied in civil engineering computations using modern programming software such as MATLAB. The main objective of the system identification is to model dynamic processes using experimental data. The mathematical models used in the identification process are based on continuous models that offer a simplified solution for the real civil engineering structures that are being analyzed. For the validation process of these models, the parametric identification process is used to estimate the structures parameters so as they are close as possible to the parameters generated in experimental conditions on the same structure.

KEYWORDS: modeling, estimation, parametric identification, MATLAB applications.

1. INTRODUCTION

The field of system identification uses statistical methods to predict mathematical models of dynamical systems based on observations or previous information. The estimated model represents the actual system and it needs to be accurately identified due to the fact that the parameters used in these models have real physical meaning.

The dynamical model exists in various forms, depending on the system identification method used. Among these forms we mention, the lumped or distributed model, the continuous time and discrete time model, the input-output and state space model, the frequency domain and time domain model, the parametric and non-parametric model, the white box and black box model, [1].

The parametric model (white box models) is the model in which the transmission of the signal through the object is supposed to be known and can be described by differential equations.

In non-parametric model, modeling the geometrical and the physical structure of a system are established by means of regression or correlation analysis (behavior model), [2].

2. IDENTIFICATION AND MODELING OF LINEAR DYNAMIC SYSTEM

2.1. Dynamic system analysis, modeling and identification

The mathematical or analytical models represent a symbolic representation of real phenomenon using abstract mathematical formulation. For each component of the system a variable or parameter can be attributed to it. The parameters are attributes of the system that don't depend on the other components, [3].

The selection of the model structure needs to be done with care, so that the parameter values will closely match the systems behavior. Also the structure should be simple enough so that these parameters can be identified without an excessive amount of data, [4]. We can validate the model by checking if the generated data from the model is close to the data generated in experimental conditions of the real system.

Recognizing the sources and locations of the modeling errors in preliminary models can help analysts implement experimental validation and assess the reliability of structural predictions from refined models. The most commonly encountered modeling errors are: discretization errors, parameter errors and conceptualization errors.

2.2. Parametric models for linear dynamic systems

If we consider the construction's structure of a known system, then we can use a parametric model to best describe the system, in which the information about the system is being represented by a set of parameters.

The mathematical models used to describe complex systems are made up of algebraic equations, differential equations and/or partial derivative equations. The variables used depend on the type of equation, among these independent variables we mention time, space etc.

A linear dynamic system can be described with the help of linear differential equations of order n with constant coefficients:

$$\sum_{i=0}^{n} a_i \frac{d^i y(t)}{dt^i} = \sum_{j=0}^{m} b_j \frac{d^j u(t)}{dt^j}; \qquad \frac{d^r y(0)}{dt^r} = y_{0r}; \quad \frac{d^v u(0)}{dt^v} = u_{0v}; \tag{1}$$

$$r = \overline{0, n-1}; \quad v = \overline{0, m-1}; \quad a_n = 1$$

where: a, b are parameters of the model; $u(t)$ is the input signal; $y(t)$ is the output signal; r is the covariance parameter; v is the noise; t is the time.

The model (1) represents a continuous parametric model, having the parameters vector described by the differential equations coefficients:

$$\theta = \left[a_{n-1} \;\; a_{n-2} \;\; \ldots \;\; a_0 \;\; b_m \;\; b_{m-1} \;\; \ldots \;\; b_0 \right]^T \tag{2}$$

The state of a system can be described with the help of a set of state variables $x_1(t), x_2(t), \ldots x_n(t)$ and an input signal. The evolution in time for these variables can be interpreted as a trajectory in a n-dimensional space, called state space. This approach offers vast modeling possibilities for a wide range of systems.

In the case of linear systems, the states are described as a set of differential equations of first order in terms of the state variables and input variable:

$$\begin{aligned}
\frac{dx_1(t)}{dt} &= a_{11}x_1(t) + a_{12}x_2(t) + \ldots + a_{1n}x_n(t) + b_1 u(t) \\
\frac{dx_2(t)}{dt} &= a_{21}x_1(t) + a_{22}x_2(t) + \ldots + a_{2n}x_n(t) + b_2 u(t) \\
&\vdots \\
\frac{dx_n(t)}{dt} &= a_{n1}x_1(t) + a_{n2}x_2(t) + \ldots + a_{nn}x_n(t) + b_n u(t) \\
x_1(0) &= x_{10}; x_2(0) = x_{20}; \ldots; x_n(0) = x_{n0};
\end{aligned} \tag{3}$$

or, in matrix form:

$$\dot{X}(t) = AX(t) + Bu(t); \quad X(0) = X_0 \tag{4}$$

The output for this system can be expressed as:

$$y(t) = c_1 x_1(t) + c_2 x_2(t) + \ldots + c_n x_n(t) + du(t) \tag{5}$$

where: $c_1, c_2, \ldots c_n$ are input parameters of the model.

or, in matrix form:

$$Y(t) = CX(t) + DU(t) \tag{6}$$

where: $\mathbf{Y}$ is the output vector; $\mathbf{X}$ is the state vector;

The systems response for an input signal can be obtained by evaluating the state of the system, $\mathbf{X}(\mathbf{t})$, and the output, $\mathbf{y}(\mathbf{t})$. The evolution of the states is defined by the differential equations (3), with the initial conditions $\mathbf{X_0} = \left[\mathbf{x_{10}}\ \ \mathbf{x_{20}}\ \ \ldots\ \mathbf{x_{n0}}\right]^{\mathbf{T}}$. The solution for the equation (4) will be:

$$\mathbf{X}(\mathbf{t}) = \mathbf{e}^{\mathbf{At}}\mathbf{X_0} + \int_{\mathbf{0}}^{\mathbf{t}} \mathbf{e}^{\mathbf{A}(\mathbf{t}-\boldsymbol{\tau})}\mathbf{Bu}(\boldsymbol{\tau})\,\mathbf{dt} \tag{7}$$

Where the first term of the equation represents the effect of the initial conditions, $\mathbf{X_0}$, and the second term represents the effect of the input signal $\mathbf{u}(\mathbf{t})$.

2.3. Parameter Identification and Estimation

The parametric identification methods are precise, efficient and easy to apply. The parametric models can be described if we know the shape indices and the dead time, or they can be completely described if we know the numerical values of the parameters and the initial conditions. By applying the fundamental laws of physics (Newton's law, mass equilibrium, etc.) to a modeled process we can determine numerical values for all the models parameters that depend on the physical parameters of the process. The behavior of the system can be determined only after an excitation is applied with a signal $\mathbf{u}(\mathbf{t})$.

The parameter estimation methods follow two main steps:

1. First step, in which, starting from the dynamic model type of the system, we establish a system of equations for estimating the parameters, as it is presented in Equation (8):

$$\mathbf{y}(\mathbf{t}) = \mathbf{M}(\mathbf{u}(\mathbf{t}), \boldsymbol{\theta}) \tag{8}$$

2. Second step, where, based on the estimation equations (parametric model), we determine the parameters vector $\boldsymbol{\theta}$ of the model with the help of the adopted estimation method.

If we consider the parameter estimation problem as an optimization problem, then we need to minimize a functional $\mathbf{V}(\boldsymbol{\theta})$. If we define the parameters space that needs to be determined $\boldsymbol{\theta}_\mathbf{i}$, the model is represented by $\boldsymbol{\theta}^{\mathbf{M}}$, the system by a point $\boldsymbol{\theta}^{\mathbf{S}}$ and de distance between the model and system by $\mathbf{D}(\mathbf{S},\mathbf{M})$. Applying the optimization process the distance with respect to the parameters values will be minimized.

$$\mathbf{V}(\boldsymbol{\theta}) = \mathbf{D}^2(\mathbf{S},\mathbf{M}) = \int_0^{\mathbf{T}} \mathbf{e}^2(\mathbf{t})\,\mathbf{dt} \tag{9}$$

When defining the distance between the system and model the following types of errors can be used:

- Input errors:

$$\mathbf{e}(\mathbf{t}) = \mathbf{y}(\mathbf{t}) - \hat{\mathbf{y}}(\mathbf{t}) = \mathbf{y}(\mathbf{t}) - \mathbf{M}(\mathbf{u}(\mathbf{t}),\boldsymbol{\theta}) \tag{10}$$

- Output errors:

$$\mathbf{e}(\mathbf{t}) = \mathbf{u}(\mathbf{t}) - \hat{\mathbf{u}}(\mathbf{t}) = \mathbf{u}(\mathbf{t}) - \mathbf{M}^{-1}(\mathbf{u}(\mathbf{t}),\boldsymbol{\theta}) \tag{11}$$

- General errors:

$$\mathbf{e}(\mathbf{t}) = \mathbf{M}_2^{-1}(\mathbf{u}(\mathbf{t}),\boldsymbol{\theta}^1) - \mathbf{M}_1(\mathbf{u}(\mathbf{t}),\boldsymbol{\theta}^2) \tag{12}$$

After we minimize the functional $\mathbf{V}(\boldsymbol{\theta})$ we obtain the estimator function:

$$\hat{\boldsymbol{\theta}} = \hat{\boldsymbol{\theta}}\{\mathbf{u}(\mathbf{t}),\mathbf{y}(\mathbf{t}),\mathbf{t}\in[\mathbf{0},\mathbf{T}]\} \tag{13}$$

3. PARAMETER ESTIMATION METHODS

Depending on the system identification used, we obtain various estimation methods, based on the type of errors that can appear (output errors, modeling errors, prediction errors). The parameter estimation methods follows two main steps in which the system of equation for parameter estimation is established and after that the models parameters can be determined using the adopted estimation method.

During the first step an algebraic matrix equation is obtained, using regression equations and measurement values:

$$\mathbf{Y} = \boldsymbol{\Phi}\boldsymbol{\theta} + \mathbf{V} \tag{14}$$

where:

$$\boldsymbol{\theta} = [\mathbf{a}_1 \quad \mathbf{a}_2 \ldots \mathbf{a}_n \quad \mathbf{b}_0 \quad \mathbf{b}_1 \ldots \mathbf{b}_m]^{\mathbf{T}} \tag{15}$$

$$\mathbf{Y} = [\mathbf{y}(\mathbf{t}_1)\ \mathbf{y}(\mathbf{t}_2)\ \ldots\ \mathbf{y}(\mathbf{t}_N)]^{\mathbf{T}} \tag{16}$$

$$\mathbf{V} = [\mathbf{v}(\mathbf{t}_1)\ \mathbf{v}(\mathbf{t}_2)\ \ldots\ \mathbf{v}(\mathbf{t}_N)]^{\mathbf{T}} \tag{17}$$

$$\boldsymbol{\Phi} = \begin{bmatrix} \boldsymbol{\varphi}^{\mathbf{T}}(\mathbf{t}_1) \\ \boldsymbol{\varphi}^{\mathbf{T}}(\mathbf{t}_2) \\ \vdots \\ \boldsymbol{\varphi}^{\mathbf{T}}(\mathbf{t}_N) \end{bmatrix} = \left[\boldsymbol{\Phi}_{\mathbf{y}} \vdots \boldsymbol{\Phi}_{\mathbf{u}} \right] \tag{18}$$

where: $\boldsymbol{\theta}$ is the parameters vector; $\mathbf{Y}$ is the output vector; $\mathbf{V}$ is the functional; $\boldsymbol{\Phi}$ is the state vector of the considered system.

The second step does not depend on the type of the model (continuous or discrete), but only on the system of equations for the parameter estimation. With minor adjustments, the estimating methods, developed with the help of the discrete models, can be used for the parameter estimation of continuous models.

3.1. The Least Squares Method

The least square method is widely used to find or estimate the numerical values of the parameters to fit a function to a set of data and to characterize the statistical properties of estimates.

The set of equation obtained in the first step is represented by:

$$\mathbf{Y}^{*} = \boldsymbol{\Phi}^{*}\boldsymbol{\theta} + \mathbf{E}^{*} \tag{19}$$

where: $\boldsymbol{\theta}$ is the parameters vector; $\mathbf{Y}^{*}$ is the output vector; $\mathbf{E}^{*}$ is the error vector; $\boldsymbol{\Phi}^{*}$ is the state vector of the considered system.

The parameters vector results from the minimization condition of the mean squared modeling error:

$$\begin{aligned} \hat{\boldsymbol{\theta}} &= \arg\min_{\boldsymbol{\theta}} \mathbf{J}(\boldsymbol{\theta}) = \arg\min_{\boldsymbol{\theta}} \frac{\mathbf{1}}{\mathbf{2}} \mathbf{E}^{*\mathbf{T}} \mathbf{E}^{*} = \\ &= \arg\min_{\boldsymbol{\theta}} \frac{\mathbf{1}}{\mathbf{2}} \left(\mathbf{Y}^{*} - \boldsymbol{\Phi}^{*}\boldsymbol{\theta} \right)^{\mathbf{T}} \left(\mathbf{Y}^{*} - \boldsymbol{\Phi}^{*}\boldsymbol{\theta} \right) \end{aligned} \tag{20}$$

The estimation of the vector $\hat{\boldsymbol{\theta}}$ is given by the relation:

$$\hat{\boldsymbol{\theta}} = \left[\boldsymbol{\Phi}^{*\mathbf{T}} \boldsymbol{\Phi}^{*} \right]^{-1} \boldsymbol{\Phi}^{*\mathbf{T}} \mathbf{Y}^{*} = \tilde{\boldsymbol{\Phi}}^{*-1} \boldsymbol{\Phi}^{*\mathbf{T}} \mathbf{Y}^{*} \tag{21}$$

This method can be used in the preliminary estimation stages.

3.2. The weighted least squares method

If the noise $\mathbf{v}(\mathbf{t})$ is correlated, $\mathbf{M}\left[\mathbf{v}(\mathbf{t})\right] = \mathbf{0}$ and the covariance matrix is $\mathbf{R}_{\mathbf{v}} = \mathbf{M}\left[\mathbf{v}^2(\mathbf{t})\right] > \mathbf{0}$, then the estimator for the least squares method becomes the estimator for the weighted least squares method. The equation of errors is given by:

$$\mathbf{A}(\mathbf{p})\mathbf{y}_0^*(\mathbf{t}_k) - \mathbf{B}(\mathbf{p})\mathbf{u}_0^*(\mathbf{t}_k) = \mathbf{v}_0^*(\mathbf{t}_k) \tag{22}$$

The system is described by the following equation:

$$\mathbf{Y}_c^* = \mathbf{\Phi}_c^*\boldsymbol{\theta} + \mathbf{V}_c^* \tag{23}$$

where: $\boldsymbol{\theta}$ is the parameters vector; $\mathbf{Y}_c^*$ is the corrected output vector; $\mathbf{V}_c^*$ is the white noise vector; $\mathbf{\Phi}_c^*$ is the corrected state vector.

The white noise $\mathbf{V}_c^*$, can be used to determine the estimator of the weighted least squares method:

$$\hat{\boldsymbol{\theta}} = \left[\mathbf{\Phi}^{*\mathbf{T}}\mathbf{W}\mathbf{\Phi}^*\right]^{-1}\mathbf{\Phi}^{*\mathbf{T}}\mathbf{W}\mathbf{Y}^* \tag{24}$$

where: $\mathbf{W}$ is the weighted matrix,

$$\mathbf{W} = \mathbf{R}_{\mathbf{v}^*}^{-1} \ . \tag{25}$$

4. CASE STUDY BASED ON SYSTEM IDENTIFICATION TOOLBOX

Over time a wide range of software applications that implement the identification methods for discrete time models have proven themselves efficient in various practical applications. Among these we mention the System Identification Toolbox that is part of the MATLAB software package, [5].

To better illustrate the capabilities of the System Identification Toolbox an analysis will be carried out on a single degree of freedom (SDOF) system of a real structure with the following material and dynamic characteristics:

$$E = 3e7\ KN/m^2; \quad \omega = 54.569\ Hz;$$
$$\zeta = 0.2; \quad T = 0.115\ \text{sec};$$
$$m = 960.37\ t; \quad c = 2.096e4.$$
$$k = 2.86e6\ KN/m;$$

Using single-input/single-output (SISO) data we can estimate and validate linear models that best describe the system dynamics. For the SDOF system we use time-domain data to identify the required parameters. The input and output signals each contain 500 data samples.

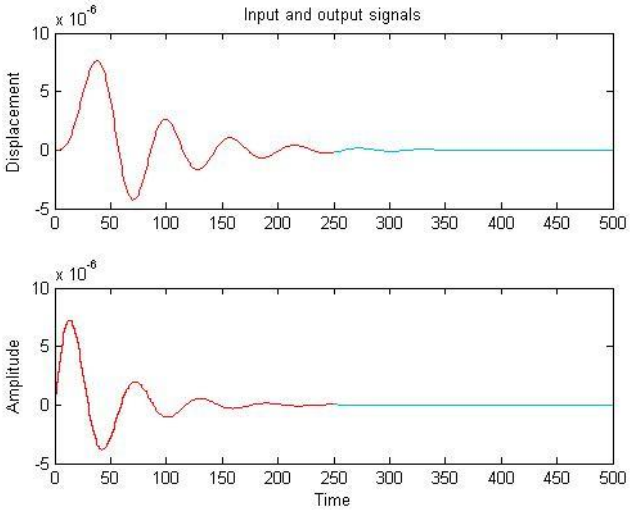

Figure 1. Time plot: Amplitude-Displacement

Using the System Identification Toolbox we can quickly estimate linear models for the SDOF system and obtain plots for the step response, frequency-response, and the output of state-space and polynomial models. These plots are later used to validate the quality of the models.

The model-output plot obtained shows the model response to the input data. The models that best fit are ordered from top to bottom.

In order to determine the model order, we can estimate simple polynomial (ARX) models for a range of orders and delays and then compare the performance of the models. We choose the orders and delays that correspond to the best model fit.

Examining the model output we choose the model with the best performance. A good model is the simplest model that best describes the dynamics and that successfully simulates or predicts the output for different inputs.

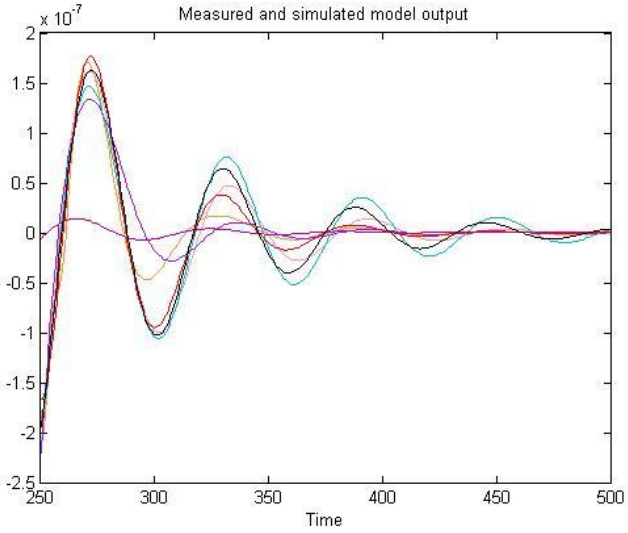

Figure 2. Measured output and model output for the estimated models

The LTI viewer can be used to display and manipulate the response plots of the estimated linear models.

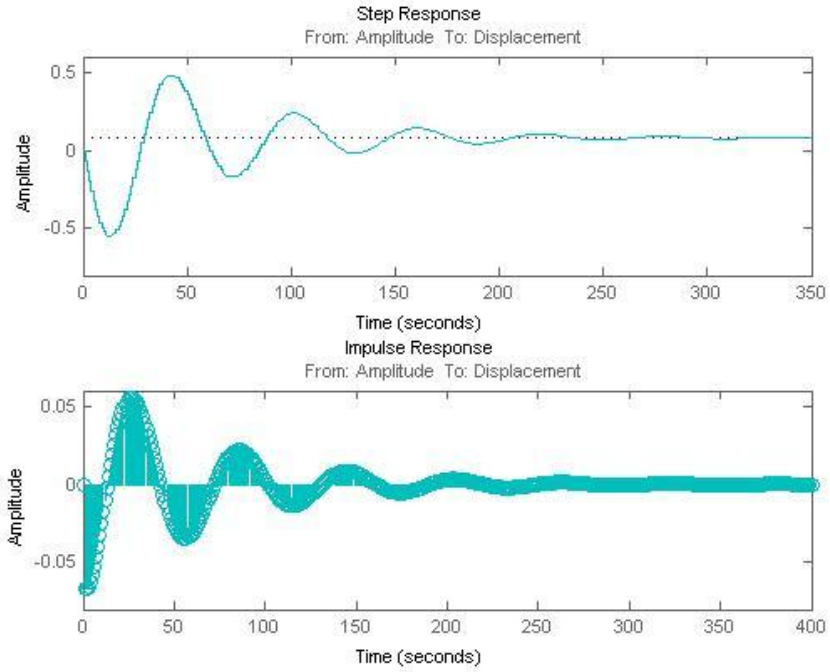

Figure 3. Step Response and Impulse Response in LTI Viewer

5. CONCLUSIONS

When consider a models for different classes of construction's structure, the models estimated based on system identification can be used to interpret the observed values, to establish the correct actions in controlling the systems output and also in predicting their evolution on a period of time.

Based on the histogram of input-output signals, system identification offers a suitable model that best describes the systems properties.

The System Identification Toolbox can be used to construct mathematical models of dynamic systems from measured input-output data. It can use time-domain and frequency-domain input-output data to identify continuous-time and discrete-time transfer functions, process models, and state-space models. The toolbox can perform grey-box system identification for estimating parameters of a given model.

References

1. Abdullah, L., Jamaludin, Z., Chiew, T. H., Rafan, N. A., and Mohamed, M. S. S., "System Identification of XY Table Ballscrew Drive Using Parametric and Non Parametric Frequency Domain Estimation Via Deterministic Approach," *Procedia Engineering*, vol. 41, pp. 567-574, 2012.
2. Țeșu, L. and Atanasiu, G. M., "Applying parameter identification of structural models assisted by MATLAB," *Buletinul IPI*, Tomul LVIII(LXII), Fasc.3, 2012.
3. Horga, V. and Ganciu, T., *Identificarea sistemelor continue*. Iași: Ed. Politehnium, 2009.
4. Novara, C., Vincent, T., Hsu, K., Milanese, M., and Poolla, K., "Parametric identification of structured nonlinear systems," *Automatica*, vol. 47, pp. 711-721, 2011.
5. MathWorks. http://www.mathworks.com/help/ident/index.html

FE Modeling of Thin Layer Mineral Composite Glass Fiber Reinforced Old Masonry Walls

George Ţăranu[1], Mihai Budescu[1], Vitalie Florea[1] and Ionuţ Ovidiu Toma[1]
[1]*Department of Structural Mechanics, "Gheorghe Asachi" Technical University of Iaşi, 700050, Romania*

Summary

Masonry structures are commonly used in Romania and not only. This is due to its many advantages in terms of mechanical behavior based on increased capacity of stress redistribution. In addition to traditional strengthening solutions, composite materials are an advantageous alternative due to the high strength versus weight ratio. This paper presents an experimental and numerical analysis on old brick masonry specimens made with weak lime mortar and limestone sand, subjected to uniaxial compression. The results were compared with finite element numerical analysis in order to show stress distribution between brickwork and strengthening layers applied. Several forms of strengthening application relative to masonry faces (interior and exterior) were considered in the numerical analysis. The beneficial effect on the mechanical behavior of strengthened masonry in terms of stress and strain distribution of both masonry and strengthening layers is shown to be dependent on the thickness of the strengthening layer.

Keywords: masonry strengthening, glass fiber mineral composites, mechanical behavior

1. INTRODUCTION

Starting with Roman civilization masonry structures made with ceramic bricks were widely used in construction worldwide because these structural systems have progressed significantly due to the process of baking bricks in kilns. Depending on local resources, masonry have been adapted to the possibilities of the regions where they were applied. Different combinations of mortar were identified in Romania as part of old masonry [1, 2].

Research in the past years at the Faculty of Civil Engineering of Iasi focused on masonry systems made with local materials [3, 4]. One of them is a sandy limestone called pufar mined near Iasi on Bucium hill (Pietraria village). Many churches and houses were made with masonry structure and mortar with pufar during the XVIIth - XVIIIth century. This mortar is characterized by reduced strength and large deformations capability. These masonry systems have a good

behavior to multiple seismic actions that occurred during the life of the buildings analyzed. In this context the apparition and damage increasing to significant degradation require structurally efficient building solutions.

One of these solutions was identified by using a composite material with reinforced glass fiber mineral matrix [5, 6, 7]. The paper presents some experimental results and numerical analyses on unstrengthened masonry elements and strengthened with composite material.

2. MATERIALS

For the purpose of the experiments, 20 elements of masonry ceramic bricks with pufar mortar were made. The bricks were specially made by molding and baking clay, at 1:2 scale with dimensions of 117x60x36. The sand (pufar) was extracted from the hill near to Iasi and sieved with 2 mm sieve. Lime slurry was used as binder. Wet mortar has a good workability and adherence due to lime binder. Figure 1a presents a sample of simple masonry executed with same thickness of mortar joints.

In the second stage, for strengthening samples were used fiberglass mesh alkali resistant with 5x5mm network and mineral matrix. A strengthening layer of 1 cm thick, was applied by pouring fluid into a prismatic shape. The fluid mix is a combination of sand, Portland cement and calcium sulphate in β anhydride III' form manufactured from industrial wastes [8, 9]. Figure 1 presents the stages of execution and pouring of masonry samples.

a

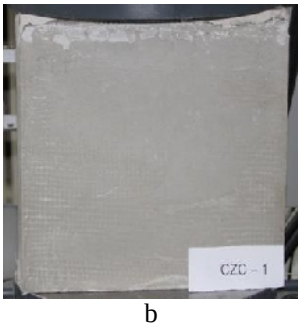

b

Figure 1. Old masonry samples: a- simple unstrengthened masonry; b- glass fiber reinforced mineral composite samples

3. EXPERIMENTAL PROGRAM

Before testing the masonry samples, their component characteristics were determined. Masonry elements were tested in compression in a universal machine. Tests consisted of 5 samples of each type of masonry. The dimensions of the samples tested, as well as the loading schema are shown in Figure 2.

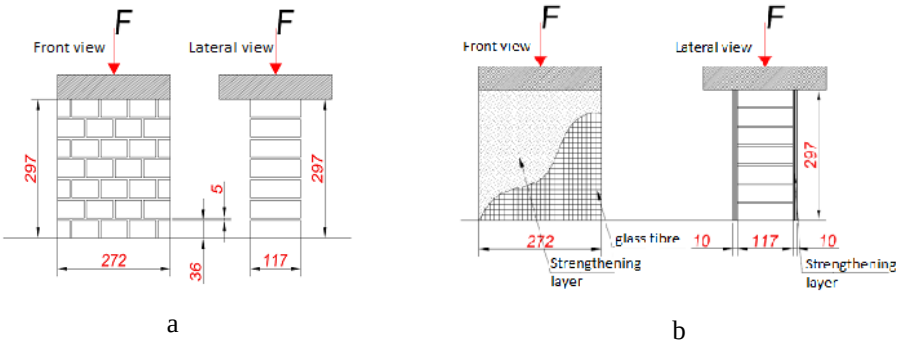

Figure 2. Dimensions and loading schema: a- uniaxial compression on simple masonry, b- uniaxial compression on strengthened masonry

The test was force controlled with a loading rate of 0.01 N/mm2/s, until samples yielded completely. Displacements were measured with displacement transducer of the testing machine. Each of the 5 tests took about 25-30 min. The test was stopped when the failure of the samples occurred.

4. RESULTS AND DISCUSSIONS

The un- strengthened masonry samples tested in axial compression yielded by the appearance of vertical cracks parallel to the direction of force. They originally appeared in the layers of mortar after that in all the mass of bricks. The strengthened samples failure differs by taking in an early stage of deformation of thin strengthening layer.

In these layers cracks were also propagated in the parallel direction to the loading of the sample. In figure 3 a, b the average stress – strain curve for the tested samples are shown.

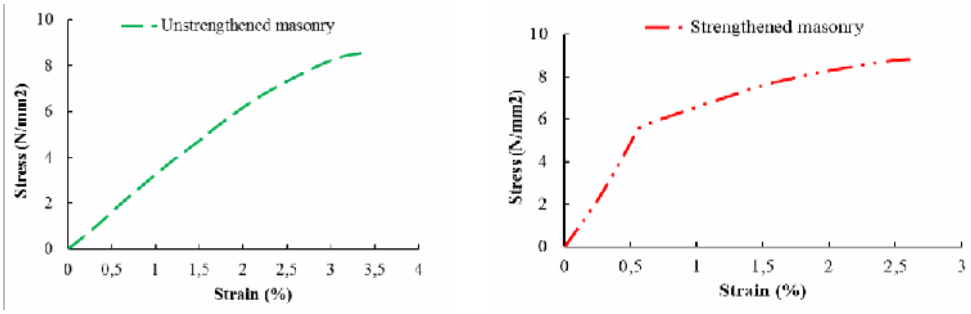

a b

Figure 3. Stress strain curve for: a- unstrengthened masonry sample; b- strengthened masonry

After completing the experimental tests values and mechanical characteristics were processed several numerical analyses were performed. FEM analyses assumptions were different depending on the composition of the samples. They were considered of distinct volumetric elements of strengthening layer, masonry, mortar or bricks. Figure 4 presents images of the models considered and their discretization.

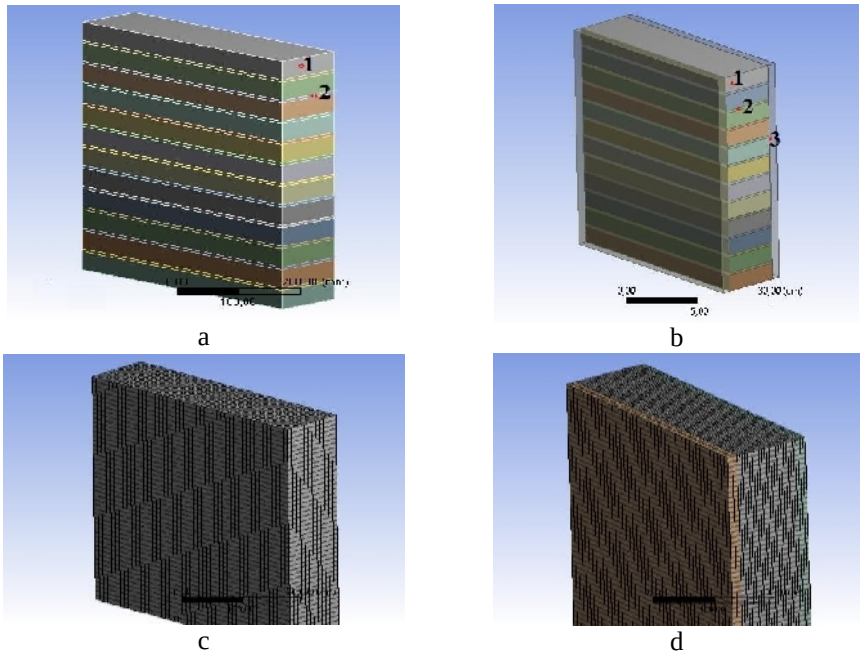

a b c d

Figure 4. Numerical models analyzed: a- un- strengthened masonry (1-brick, 2-mortar); b- strengthened masonry (1- brick, 2- mortar, 3- strengthening layer); c- homogenous simple masonry; d- strengthened masonry with 2 strengthening layers

For the numerical analyses performed on the samples the material characteristics presented in table 1 were used.

In the numerical model a horizontal load of 1000 N was applied in order to observe the distribution of the maximum and minimum principal stresses and strains. Figure 5 presents de image of map distribution of the maximum principal stresses in the case of the studied model.

Table 1.Material characteristics

Material	Tensile strength (N/mm^2)	Compressive strength (N/mm^2)	Elastic modulus in compression (N/mm^2)
Mortar	0.29	2.30	208.95
Brick	2	14.72	426.23
Masonry	0.17	8.6	322.58
Mineral composite	11.78	26.84	9007

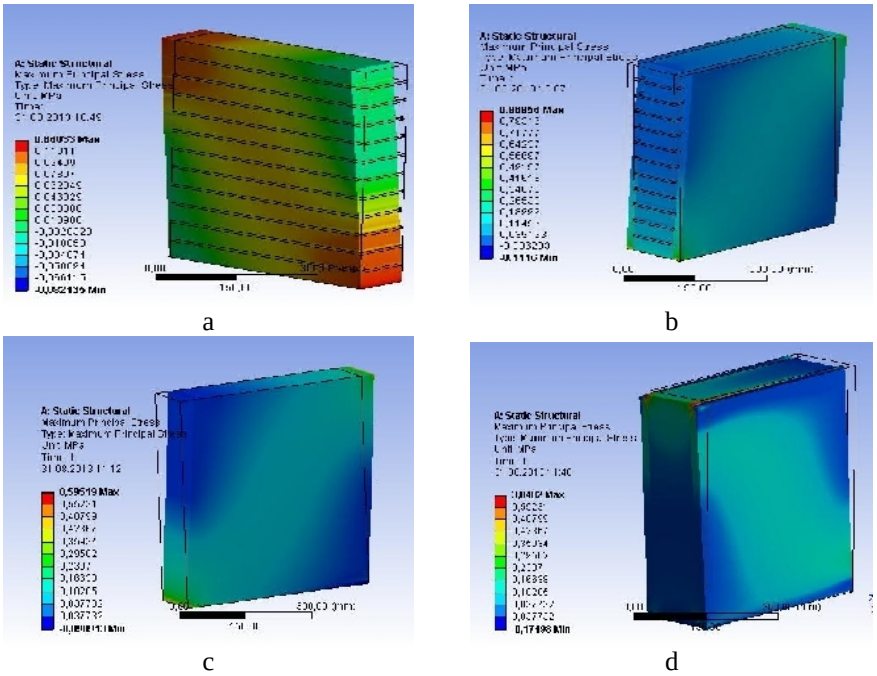

a b c d

Figure 5. Maximum principal stress: a- unstrengthened masonry composed model; b- strengthened masonry composed model; c- unstrengthened homogenous model; d- strengthened homogenous model

Comparing the results of numerical analysis and the experimental test the influence of weak mortar on masonry strength is visible. When strengthening layer is applied an increase of overall stiffness and resistance is present.

5. CONCLUSIONS

Masonry structures are numerous and spread all over the world. The use of local materials led to different behavior of these structures. Due to the age of many of these structures and damages that occurred during their existence, the study of these systems and finding suitable and compatible building solutions is required. In this paper some experimental results of uniaxial compression tests on elements of masonry with local mortar made of calcareous sand, called pufar which was used at a large scale in Iasi region were presented. In addition to verifying the material properties some strengthening solution based on glass fiber reinforcement mineral matrix composite were proposed and tested. The mineral composite consists in 50% of fine sand, 25% ordinary Portland cement and 25% of calcium sulfate in β anhydride III' form, manufactured from industrial wastes and fiberglass mesh reinforcement.

The results show a considerable improvement of the behavior of masonry by applying thin strengthening layer on both faces of masonry. The strengthening layer increases capacity and helps to redistribution of efforts in a more uniform manner across the mass of element. This solution can be applied successfully if it is possible to pour on both sides of the walls. Also it was noticed a good compatibility between materials associated (masonry and strengthening mineral composite) both experimental tests and the numerical analyses.

References

1. D.S. Robertson, (1969), *"Greek and Roman Architecture"*, 233.
2. R. Mark, P. Hutchinson, (1986) "On the Structure of the Roman Pantheon", *Art Bulletin*, 68 26.
3. Plesu, R. Taranu, R. Covatariu, D. a.o., (2012), "Strengthening and Rehabilitation Conventional Methods for Masonry Structures", *The Bulletin of the Polytechnic Institute of Jassy, Construction. Architecture Section*, Tomme: LVIII (LXII) | Fascicle: 1, pp. 113-124.
4. Taranu, G., Lungu, I., Taranu, N., (2013), "Load Carrying Elements and Structural Modular Systems Made of Synthetic Fibres Reinforced Mineral Matrix Composite", *Interdisciplinary Research in Engineering: Steps Towards Breakthrough Innovation for Sustainable Development*, volume (8-9), pp. 327-334.
5. Taranu, N., Oprisan, G., Entuc, a.o., (2012), "Composite and hybrid solutions for sustainable development in civil engineering", *Environmental Engineering and Management Journal*, 11 (4), pp. 783-793.
6. C. Baux, (2010), "Process for the industrial manufacture of compositions based on anhydrous calcium sulphate in the b-anhydrite iii' form, and corresponding compositions and binders", France Patent.
7. J.A.G. Thomas, (1972), "Fibre composites as construction materials", *Composites*, 3 2.
8. B. Aranda, O. Guillou, C. Lanos, C. Tessier, F. Le Dret, (2011), "Synthese d'un liant vert capable de concurrencer le ciment Portland", *Journée des doctorants*, Comunication orale, Université de Rennes, France.
9. Toma, I.-O., Covatariu, D., Toma, A.-M. a.o. (2013), "Strength and elastic properties of mortars with various percentages of environmentally sustainable mineral binder", *Construction and Building Materials*, pp. 348 - 361.

ISSN 2285 -2735